

**Evidence of an oceanic plateau origin and a deep,
depleted mantle source for the Iron King Volcanics,
a 1.75-Ga accreted terrane in Central Arizona**

By Bonnie A. Frey

Submitted in partial fulfillment of the requirements for
the degree of Master of Science in Geochemistry

New Mexico Institute of Mining and Technology
Socorro, New Mexico
May 2002

Department of Earth &
Environmental Science
New Mexico Tech
Socorro, NM 87801

ABSTRACT

The Iron King Volcanics in central Arizona contains lithologies (pillow basalts, hyaloclastites and hydrothermal cherts) common to the northeast-striking oceanic terranes that were accreted to the North American continent during the Paleoproterozoic. Contrary to early interpretations that these terranes are island arc sequences, the Iron King Volcanics has a basalt component that does not carry trace element signatures characteristic of island arc basalts but shows evidence for an oceanic plateau origin. As such, this component is referred to as the plume component. Evidence includes a submarine, basalt-dominated lithologic sequence with flat REE patterns and incompatible trace element patterns that do not show Ta-Nb anomalies. A comparison of incompatible element ratios (Th/Ta, La/Yb, Nb/Y, Zr/Y, Sm/Yb and Nb/Zr) in the Iron King Volcanics to volcanics from other tectonic settings supports this hypothesis. A second component of the Iron King Volcanics has lithologic and geochemical affinities to an island arc sequence, based on a volcanic sequence dominated by felsic and intermediate lithologies and the Ta-Nb depletion observed relative to other incompatible elements.

The Iron King plume volcanics contain two geochemical groups: an enriched group and a nonenriched group. These groups may have formed from different degrees of melting in different regions of the plume head. The enriched group was probably produced by small degrees of melting in a relatively cool outer section of the plume head, and the nonenriched group was produced closer to the plume's hot tail. The relationship of Nb/Y to Zr/Y in the Iron King plume-derived basalts suggests a mantle source with

mixed depleted and enriched end members. The depleted end-member was probably a deep rather than a shallow source. The mantle plume may have entrained enriched mantle material as it ascended. Like many other oceanic plateaus, the Iron King magmas developed at depths within the garnet stability field (>75 km), supported by modeling that relates $\text{CaO}/\text{Al}_2\text{O}_3$ ratios to pressure.

The plume component is interpreted to be an upper section of an oceanic plateau sliced off during obduction. Several models are suggested for the association of the plume and arc components. An acceptable model should take into consideration the absence of rock types common to deeper regions of an oceanic plateau and deformational features common to both the plume and arc components. Two models involve arc formation along the margin of an oceanic plateau: (1) The oceanic plateau collides with the continent, forcing a subduction zone to backstep to the other side of the oceanic plateau. An arc develops before more terranes collide with the outer edge of the oceanic plateau. (2) The oceanic plateau approaches a subduction zone, jams it, and forces the subduction zone to switch direction. An arc system forms on the oceanic plateau near the new subduction zone before the whole system undergoes subduction beneath and collision with a continent.

ACKNOWLEDGMENTS

This research was supported by a grant from the Research Division of New Mexico Institute of Mining and Technology to my advisor Kent Condie. I would like to thank my Kent for his advice and fine teaching and editing skills and my committee members Nelia Dunbar and Matt Heizler for their helpful suggestions. I am also grateful to Robert Kerrich for the use of the ICP-MS laboratory at the University of Saskatchewan and to Qianli Xie for overseeing the laboratory work and providing invaluable information about the laboratory process. Thanks to Amy Mathis for field assistance and Jean Wardell for her invaluable advice, support and editing skills. A special thanks goes to my husband Matt Bernhardt for his constant support and frequent understanding, especially during times of stress.

TABLE OF CONTENTS

ABSTRACT	
ACKNOWLEDGMENTS	ii
TABLE OF CONTENTS	iii
LIST OF FIGURES	v
LIST OF TABLES	vii
INTRODUCTION	1
GEOLOGICAL SETTING	5
Transcontinental Proterozoic Provinces	5
Arizona's Transition Zone	5
Yavapai Supergroup.....	8
Big Bug block	9
Metamorphism	13
Geologic history.....	14
Iron King Volcanics	17
Introduction.....	17
Basalts	18
Felsic/intermediate volcanics.....	21
Chert.....	21
Volcaniclastic rocks	24
Primary textures	27
Area ore deposits.....	28
TECTONIC SETTINGS	31
Lithologic evidence.....	33
Geochemical evidence	37
RESULTS	43
Classification.....	48
Major elements.....	51
Trace elements	57
Plume versus arc components.....	57
Arc volcanics	57
Plume-derived basalts	63
DISCUSSION	66
Introduction.....	66
Effects of alteration.....	66
Tectonic discrimination	71
Lithologic association	74
Geochemical evidence	77
Magma models.....	83

Introduction.....	83
Continental contamination.....	83
Fractional crystallization.....	84
Partial melting.....	89
Difference between enriched and nonenriched plume components	101
Models for the association of Iron King plume volcanics with arc volcanics	104
CONCLUSIONS	108
APPENDIX A : Petrographic report of the Iron King Volcanics	111
APPENDIX B : Analytical methods.....	114
APPENDIX C: Loss on ignition diagrams.....	123
REFERENCES.....	134

LIST OF FIGURES

Figure		Page
1	Map of orogenic belts and age provinces in North America	6
2	Map showing the locations of the Colorado Plateau, Basin and Range Province, and the transition zone in Arizona	7
3	Geologic map of Iron King Volcanics and the surrounding units	10
4	Pillow basalts of the Iron King Volcanics	19
5	Chert in the Iron King Volcanics	22
6	Volcanic breccia in the Iron King Volcanics	25
7	Origin of oceanic plateaus and ocean islands	32
8	Idealized lithologic sequence for sections of the Caribbean Plateau in Columbia and Ecuador.....	35
9	Incompatible element distributions in normal mid-ocean ridge basalts, arc basalts, ocean-island basalts, and Ontong-Java	40
10	Enlargements of the northern and southern sections of Iron King Volcanics and the surrounding units.....	44
11	Pie charts showing the distributions of eruption types characteristic of the northern and southern sections of the Iron King Volcanics	47
12	Zr/TiO ₂ -Nb/Y rock classification diagram	52
13	Volcanic series on an Y-Zr diagram showing the distribution of the Iron King Volcanics.....	53
14	Major element variation diagrams for the Iron King Volcanics	54
15	Phosphorus and titanium oxide variation diagrams.....	56
16	Primitive-mantle normalized graphs of the Iron King Volcanics.....	58
17	REE graphs of the Iron King Volcanics	60

18	Graph of loss on ignition (LOI) vs. MgO for the Iron King Volcanics.....	69
19	Iron King Volcanics plotted on graph of LOI against SiO ₂	70
20	LOI versus CaO/Al ₂ O ₃ plot for the Iron King Volcanics and separate graphs of LOI versus CaO and Al ₂ O ₃	72
21	LOI vs. Th/Ta for the Iron King Volcanics	73
22	Interpretive map of the distribution of arc and oceanic plateau assemblages within the Iron King Volcanics.....	76
23	Th/Ta vs. La/Yb graph showing fields for N-MORB, oceanic plateau basalts, oceanic island basalts, and island arc basalts.....	78
24	Nb/Y vs. Zr/Y graph of Iron King basalts	80
25	Iron King Volcanics plotted on Sm/Yb vs. Nb/Zr graph.....	82
26	Th vs. Ta graph of Iron King Volcanics	85
27	Graph of Ni vs. Mg# for the plume-related members of the Iron King Volcanics.....	86
28	Calculated results for fractional crystallization model for the Iron King Volcanics.....	90
29	Calculated melt compositions of a batch melting model.....	92
30	La/Sm and Sm/Yb diagram of Iron King Volcanics.....	94
31	CaO/Al ₂ O ₃ vs. Al ₂ O ₃ graphs for Iron King Volcanics and other oceanic plateaus. Fields and numbers represent the pressures in GPa	96
32	Trace element diagrams that demonstrate the effect of small to large degrees of melting on trace element ratios	98
33	Zr/Hf vs. Zr, Sc and Ni for the Iron King Volcanics	100
34	Diagram demonstrating a possible model for the accretion of the Iron King Volcanics.....	106
	Appendix C: Loss on ignition diagrams for incompatible elements and element ratios	124

LIST OF TABLES

1	Zircon ages pertinent to events that affected the Big Bug block.....	15
2	Major and trace element results for the Iron King Volcanics.....	49
3	CIPW weighted norms for Iron King Volcanics.....	67
4	Bulk distribution coefficients for fractional crystallization and batch melting	88
5	Mafic partition coefficients (K)	88
6	Detection limits of major and trace element analyses	115
7	Element concentrations in the calibration standards and spike solution.....	118
8	Experimental and accepted values of standard MRG-1 and standard deviation for the Iron King Volcanics analysis	119
9	Comparison of two different runs on the ICP-MS for nine Iron King Volcanics samples.....	121

INTRODUCTION

Since the recognition of plate tectonics in the 1960s, several methods of continental growth have been proposed. Two well-accepted modes of continental growth are the addition of magma to the crust by under- and overplating and the addition of oceanic terranes to the continental margins by the collision and accretion (Condie, 2001). One interpretation of the terrane accretionary model was based on the belief that greenstone belts consisted of material from single tectonic settings such as island arcs, back arc basins and continental rifts, rather than normal ocean floor material (Thurston, 1994). The southwestern United States is one region where this type of continental growth is considered by many geoscientists to have been the prevalent mode of growth.

However, debate about the details of continental growth continues. Since the discovery of oceanic plateaus in the mid-1970s, geoscientists have realized that these anomalously thick sections of ocean floor may also play a significant role in continental growth. As the technology used to study the ocean floors improved, more and more modern-day oceanic plateaus were discovered, and it was recognized that they could provide a significant volume if they were accreted to the continents. For example, Schubert and Sandwell (1989) reported that the total anomalous crustal volume of modern oceanic plateaus was 4.9% of the total volume of the continental crust. They determined that if this material was accreted over a period of 100 My, it would add 3.7 km³/yr to the continents, compared to 1.1 km³/yr added by ocean island arcs. In addition, researchers began to find within-plate oceanic sequences in Archean and Proterozoic greenstones (Thurston, 1994). Evidence for a "continental-growth-by-accretion-of-

mantle-plume-material” theory was promising. However, supporters were faced with the problem of ocean floor buoyancy. As the plates move, much of the ocean floor, with an average thickness of about 5-7 km (Condie, 1997b), is simply subducted, leaving little evidence on the continents of its former existence. Researchers were faced with proving that the same fate did not happen to oceanic plateaus. Several studies, including one by Cloos (1993), have successfully shown that plateaus can undergo obduction if they reach a minimum thickness of 30 km. The challenge appears to have changed from “Do oceanic plateaus contribute to continental growth?” to “If they contribute to continental growth, why can’t we recognize a significant number of them in the rock record?” Kerr et al. (2000) recently suggested that oceanic plateaus are available in the crustal record. They proposed that the real challenge is finding them and publishing the evidence.

One obstacle to recognizing the tectonic source of greenstones is developing the tools to do so. Tools to identify oceanic plateaus in the rock record were developed in large part by studies of modern oceanic plateaus, including the largest ones, Ontong Java and Caribbean plateaus. Isotope and trace element studies have helped geoscientists recognize the unique geochemical signature of oceanic plateau basalts. In addition, the discovery of accreted pieces of the Caribbean plateau in South and Central America have provided lithologic and stratigraphic sections of oceanic plateaus (Kerr et al., 1998). These new tools have been tested and proved with the discovery of other oceanic plateau terranes on the continents. Examples include several young greenstones such as Wrangellia Terrane in British Columbia, Angayucham Terrane in northwestern Alaska, and several accreted terranes in Japan (Condie, 2001).

These discoveries provide incentive to reexamine greenstones in areas such as the southwestern United States where the large volumes of juvenile crust are interpreted to be arc volcanics (e.g. Anderson and Silver, 1976; Smith, 1992; Condie, 1986). More recent studies in Colorado, New Mexico and Arizona have uncovered geochemical signatures similar to modern-day oceanic plateau basalts (Knoper and Condie, 1988; Vance, 1989). This investigation focuses on a large Proterozoic greenstone in central Arizona that not only contains metabasalts with arc geochemical signatures, but also contains metabasalts with oceanic plateau signatures (Vance, 1989). The Iron King Volcanics is a 1.75 Ga succession southeast of Prescott, Arizona, that contains abundant pillow basalts and volcanoclastic rocks (Anderson, 1972; Anderson and Blacet, 1972a). These rocks provide evidence of a submarine origin, similar to some island arcs. Unlike island arc basalts, however, many mafic units in the Iron King Volcanics show no depletion in the elements Nb and Ta, a characteristic feature of modern and ancient island arcs (Vance, 1989).

The geochemical signatures used to identify the tectonic source of basalts are not given by major elements or large ion lithophile elements, which are susceptible to hydrothermal alteration and metamorphism, but by high field strength elements (HFSE), which are considered immobile in aqueous environments and during alteration processes (Winchester and Floyd, 1977; Condie, 1994). HFSE, elements that have a high valence-charge to ionic-radius ratio, include the rare earth elements (REE) and Sc, Y, Th, Zr, Hf, Ti, Nb, Ta and P (Rollinson, 1993). The immobility of these elements allows geoscientists to look beyond surficial processes that can change the distribution of mobile elements, and instead focus on the composition of mantle sources of magmas and magmatic processes, such as fractional crystallization and partial melting.

The purpose of this study is three-fold: (1) to show that the Iron King Volcanics originated as an oceanic plateau; (2) to characterize the mantle source and mantle processes that produced geochemical signatures in the Iron King Volcanics; and (3) to provide a model of the tectonic history of these volcanics.

GEOLOGICAL SETTING

Transcontinental Proterozoic Provinces

The Iron King Volcanics is one of many terranes in the Transcontinental Proterozoic provinces that make up a 1200- to 1300-km wide swath of North America (Fig. 1) named by Van Schmus and Bickford (1993). A province is a large tract of an orogen that was assembled during one major pulse of convergent tectonism (Karlstrom and Bowring, 1988). These provinces are a collection of mainly juvenile Proterozoic terranes that were accreted to the North American Archean craton (Van Schmus and Bickford, 1993) between 1.8 to 1.65 Ga, providing a significant addition to the supercontinent Laurentia (Hoffman, 1988, 1989). Trending northeast to east-northeast, the provinces are defined by regional lithology and structure, U-Pb zircon dating, Sr-Nd-Pb isotopic signatures, and regional geophysical anomalies (Van Schmus and Bickford, 1993). The main exposures of this Proterozoic crust occur in the southwestern United States in the Cordillera extending from southern Wyoming to northern New Mexico, in the mountains of New Mexico that border the Rio Grande rift, along the San Andreas fault system of southern California, and in the Arizona transition zone between the Basin and Range Province and the Colorado Plateau (Condie, 1981; P.F. Hoffman, 1988).

Arizona's Transition Zone

The Arizona sections of the Basin and Range Province, the Colorado Plateau, and the 500-km long transition zone between them are shown on Figure 2. The transition zone trends northwest, perpendicular to the strike of the Proterozoic terranes within it.

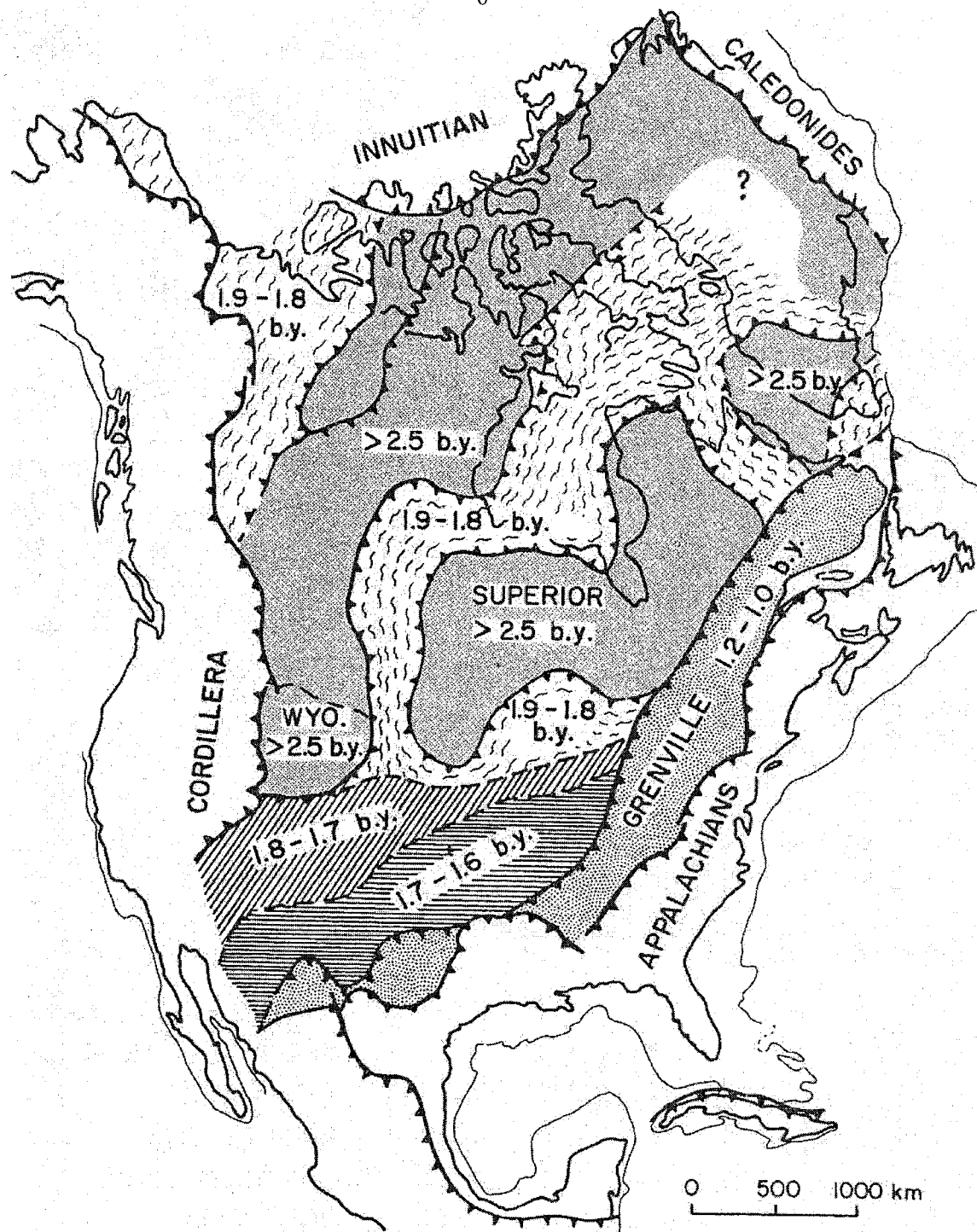


Fig. 1 Map from Karlstrom et al. (1987) of orogenic belts and age provinces in North America. The Transcontinental Proterozoic provinces described by Van Schmus and Bickford (1993) include the age provinces marked in horizontal and diagonal stripes (1.6-1.8 Ga). The Hudsonian Craton described by Van Schmus and Bickford (1993) includes the provinces with ages >1.8 Ga.

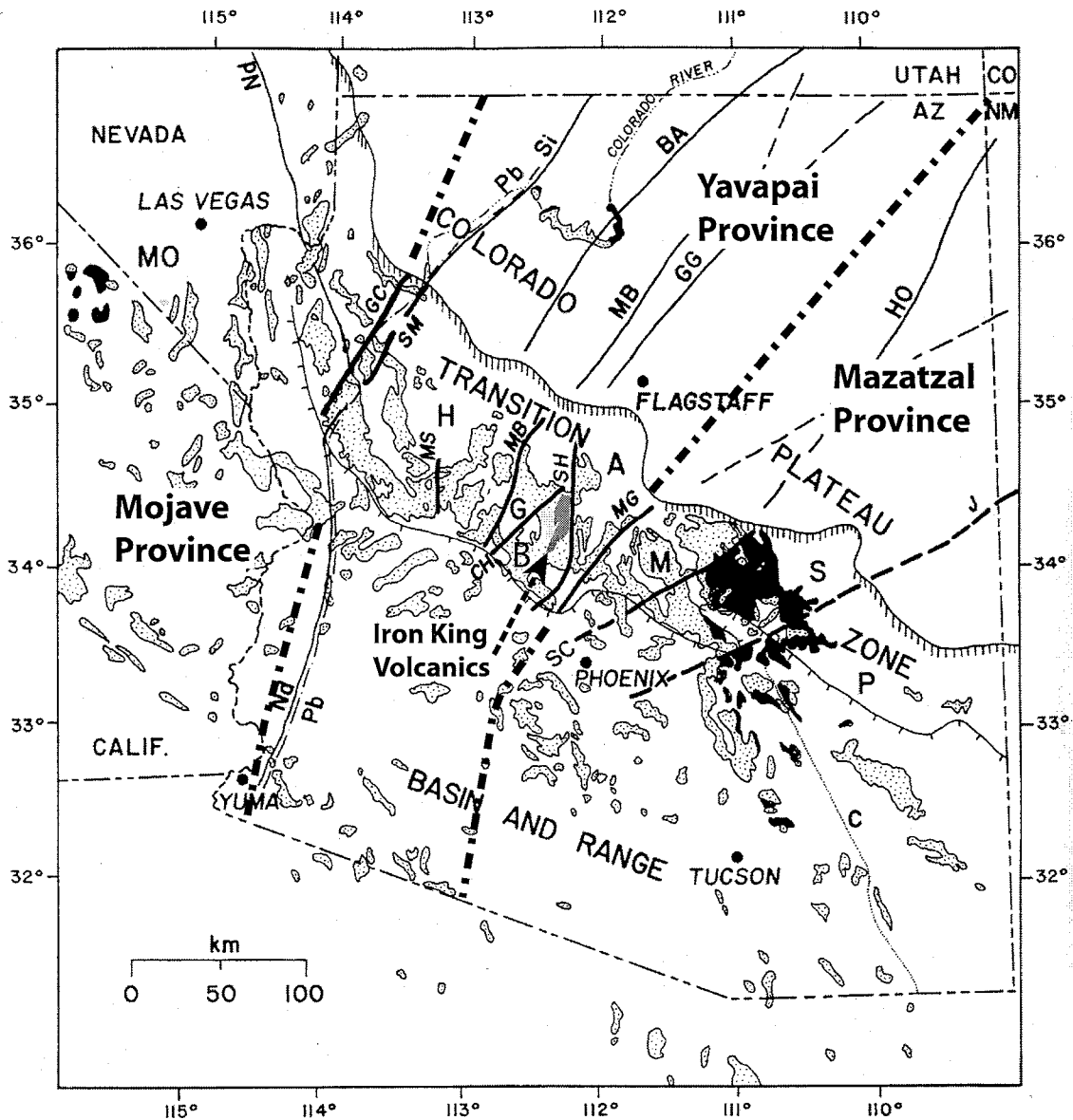


Fig. 2 Map after Karlstrom and Bowring (1993) showing the locations of the Colorado Plateau, Basin and Range Province, and the transition zone in Arizona. Stippled areas show Paleoproterozoic rocks, and black areas show Mesoproterozoic rocks. The centrally located Iron King Volcanics is shown in gray within the Big Bug block (B) of the transition zone. Other blocks include the Mojave (M), Hualapai (H), Green Gulch (G), Ash Creek (A), Mazatzal (M), Sunflower (S), and Pinal (P). Other features pertinent to this study include two faults, the Chaparral (CH) and the Shylock (SH). Heavy dotted and dashed lines show the outline of the Yavapai Province.

Because of their juxtaposition between the Basin and Range Province and the Colorado Plateau, rocks in the transition zone have undergone Laramide compressional faulting and later extensional faulting, which have contributed to the exposure of older rocks such as Proterozoic volcanics and intrusives (Vance, 1989). Although the whole region has undergone such late-stage deformation, the structure within the transition zone was only slightly affected by deformation and considerable information about Proterozoic events is still available (Darrach et al., 1991). By dating igneous rocks in the transition zone, researchers have recognized three tectonic provinces in Arizona's transition zone: the Mojave, Yavapai and Mazatzal provinces, listed here in order from oldest to youngest and from west to east (Fig. 2).

Yavapai Supergroup

The Iron King Volcanics is located in the Yavapai Province (Fig. 2), a greenstone belt ranging in age from 1.76 to 1.70 Ga that was added to the continent during the 1.70-Ga Yavapai orogeny (Karlstrom and Bowring, 1988; Karlstrom, 1991). The province is made up of four blocks: the Ash Creek, Big Bug, Green Gulch, and Hualapai blocks (Karlstrom and Bowring, 1993). This report follows Karlstrom and Bowring's (1988) definition of "block": "an area of Proterozoic basement bounded by major Proterozoic faults and shear zones." The shear zones that form the boundaries of these blocks have a predominantly northeast trend that continues into the Colorado Plateau (Fig. 2).

The Paleoproterozoic rocks in this region were given the chronostratigraphic name, Yavapai Series, by Anderson et al. (1971), but will be referred to by the lithostratigraphic name, the Yavapai Supergroup (Henderson et al., 1980), throughout

this report. The supergroup contains metamorphosed basaltic to rhyolitic volcanics, ash-flow tuffs, and volcanogenic sedimentary rocks intruded by granodioritic batholiths (Anderson and Silver, 1976; Karlstrom et al., 1987). The metamorphic grade of these rocks is primarily greenschist to amphibolite facies (Karlstrom et al., 1987). Several authors suggest the volcanic rocks in the series originated in an island-arc setting (Anderson and Silver, 1976, 1978; Condie, 1984; Karlstrom et al., 1987).

Big Bug block

The Big Bug block, named for exposures along the Big Bug Creek (Anderson et al., 1971), contains two Precambrian formations: the Iron King Volcanics and the older Spud Mountain Volcanics (Fig. 3a-b). The Big Bug Group also includes the Green Gulch Volcanics, but since they fall outside the block (northwest of the Chaparral shear zone) they are not considered in this report. As indicated by the formation names, the Big Bug block is made up of mostly volcanic and volcanoclastic rocks (Anderson and Blacet, 1972a). These volcanic rocks include pillow basalts, rhyolite, chemical sediments and exhalative deposits. The volcanic rocks are separated from Precambrian volcanogenic sedimentary rocks, including the 1.72 Ga Texas Gulch Formation, by a regional unconformity (Karlstrom and Bowring, 1993). The Texas Gulch Formation consists of metasedimentary rocks of quartz wacke, pelitic schist and slate (Karlstrom and Bowring, 1993). Gabbroic sills and granitic plutons are found throughout the block. Anderson and Blacet (1972) proposed, based on the similarity of mineralogy and chemical composition, that the gabbroic sills were injected into the thick sequences of basaltic pillows as they were accumulating. Notable plutons near the Iron King

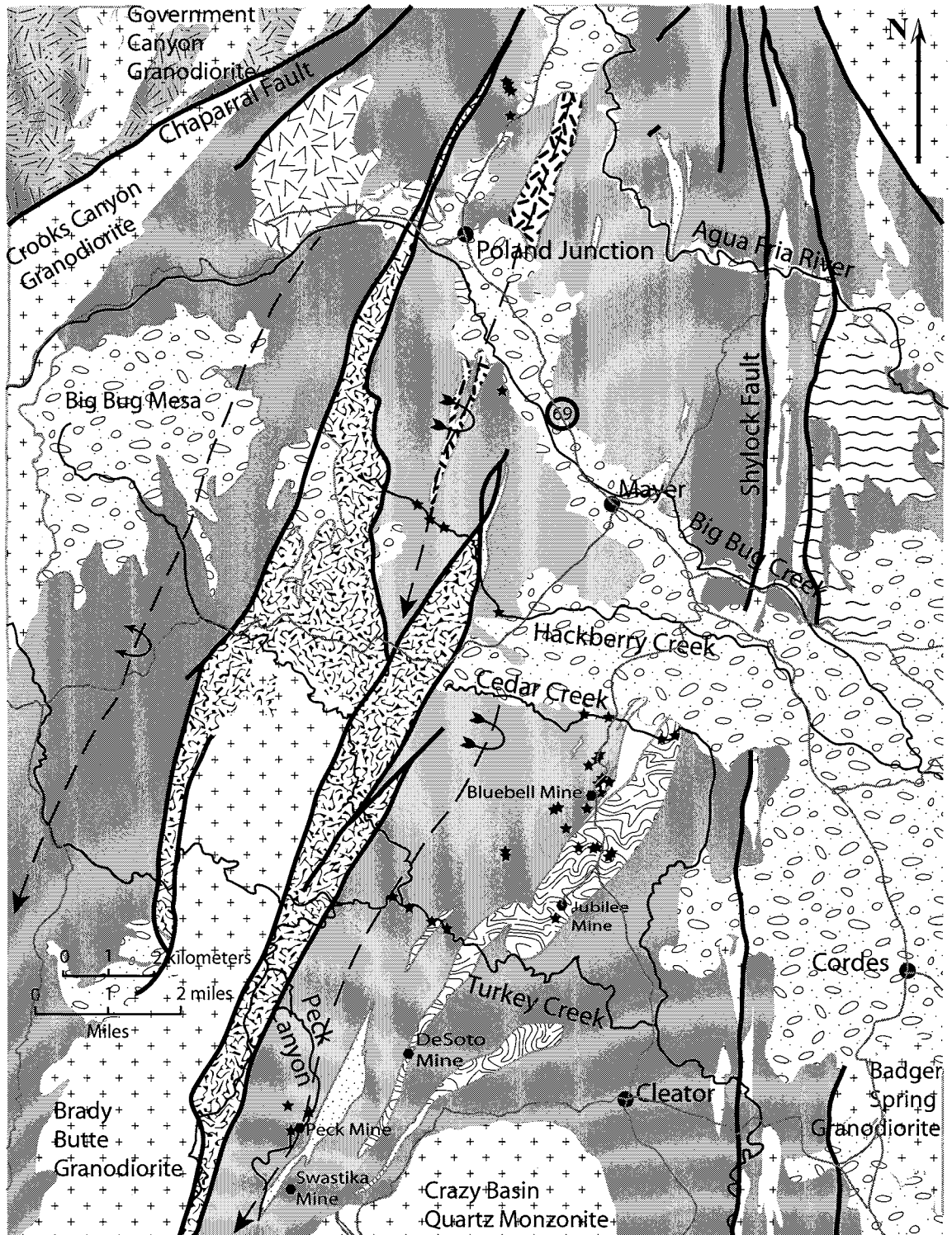



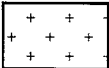
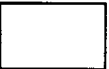

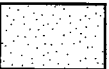

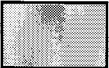
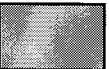






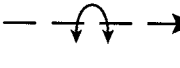






Fig. 3a Geologic map of Iron King Volcanics and the surrounding units. After Anderson and Blacet (1972b and c). Key listed on Fig. 3b.

Fig. 3b Key to geological map of Iron King Volcanics and surrounding formations

-  Tertiary and Quaternary sediments
-  Texas Gulch formation -- sandstone, tuff, slate, limestone and conglomerate
-  Tertiary granodiorite
-  Precambrian intrusives -- includes granites, granodiorite, Alaskite, quartz monzonite, gabbro and quartz porphyry
-  IKC -- ferruginous chert beds
-  IKAB -- mafic flows at base of Iron King Volcanics interbedded with chert, carbonate and breccia
-  IKR -- bedded tuffs with sericitic base
-  IKAT -- andesitic-rhyolitic tuffaceous rocks
-  IKA -- andesitic and basaltic amygdaloidal and pillow flows
-  Spud Mountain Volcanics
-  Green Gulch Volcanics
-  Silicified and sericitized rocks

-  Fault line
-  Rivers
-  Roads
-  Plunging syncline
-  Plunging anticline
-  Town
-  Mine
-  Sample location
-  Highway

Volcanics include the Crooks Canyon Granodiorite, the Brady Butte Granodiorite and the Crazy Basin Quartz Monzonite (Fig. 3a). The Big Bug block is capped in some locations by Tertiary and Quaternary sedimentary rocks, as well as minor Tertiary volcanics.

Paleoproterozoic rocks of the Big Bug block are isoclinally folded and dip steeply (Anderson and Creasey, 1958). Major structures are an overturned plunging anticline on the west and an associated plunging syncline to the east, both trending northeast (Anderson, 1972). Anderson and Creasey (1958) estimated that the syncline plunges about 7° to the south. Multiple small folds along the edges of the major folds and thinning and thickening of units caused by deformation prevent an accurate measurement of the Big Bug block's width, according to Anderson and Blacet (1972a), but Anderson and Creasey (1958) estimated that the block is about 6-km thick.

Proterozoic shear zones, each 2-km thick, bound the block on two sides: the Chaparral shear zone on the northwest side of the block and the Shylock shear zone on the east (Fig. 3a). The northeast-trending Chaparral shear zone is in contact with the Crooks Canyon Granodiorite for most of the fault's length. It has a subvertical, northeast-striking foliation and a shallowly plunging northeastern lineation (Karlstrom and Bowring, 1993). The Shylock shear zone extends 60 km from north to south and is in contact with the Spud Mountain Volcanics.

Several characteristics are the same for both shear zones. Both have right-lateral strike-slip movement, with about an 8-km slip evident on the Shylock shear zone (Anderson and Blacet, 1972a), and both underwent ductile deformation as indicated by mylonization (Darrach et al., 1991; Karlstrom and Bowring, 1993). They are considered

zones of high shortening that were progressively overprinted by strike-slip movement (Karlstrom, 1991). Karlstrom and Bowring (1993) proposed that similar fabrics in the Chaparral shear zone and in a section of the Shylock shear zone (Cleator shear zone, Darrach et al. [1991]), indicate that movement along the shear zones occurred at the same time (1.7 Ga). These fabrics are also mimicked within the Big Bug block between the shear zones. According to Karlstrom and Bowring (1993), this is an indication that movement along the shear zones resulted in contemporaneous migration of the Big Bug block to the south.

Metamorphism

The metamorphic grade of the Big Bug block, including the Iron King Volcanics, ranges from lower greenschist to middle amphibolite facies (Vance, 1989). Vance (1989) states that most of the Iron King Volcanics represents greenschist facies as shown by such minerals as albite, actinolite, quartz, calcite and biotite, chlorite and epidote. Petrographic studies in this investigation and in Vance's investigation show actinolite and epidote in rocks from Mayer north to the Iron King Mine.

Metamorphic grade increases toward the younger plutonic rocks such as the Crazy Basin Quartz Monzonite and the Brady Butte Granodiorite (Anderson, 1972). Vance (1989) states that local chemical gradients also result in amphibolite grade metamorphism, such as mafic rocks near Bluebell Mine where hornblende, oligoclase and andesine are found. Petrographic investigations in this study confirm that the mafic rocks south and southwest of Bluebell Mine underwent amphibolite grade metamorphism.

Williams (1991) reported that metamorphic temperatures of the Big Bug block amphibolites range from 400°C away from the Crazy Basin Quartz Monzonite to as high as 600°C near the pluton. Metamorphic pressures in the block were about 3 kbars.

Geologic history

The Precambrian history of the Big Bug block and its relationship to the Yavapai and surrounding provinces has been compiled from several investigations (e.g. Anderson and Creasey, 1958; Vance, 1989; Karlstrom and Bowring, 1988; Karlstrom and Bowring, 1993) and is summarized below. A list of U-Pb zircon ages that helped constrain the timing of events is given in Table 1.

- (1) The Spud Mountain and Iron King Volcanics were erupted between 1.755 and 1.740 Ga. This date is based on the age of a rhyolitic flow in the Spud Mountain Volcanics.
- (2) The Brady Butte Granodiorite crosscuts both of these volcanic formations, indicating that the two volcanic sequences were in tectonic contact by the time of the intrusion at 1.75 Ga.
- (3) An unconformity developed as the volcanics and intrusions were eroded and the Texas Gulch Formation was deposited on top of them. The tuffaceous felsic clasts and purple to gray shale that make up the Texas Gulch Formation contain clasts from the Alder Group in the Mazatzal province and the Big Bug Group in the Yavapai province. The maximum age obtained from zircons found in the Texas Gulch tuffs is 1.71-1.72 Ga (Conway and Silver, 1989).

Table 1 Zircon ages pertinent to events that affected the Big Bug block.

Zircon source	Geographical location of source	Block where located	Age	References
Rhyolitic flow, Spud Mountain Volcanics	West of Iron King Volcanics, Central Bradshaw Mountains	Big Bug	1.755 +/- 10 Ga*	1, 2
Brady Butte Granodiorite	West of southern Iron King Volcanics	Big Bug	1.750 +/- 10 Ga*	1, 2
Government Canyon Granodiorite	NW of Iron King Volcanics, across Chaparral Fault	Green Gulch	1.750 +/- 15 Ga*	1, 2
Badger Spring Granodiorite	Southeast of Iron King Volcanics	Ash Creek	1.740 +/- 10 Ga	3
Crazy Basin Quartz Monzonite	South of Iron King Volcanics, Central Bradshaw Mountains	Big Bug	1.699 +/- 5 Ga	3
Crooks Canyon Granodiorite	West of northern Iron King Volcanics	Big Bug	1.735 Ga, no error provided	4

1. Anderson et al. (1971)
2. Anderson and Silver (1976)
3. Karlstrom et al. (1987)
4. Karlstrom and Bowring (1993)

* Values reported before 1977 have been reduced by 20 Ma to correct to more recent recommended decay constants (Steiger and Jaeger, 1977).
References listed here do not indicate sigma values of the error.

- (4) An F1 deformational event between 1.750 and 1.700 Ga caused recumbent and some upright folding in the Texas Gulch sediments and everything older, including the Iron King Volcanics. Karlstrom and Bowring (1993) associate this deformation with northwest directed thrusting.
- (5) F1 folds were overprinted by tight, isoclinal, upright folds during an F2 event of intense shortening around 1.70 Ga. This period of deformation is referred to as the Yavapai orogeny by several authors. Williams (1991) states that peak metamorphism in the Yavapai Province occurred during this period. The shortening is considered to be synchronous with the emplacement of the Crazy Basin Quartz Monzonite, supported by the tendency of temperatures to increase toward the pluton in all directions (Williams, 1991). Karlstrom and Bowring (1993) suggest that some shortening also predated the intrusion. The dominant northeast-trending, vertical fabric is a result of the F2 event (Karlstrom and Bowring, 1993). This event also coincides with movement along the Chaparral and Shylock shear zones, which is suggested by the mylonization that developed along the 1.735-Ga Crooks Canyon Granodiorite as the adjoining Chaparral shear zone cut across it. Furthermore, fabrics similar to the shear zone fabrics developed across the Big Bug block (Karlstrom and Bowring, 1993).

Karlstrom and Bowring (1988) suggest that the Yavapai province was assembled in two sections. The Hualapai and Big Bug blocks were assembled during the same 1.70-Ga tectonic event. Although they have distinct pre-1.7 Ga tectonic histories, they collided at about 1.7 Ga (Karlstrom and Bowring, 1988). The Ash Creek and Green

Gulch blocks, on the other hand, were part of a separate terrane that was thrust across and folded around the Big Bug block into an antiform (Karlstrom and Bowring, 1988). Bowring et al. (1991) have recently dated Ash Creek Group rhyolites in the Jerome area at 1.74 Ga.

Iron King Volcanics

Introduction

The Iron King Volcanics is named after Iron King Gulch where the formation is exposed (Vance, 1989). The stratigraphic sequence contains a lower unit of pillow basalts and andesitic and basaltic flows in the southwest and an upper unit of mafic and felsic tuffaceous rock in the northeast (Vance, 1989). Several studies have shown that all units have undergone greenschist to amphibolite-facies metamorphism. All units have also undergone considerable deformation during which localized zones of shearing formed, particularly within ash and tuff units. The relationship of the Iron King Volcanics to surrounding units is evident on Anderson and Blacet's (1972b, 1972c) maps, which have been reproduced on Figure 3a-b. The Iron King Volcanics is bounded on the west by a fault, which separates the unit from the sedimentary Texas Gulch Formation (Fig. 3a). On its eastern side, the Iron King Volcanics is in direct contact with the Spud Mountain Volcanics. In the northeast, small folds have caused interfingering between the two formations. The Spud Mountain Volcanics also outcrops west of the Texas Gulch Formation, lending evidence for a syncline that encloses the Iron King Volcanics along its central axis. Anderson and Blacet (1972a) estimate that the Iron King Volcanics is about 3000 m thick.

As shown in earlier studies and confirmed by this study, the Iron King Volcanics contains five main rock types: basalt flows, rhyolite, hydrothermal deposits (mostly chert), volcanic breccia, and rhyolitic to mafic ash flow deposits. Mafic flows, the dominant rock source, are capped by pillow basalts and rhyolites and are interbedded with the chert, breccia and ash flow deposits. The rock types will be referred to by the names of their protoliths throughout this study.

Basalts

Basalt makes up nearly 50 percent of the Iron King Volcanics and is present as pillow basalts or massive basalts that represent interior lava flows or intrusives such as sills or dikes. The basalts have been metamorphosed to amphibolites with grain sizes varying from fine to medium. Rock color ranges from grayish green to greenish black depending on the amount of chlorite present. The darker amphibolites owe their dark color to actinolite amphibole (Anderson and Blacet, 1972a).

Pillow basalts, which indicate fast cooling rates and slow flow rates (Fink and Griffiths, 1992), are common in the Iron King Volcanics. The pillows range in size from less than a centimeter to half a meter in length. Chilled margins occur in nearly all pillow basalts (Fig. 4a-d). In many cases, quartz veins have formed around the outer perimeter of the pillows. The pillows are generally flattened and deformed, masking the stratigraphic top of the flow. Individual flows range from about a meter to tens of meters (Anderson and Blacet, 1972a).



Fig. 4a Flattened pillow basalts displaying chilled margins. Location is within Cedar Creek 100 m west of Forest Route 93.

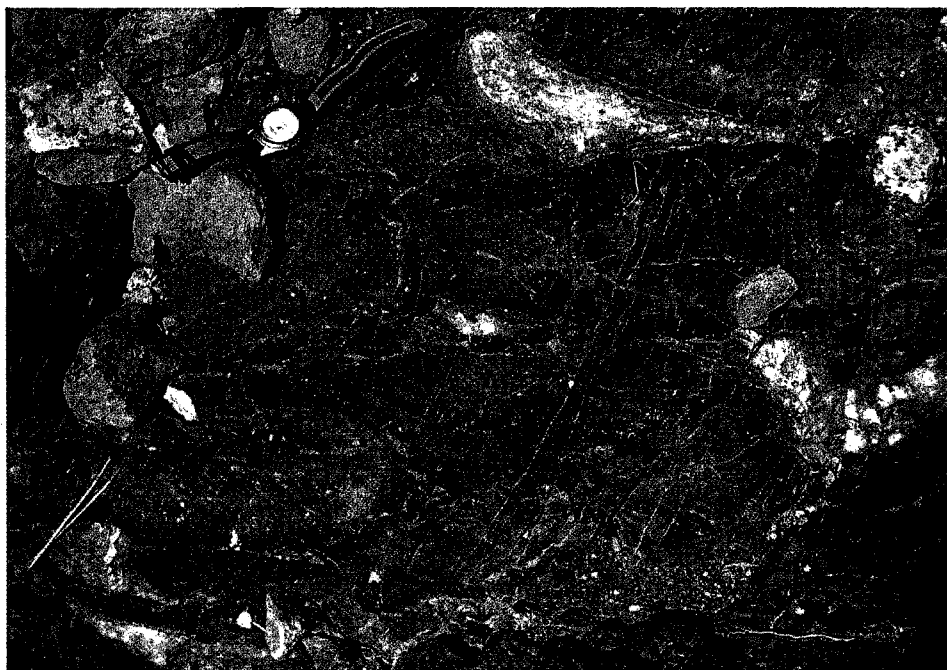


Fig. 4b Pillow basalts showing chilled margins within Black Rock Canyon, south of Jubilee Mine.



Fig. 4c (top)
Pillow basalts in Cedar Creek within 500 m of Forest Route 93. Quartz fills in gaps between the pillows. Chilled margins are no longer dark rims, but are lighter and show separation from the pillows because of weathering.

Fig. 4d (bottom)
Nearby pillow basalts that have undergone silica replacement.

Felsic/intermediate volcanics

Felsic and intermediate rocks comprise about 20% of the Iron King Volcanics. The felsic volcanics were metamorphosed to quartz sericite schists, and deformation has left little evidence of relict textures (Vance, 1989). The felsic protoliths were rhyolitic flows and tuff (Anderson, 1972). The intermediate rocks, which have been metamorphosed from andesitic flows and tuffs to amphibolite (Anderson, 1972), are difficult to distinguish from the mafic amphibolite. These rock types are most concentrated in the eastern and northern sections of the Iron King. Most of the formation's ore deposits are associated with felsic deposits.

Chert

Chert, which comprises only about 1% of the Iron King Volcanics, has three occurrences: black chert high in magnetite, layers of ferruginous chert interbedded with silicified ash, and silicified pillows and ash (Fig. 5a-c). Although chert is found throughout the Iron King Volcanics, it is most concentrated in outcrops along Cedar Creek, where it not only appears in the most continuous outcrops but also is strongly folded on a scale of centimeters to meters (Fig. 5a). Anderson (1972) measured a width of at least 600 m for chert outcrops within a one-kilometer section of Cedar Creek east of Forest Route 93, but no estimate was made as to how much the folding adds to the width. The unit thins to the southwest and has a width of only about 120 m just east of the Blue Bell mine (Anderson, 1972). An analysis of the chert beds southeast of Blue Bell mine yielded SiO₂, 52.4%; Fe, 29.0%; Mn, 0.9%; TiO₂, 0.6%; and S, 0.11% (Anderson, 1972).

The ferruginous chert in the Iron King Volcanics is similar to Algoma-type iron-



Fig. 5a Folded chert and ash beds within Cedar Creek, about 850 m east of Forest Route 93.



Fig. 5b Chert boudins within a highly sheared zone of ash and chert beds. Location is in Cedar Creek, about 650 m east of Forest Route 93.



Fig. 5c Boudin of slightly deformed ferruginous chert in a mass of highly deformed basalt and minor amounts of yellowish-orange carbonate. Located in Cedar Creek, about 1000 m east of Forest Route 93.

formation. Algoma-type iron formation develops within marine volcanic settings, unlike Lake Superior-type iron-formation, which forms in shelf and platform basins, and Rapitan-type iron-formation, which forms in association with glacial deposits (Gross, 1996a). Algoma-type deposits develop when particles of silica and iron are added to the water column by hydrothermal venting and then are precipitated by adsorption on amorphous iron and manganese oxides and smectite clays in surrounding sediments, either in anoxic or oxidizing environments (Gross, 1996b). Ferruginous chert consists of alternating layers of chert and iron-rich oxides, silicates, carbonates, and sulfides, and it is interbedded with clastic and pelagic sediments, tuff, and volcanic rocks (Gross, 1996b).

Within the Iron King Volcanics, iron formation is frequently found interbedded with tuff, carbonates and basalt. Chert ribs are invariably the predominant rock in boudins in zones of heavy shearing. Basalt also forms boudins in the sheared zones but it is usually highly deformed.

Volcaniclastic rocks

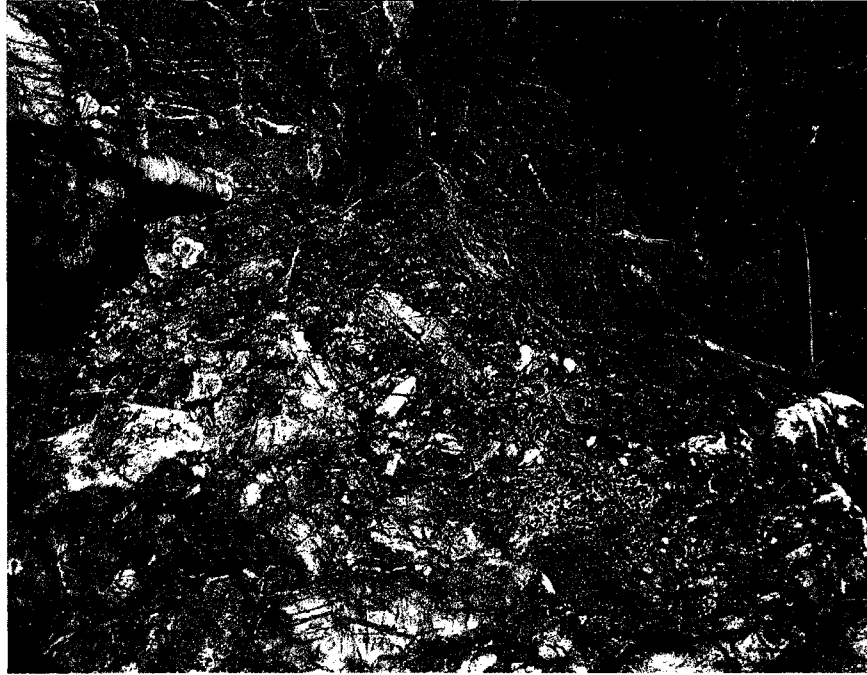
About 18% of the Iron King Volcanics consists of breccia and 4% includes tuffaceous volcanic sediment. Volcaniclasts within the breccia include carbonate, chert, coarse- to fine-grained amphibolite, felsic to intermediate volcanic rocks, and volcanic glass-fragments (now recrystallized). Breccias in the Iron King Volcanics are most commonly heterolithologic breccias (Fig. 6a, c and d), those described by Fisher and Schmincke (1984) as containing clasts of more than one rock type and displaying varying degrees of rounding as a result of extrusion or transportation. Many of the clasts



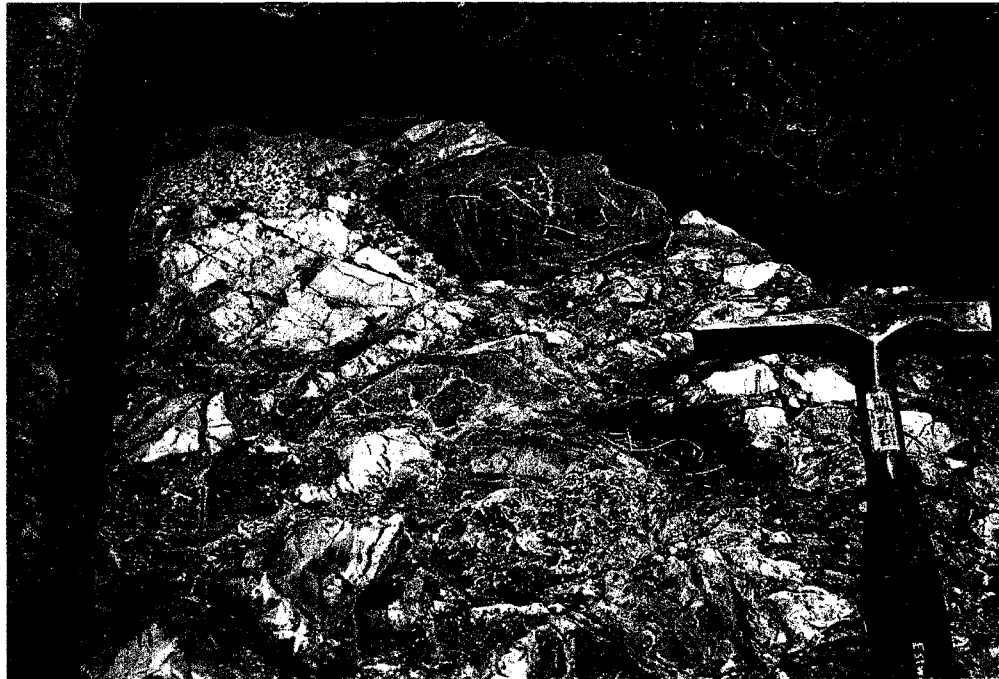
Fig. 6a Heterolithic breccia in Black Rock Canyon within 400 m of primitive road that forks off of Forest Road 93 about 5 km north of Cleator.



Fig. 6b Hyaloclastic breccia 600 m south of Bluebell mine in unnamed tributary to Mineral Creek. Tributary runs parallel to Forest Route 93.



6c and d Contacts between pillowed basalt flows and breccia in Black Rock Canyon, south of outcrop shown in Fig. 6a. Basalt in Fig. 6c appears to have flowed over the breccia.



in the heterolithic breccias found in the Iron King Volcanics are rounded, but clasts are poorly sorted and no depositional fabric is evident in the breccias. The presence of rounded clasts in poorly sorted breccias indicates that these clasts were reworked.

Monolithic hyaloclastites are also relatively common in the Iron King Volcanics (Fig. 6b). These breccias contain lava fragments ranging in size from <1 cm to tens of centimeters and most likely form in situ (Fisher and Schmincke, 1984). Felsic tuffs in the Iron King Volcanics were most likely deposited as ash flows. This is indicated by “wispy streaks resembling flattened pumice” in the felsic rocks at Bluebell Mine as described by Vance (1989). As the weakest lithologic type in the Iron King Volcanics though, tuffs are highly deformed and layering from the flow is difficult to recognize.

Like pillow lavas, hyaloclastites indicate subaqueous eruption or flow of lava into water (Batiza and White, 2000). In addition to forming by thermal shock granulation, which is a quenching process during underwater eruption, they can also form by spalling of thin lava flows (Batiza and White, 2000). Most hyaloclastics in the Iron King Volcanics appear to have formed in situ from thermal shock granulation rather than in spalling off processes. However, fragments resembling pieces of basalt are present in some of the heterolithic breccias and may have formed by alternative shattering processes.

Primary textures

Primary textures are well preserved in the Iron King basalts south of Mayer. For example, basalt flows in Peck Canyon contain amygdules of quartz and calcite. One basalt outcrop in Peck Canyon contains a higher concentration of amygdules at the top of

flow layers. Amygdules were also observed by Vance (1989) in Cedar Creek basalts. In terms of grain sizes, a transition of coarse-grained to fine-grained textures were observed in one outcrop of massive basalt. Relatively fine-grained pillows are mixed with coarse fragments in some breccias (Fig. 6a). Ophitic to subophitic textures are evident in central parts of the basalt flows. Anderson and Blacet (1972a) presume that the original textures were intergranular or intersertal, typical of the rapid cooling expected in basalt flows.

Textural preservation is poor in the Iron King felsic units, but relict quartz phenocrysts are visible in thin section (Appendix A and Vance [1989]). Besides the flattened pumice fragments Vance (1989) observed at Blue Bell mine, he interpreted 25% plagioclase phenocrysts in samples collected northeast of Poland Junction as relict crystals. Textures in the volcanic rocks in close proximity to granitoid plutons are recrystallized, consistent with the observation that preservation of original texture decreases with greater degrees of deformation (Vance, 1989).

Area ore deposits

Lindberg (1989) provides several reviews of Paleoproterozoic ore deposits in Arizona. In his 1989 review, he states that Precambrian deposits have been significant sources of copper, zinc, lead, gold and silver although few Precambrian deposits in Arizona are being mined today. Most of the Precambrian ore came from massive sulfide deposits in the Yavapai Supergroup, with the majority from the Verde district at Jerome and the Big Bug district near Humboldt (Lindberg, 1989). The ore in both these districts are in the Spud Mountain Volcanics.

Anderson and Creasey (1958) described two types of Paleoproterozoic ore deposits in the Jerome area: massive sulfide and fissure vein deposits. Massive sulfide deposits comprise aggregates of sulfide minerals with little or no visible gangue minerals that are largely producers of metals. Although the massive sulfide deposits in the Jerome area are in the Spud Mountain Volcanics, they are similar to those found in the Iron King Volcanics. Fissure vein deposits formed by crystallizing of minerals in open space were mined for precious metals, such as gold and silver. Quartz vein silver and gold deposits are found southeast of the Iron King Volcanics; however, these appear to be Mesozoic to Tertiary and have no similarities to the ore deposits in the Iron King Volcanics. For this reason, the remainder of this section will focus on the massive sulfide deposits of the Iron King Volcanics.

Mining in the Iron King Volcanics was concentrated in the Mayer District during the first half of the 1900's. In 1989, the district ranked fourth in Arizona's total tonnage of massive sulfide ores, although DeWitt (1995) listed it as third in copper, silver and gold. Lindberg (1989) stated that the district produced 2.4% of the copper, 3% of the gold and 2.2% of the silver from this ore type. The significant producers of this district are the Blue Bell and the DeSoto mines (Fig. 3a). Blue Bell is by far the largest producer as the fifth largest massive sulfide deposit in the state in terms of ore tonnage (DeWitt, 1995). These two deposits are associated with Iron King rhyolites, either within them or at their contacts with basalt and andesite (DeWitt, 1995). Although none of the recent literature describes them, the Peck and Swastika mines near the DeSoto mine appear to originate in rhyolitic volcanics, based on a description by Lindgren (1926). He called the host rock a quartzite, a term he also used to describe the host rock of the DeSoto mine,

which, as already mentioned, was described as an Iron King rhyolite by DeWitt (1995). Four mines in the Big Bug mining district are considered massive sulfide deposits hosted in an upper felsic and andesitic unit of the Iron King Volcanics (Anderson and Blacet, 1972a). They are the Boggs, Iron Queen, Hackberry and Lone Pine mines. These four mines were operated during World War II for copper (Anderson and Blacet, 1972a). Unlike Anderson and Blacet, DeWitt (1995) placed the Hackberry mine at the same stratigraphic position as the Iron King mine, the top producing mine of the Big Bug district that is clearly contained in the Spud Mountain Volcanics.

Anderson and Creasey (1958) state that the massive sulfide deposits in the Yavapai Supergroup are largely controlled by structure. Veins or lenses form parallel to foliation or folds. The main sulfide minerals found in these deposits include pyrite, chalcopyrite, sphalerite and galena. Anderson and Creasey (1958) concluded that the deposits form by replacement or metasomatism, but later studies found that these deposits formed as precipitates from submarine hot springs on the sea floor and that they were modified by later hydrothermal action (Lindberg, 1989).

TECTONIC SETTINGS

To show that the Iron King Volcanics originated in an oceanic plateau setting, we must not only show that the volcanic sequence has similarities to oceanic plateau basalts (OPBs), but we must also show how it is dissimilar to the volcanic sequences produced in other tectonic settings.

Basalts are produced in numerous tectonic environments. They are generated at active margins of plates where subduction zones and spreading centers form, and they are generated within plates when magma from mantle plumes reaches the surface.

- Subduction zones produce continental and island arc basalts.
- Spreading centers produce basalts at mid-ocean ridges and back-arc basins.
- Intraplate settings have three types of basalt sequences that require the eruption of magma from mantle plumes at the earth's surface: Ocean island basalts (OIB) are generated as hot spots that produce relatively low volumes of basalt over a long period of time. Continental and oceanic flood basalts result when great volumes of mantle plume-derived magma are erupted in a relatively short period of time. Continental rifts provide a fourth location for intraplate basalt production; however, not all continental rifts have plume geochemical signatures, and those that remain active can develop into mid-ocean ridges.

Because of their intraplate, submarine origin, oceanic islands and oceanic plateaus are similar in many ways. As plume-derived features, the basalts of both carry a geochemical signature of their deep source, perhaps in the D" layer along the earth's core mantle boundary (Fig. 7). These basalts also show evidence of magma evolution during

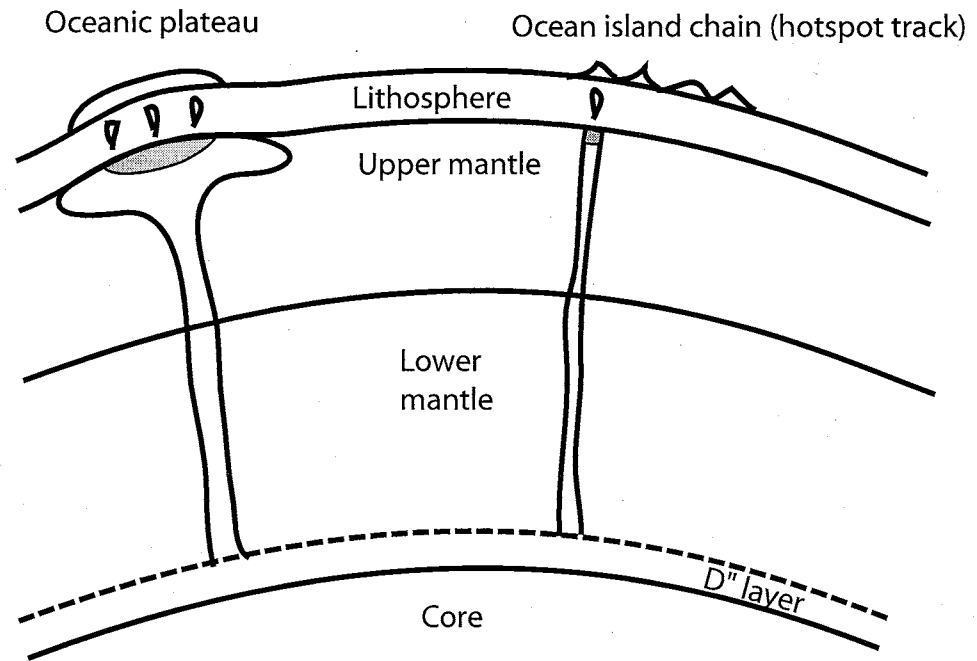


Fig. 7 Oceanic plateaus and ocean islands have a similar origin. Both are generated from a plume of hot buoyant solid that rises through the mantle from the D'' layer. The heated plume material is less viscous than the surrounding mantle and as a result can develop a plume head. Some researchers suggest that a plume head is the source for oceanic plateaus, while a plume tail that has lost its plume head is the source for ocean islands. The plume melts as it approaches the base of the lithosphere, here shown in gray. This melt may undergo fractional crystallization in lithospheric magma chambers before eruption.

partial melting of the mantle source material, which occurs in a plume at the base of the lithosphere and is relatively high for oceanic plateaus, and fractional crystallization of the resulting melt, which occurs in magma chambers at shallow depths within the lithosphere (Fig. 7). The large difference in eruption volume, and therefore size, of oceanic plateaus and ocean islands is related to the development of a plume head as the mantle plume moves through the mantle (Fig. 7). To develop a plume head, the plume material must be hotter and, as a result, have a lower viscosity than the surrounding mantle material (Davies, 1999; Condie, 2001). Several studies have suggested that an oceanic plateau and ocean islands can be produced by the same mantle plume (Davies, 1999). These studies suggest that basalts of the oceanic plateau are first erupted from the plume head. A moving plate carries the plateau and the underlying plume head from the location of the eruption while subsequent eruptions of the remaining plume tail create hot spot tracks (Davies, 1999).

To identify the tectonic environment where a particular basalt series formed, there are two lines of evidence we must review: lithologic and geochemical evidence.

Lithologic evidence

When examining lithologic evidence, the choices of tectonic environment can be reduced by considering whether a volcanic sequence was produced on land or under water and by considering other volcanics in addition to basalt. Pillow basalts and hyaloclastic breccias are two characteristic features of submarine eruption (Batiza and White, 2000). Iron formation, such as chert deposits, also require an aqueous environment for their generation (Gross, 1996a). The presence of these rock types in a

volcanic sequence rules out continental tectonic settings such as flood basalts, continental arcs and continental rifts. Eruptions of OPBs are dominated by basalt flows, as are ocean island eruptions and mid-ocean ridge eruptions. Continental and oceanic arc eruptions are dominated by volcanoclastic rocks (Campbell, 1999). Furthermore, continental volcanic sequences are either entirely mafic or bimodal felsic and mafic, rarely associated with andesites. Arc sequences, on the other hand, contain rocks ranging from felsic to mafic, with andesites composing an abundant component (Smith, 1992).

Rock types found in oceanic plateaus are similar to those reported by Corcoran (2000) for greenstones in the Archean Slave Province in the Northwest Territories, Canada. The Point Lake belt contains 50% massive and pillow basalts, 20% pillow breccias, 15% mafic dykes and sills, 10% massive flows and 5% hyaloclastite. Kerr et al. (1998) have developed an idealized lithologic sequence for oceanic plateaus from sections of the Caribbean Plateau that were obducted along the coasts of Columbia and Ecuador (Fig. 8). A layer of ultramafic rocks makes up the bottom unit. In ascending order are gabbros, high-MgO lavas such as picrites and komatiites, and shallow-level dolerite sheets. Pillow basalts cap the unit.

Most igneous textbooks provide idealized lithologic sequences for ophiolites, which are believed to represent mid-ocean ridges and back-arc basins. The sequence from bottom to top is tectonized harzburgites, ultramafic and mafic cumulates, noncumulate gabbros, a mafic sheeted dike complex, pillow lavas and a cap of sediments, usually pelagic sediments (Condie, 1997b). The major difference between ophiolites and oceanic plateaus is that oceanic plateaus lack sheeted dike complexes. If we wish to determine that a basaltic sequence is not a mid-ocean ridge remnant, but a remnant of an

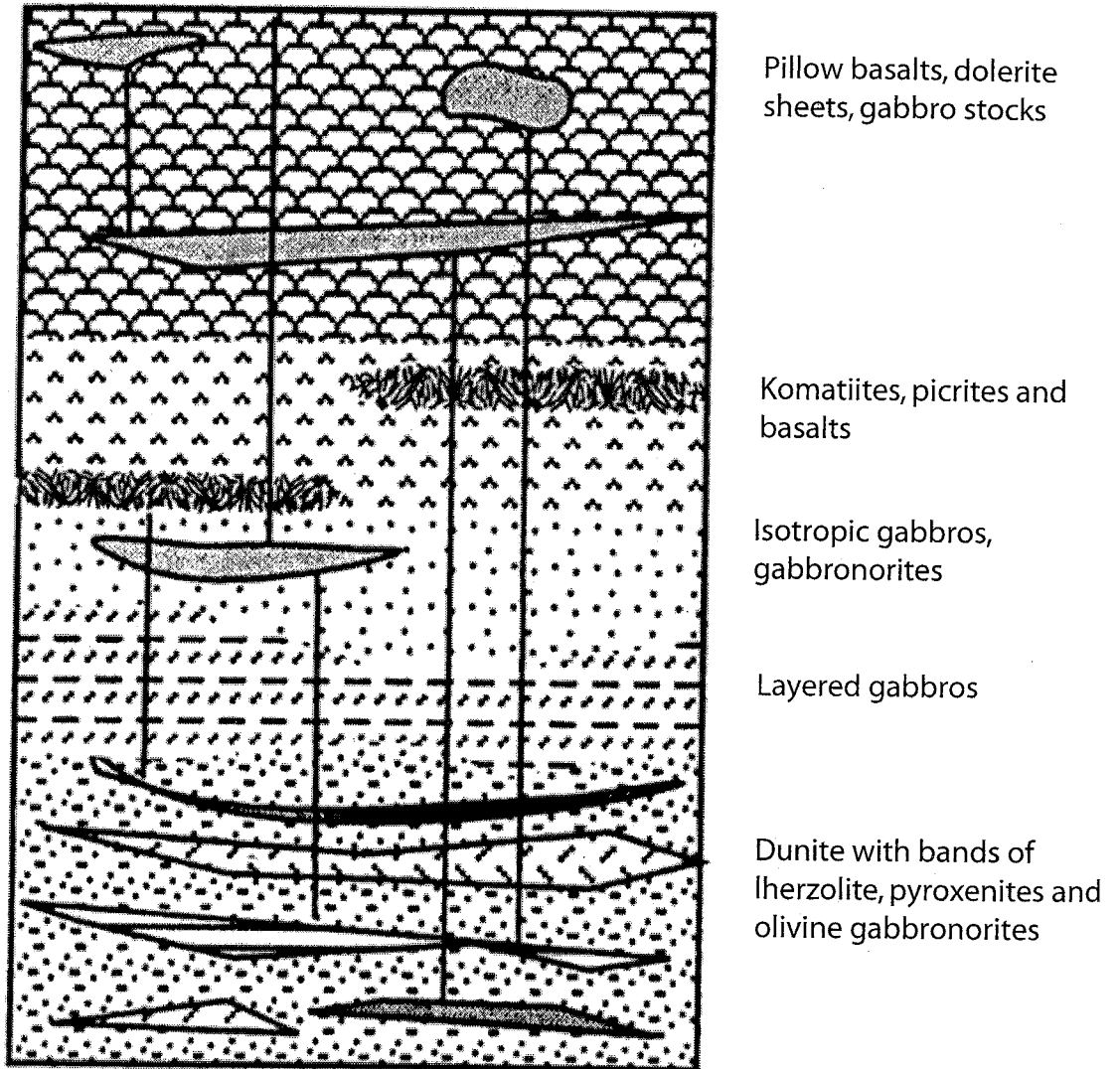


Fig. 8 Idealized lithologic sequence by Kerr et al. (1998) for sections of the Caribbean Plateau in Columbia and Ecuador.

oceanic plateau, we must use geochemical and isotopic characteristics. Back-arc basins, on the other hand, have an additional lithologic characteristic: as with other tectonic settings that form in the vicinity of arcs, they contain more pyroclastic rocks than oceanic plateaus.

Occasionally, some continental settings do not conform to idealized successions. Continental rifts can become inundated with fresh water or seawater, and continental flood basalts can flow into water resulting in submarine eruption. According to Cas and Wright (1987) the initial rift environment is subaerial with mafic to felsic and alkaline to peralkaline volcanics and may include thick pyroclastics. These lithologies decrease in abundance up-sequence as tholeiites similar to mid-ocean ridge basalt (MORB) and deep marine sediments increase in abundance. Smith (1992) and Green (1992) describe rift series composed of thick basalt flows with less abundant silicic volcanics during the early stages of development, and dikes and lavas with MORB geochemistry in the later stages. Green (1992) provides an additional description of important sedimentary assemblages found in continental rifts, generally related to subsiding basins and trailing edge margins. The sediments include immature fluvial sandstones and conglomerates, lacustrine deposits, evaporites, stable-shelf deposits, turbidites and pelites. Continental flood basalts have several other characteristics that, when used together, can help differentiate them from oceanic plateaus: they comprise extensive subaerial eruptions, the rocks from these eruptions are interlayered with terrestrial sediments and weathered horizons, and the volcanics are initially erupted onto eroded land surfaces (Kerr et al., 2000).

As mentioned, OIB are similar to OPB sequences because mantle plumes produce both sequences in oceanic settings. There are, however, several lithologic differences.

Kerr et al. (2000) state that OIB magmatism is focused at hot spots. When generated on moving plates, these eruptions result in island chains, seamounts and aseismic ridges. OIBs also undergo greater magmatic differentiation than oceanic plateaus (Kerr et al., 2000). For this reason, OIB eruptions include more rhyolitic, phonolitic and pyroclastic components. If lithologic differences, however, are not observed in an accreted terrane, trace element geochemistry can provide significant evidence about the tectonic source of the basalt.

Geochemical evidence

The use of geochemistry for tectonic discrimination cannot be considered alone, but combined with lithologic evidence it is important. The following review of geochemical diagrams does not cover every combination that will be used to discuss the Iron King Volcanics. Instead, only some of the most powerful and most widely used geochemical discrimination diagrams will be introduced.

As mentioned in the introduction, the geochemical signature characteristic of a particular tectonic setting is provided by HFSE, trace elements that are considered immobile in aqueous environments during alteration processes. The HFSE are considered incompatible in the solid phase, preferring the melt or liquid phase instead. Certain HFSE are considered more incompatible than others, and despite their immobile character, Nb and Ta behave differently from elements of the same incompatibility in wet tectonic environments such as subduction zones than others.

One of the most widely used geochemical diagrams is the incompatible-element distribution diagram (PMn diagram). In this diagram, each element is normalized to

primitive mantle values. By normalizing to the primitive mantle, deviations of the distribution of elements in the basalts from a primitive source are evident (Rollinson, 1993). In this study, the primitive mantle values reported by Sun and McDonough (1989) will be used.

The mobility and incompatibility of elements determine their order on a PMn graph. These characteristics are controlled by ionic potential (ionic charge/ionic radius) and bulk distribution coefficient. Pearce (1983) reviews this relationship: elements with low ionic potentials (<3) and very high ionic potentials (>12) are generally mobile, whereas elements with ionic potentials between these extremes tend to be immobile. The bulk distribution coefficient (or partition coefficient) is a measure of the compatibility of an element; that is, whether the element prefers to stay in the solid phase or if it prefers the liquid phase. Elements with bulk distribution coefficients much less than 1 are considered highly incompatible. Elements with bulk distribution coefficients greater than 1 are compatible. In terms of the PMn diagram, the most mobile and most incompatible elements are placed on the left side of the graph. All elements on the graph are considered incompatible; however, several exceptions occur when specific elements are controlled by a specific mineral phase. These exceptions include Y and Yb, which are highly compatible in garnet (Pearce, 1983). Unlike the low partition coefficients of other trace elements, the least incompatible elements, Tb through Lu, have partition coefficients for garnet that are greater than 1.

PMn graphs are particularly useful for understanding magmatic processes and for identifying magma sources in the mantle. Pearce (1983) shows that fractional crystallization and partial melting can change incompatible element concentrations but

generally preserves relative differences between elements. Source variations, on the other hand, will not only change the level of the graph, but cause variations within it (Pearce, 1983).

Average incompatible element distributions in basalts can vary among tectonic settings such as mid-ocean ridges, ocean islands, arcs, and the Ontong Java oceanic plateau (Fig. 9). Normal mid-ocean ridge basalts (N-MORB) have relatively flat incompatible element distributions, with depletion in the most incompatible elements from Th to Nd. According to Saunders and Tarney (1984), this implies that the parental magmas were derived from a source that has undergone previous melt extraction events. OIB, on the other hand, provide an increasingly enriched distribution from the least incompatible elements (on the right) to the most incompatible elements (on the left). Kerr et al. (2000) attribute this behavior to deep melting in the garnet stability field. Arc basalts, which have a relatively flat distribution compared to OIB, can be distinguished from basalts from the other three tectonic settings by an obvious depletion in Nb and Ta relative to Th and La. Condie (1994) attributes this characteristic to metasomatic processes at subduction zones. Th and La are soluble large ion lithophile elements that, when joined by saline water during subduction, separate from the subducting slab to enter the mantle wedge (Condie, 1994). And last, basalts from Ontong Java provide a flat incompatible element distribution, only slightly depleted in the most incompatible elements.

Kerr et al. (2000) has shown that OPBs can vary from a flat incompatible element distribution. Some have enriched incompatible trace element distributions that indicate melting in the garnet stability field or distributions with a positive Nb and Ta anomaly,

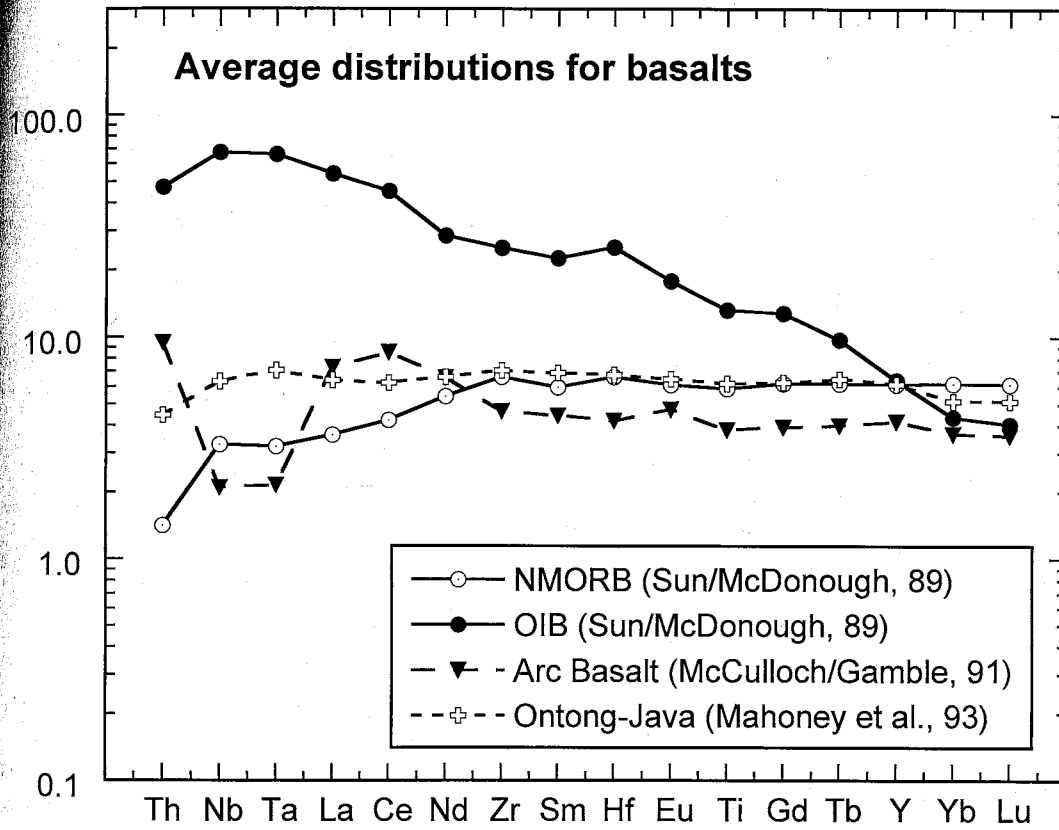


Fig. 9 Incompatible element distributions in normal mid-ocean ridge basalts (NMORB), arc basalts, ocean-island basalts (OIB), and Ontong-Java, the world's largest oceanic plateau. Values are normalized to primitive-mantle values of Sun and McDonough (1989).

indicating a source enriched by a subducted slab of crust. Variation from a flat distribution, found in many OPBs, to an enriched distribution, found in many OIBs, is also controlled by the degree of partial melting, related to the proximity of melting to the center of the plume. Melting generated nearer the center of the plume, which is hotter, is greater than melting that occurs further away in the plume head. A smaller degree of melt is more likely to occur in an ocean island mantle source that has been separated from the hot plume tail center by plate movement, as is the case of the Hawaiian islands (Condie, 2001).

A second important geochemical tool used in this study is the REE distribution diagram. REE diagrams are constructed in a similar manner to PMn diagrams, but only REE, those elements with atomic numbers 57 through 71, are plotted, and element concentrations are normalized to chondrite values (after Sun and McDonough [1989]). Normalization to chondrite values is necessary because REE with even atomic numbers tend to be more stable than REE with odd atomic numbers and REE with even atomic numbers tend to be more abundant (Rollinson, 1993). REE diagrams are plotted with the lightest REE on the left.

OIB is depleted in heavy REE, another characteristic attributed to deep melting in the garnet stability field (Kerr et al., 2000). OPBs generally have flat REE patterns, which according to Kerr et al. (2000) indicate either shallow melting or high degrees of melting. Basalts from arc settings may show enrichment in the light REE, another relict of subduction processes (Pearce, 1983), whereas MORB are depleted in light REE. The trace element geochemistry of back-arc basin basalts is transitional between arc basalts and MORB in terms of incompatible elements and REE (Saunders and Tarney, 1984).

Because most major elements are affected by alteration, they will not be considered in great detail in a discussion of the Iron King Volcanics. The behavior of Mg and Ni is useful for a discussion of tectonic environments in terms of how evolved the magma is, or how closely related it is to a primitive source. In this capacity, Mg and Ni serve as valuable indices of fractional crystallization. The more their concentrations decrease in basalts, the more evolved the magma is. Arc basalts are more evolved than OPB and OIB (Kerr et al., 2000). Nickel and MgO values are expected to be lowest for arc basalts. Ni values from several tectonic settings are as follows: arc basalts, 7 to 30 ppm (Condie, 2001); MORB and OPB, 40 to 140 ppm; average continental crust, 105 ppm (Abbott and Mooney, 1995); and Ontong Java basalts, 72-185 ppm (Abbott and Mooney, 1995).

These are only a few of the geochemical tools that will be used to discuss the tectonic origin of the Iron King Volcanics. However, concepts used to build and understand these basic geochemical diagrams and relationships are applied in the construction and discussion of other diagrams we will use, not just in terms of tectonic source characteristics, but also in terms of magmatic processes and mantle trace element distributions.

RESULTS

Most of the samples collected for this study were amphibolites from massive flow units and sills rather than pillowed flows. Because the main purpose of the sampling was to determine the geochemistry of the mantle source, only one felsic sample, a quartz-sericite schist, was collected. Outcrops of the Iron King Volcanics are predominantly in canyons, and eight canyons were chosen for sampling. An attempt was made to take at least a fist-sized sample at each location from only fresh outcrops. Twenty-three amphibolite samples were collected, in addition to the felsic sample, and sample locations are shown on Figure 10a-c. The maps also show locations where Vance (1989) collected 13 samples.

It was observed during sample collection that basalt flows dominate the southern portion of the Iron King Volcanics, whereas the northern part is dominated by felsic and andesitic volcanics (Condie, personal communication). Figure 11 demonstrates the distribution of lithologic types between the two components. In the southern section, basalt flows dominate with about 58%, whereas felsic and intermediate volcanics dominate the northern section with about 53% versus 31% basalt flows. The percent of chert is very similar (about 10%) between the two volcanic sequences, and the percent of breccia within the two sequences is within 10% of each other.

The samples that were gathered were visually screened for alteration and chlorite content, and those with the least amount of alteration and chlorite were chosen for chemical analysis. Eleven amphibolites and the felsic sample were chosen, as well as

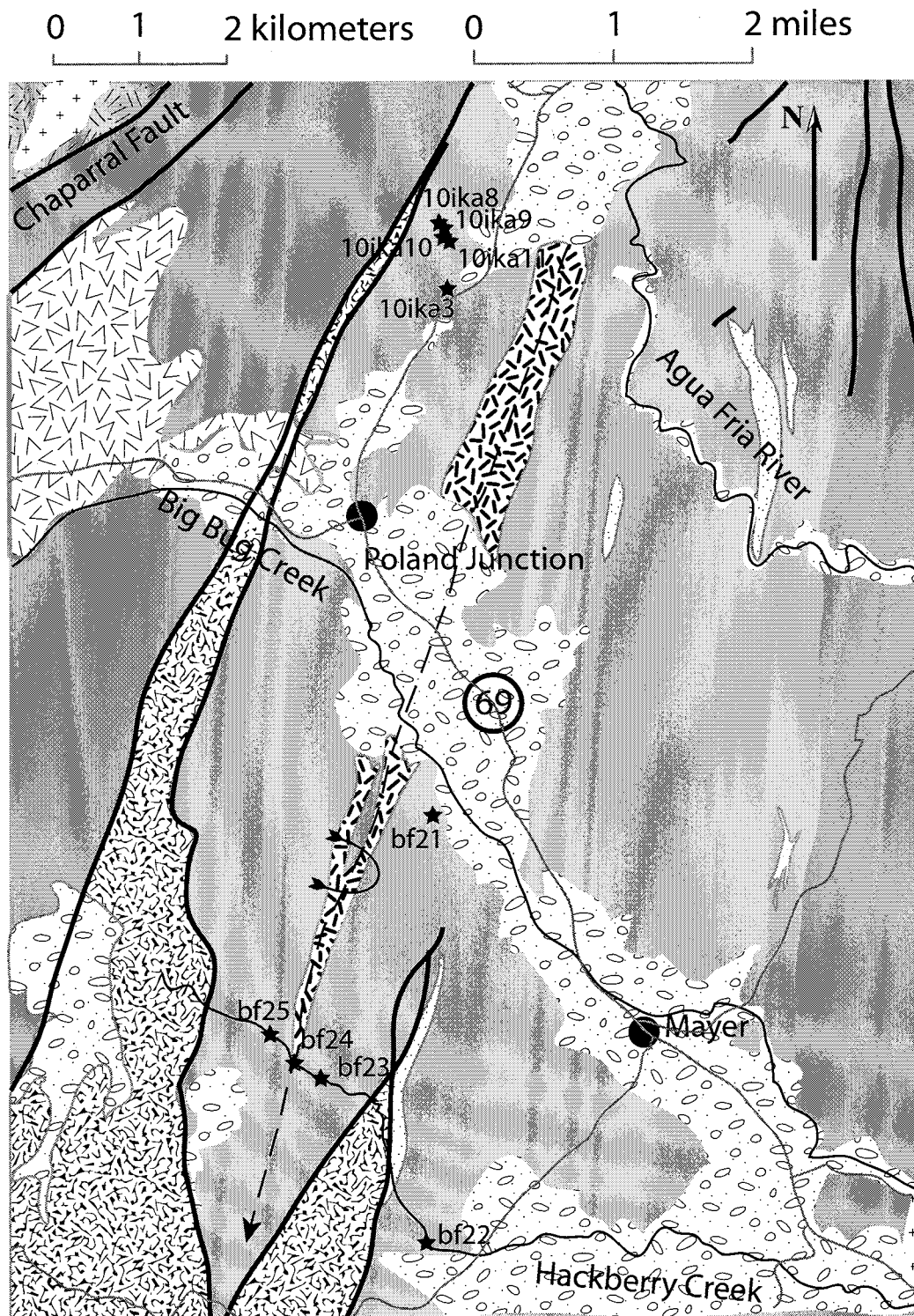


Fig. 10a Enlargement of northern section of Iron King Volcanics and the surrounding units. After Anderson and Blacet (1972b and c). Key listed on Fig. 10c.

0 1 2 kilometers

0 1 2 miles

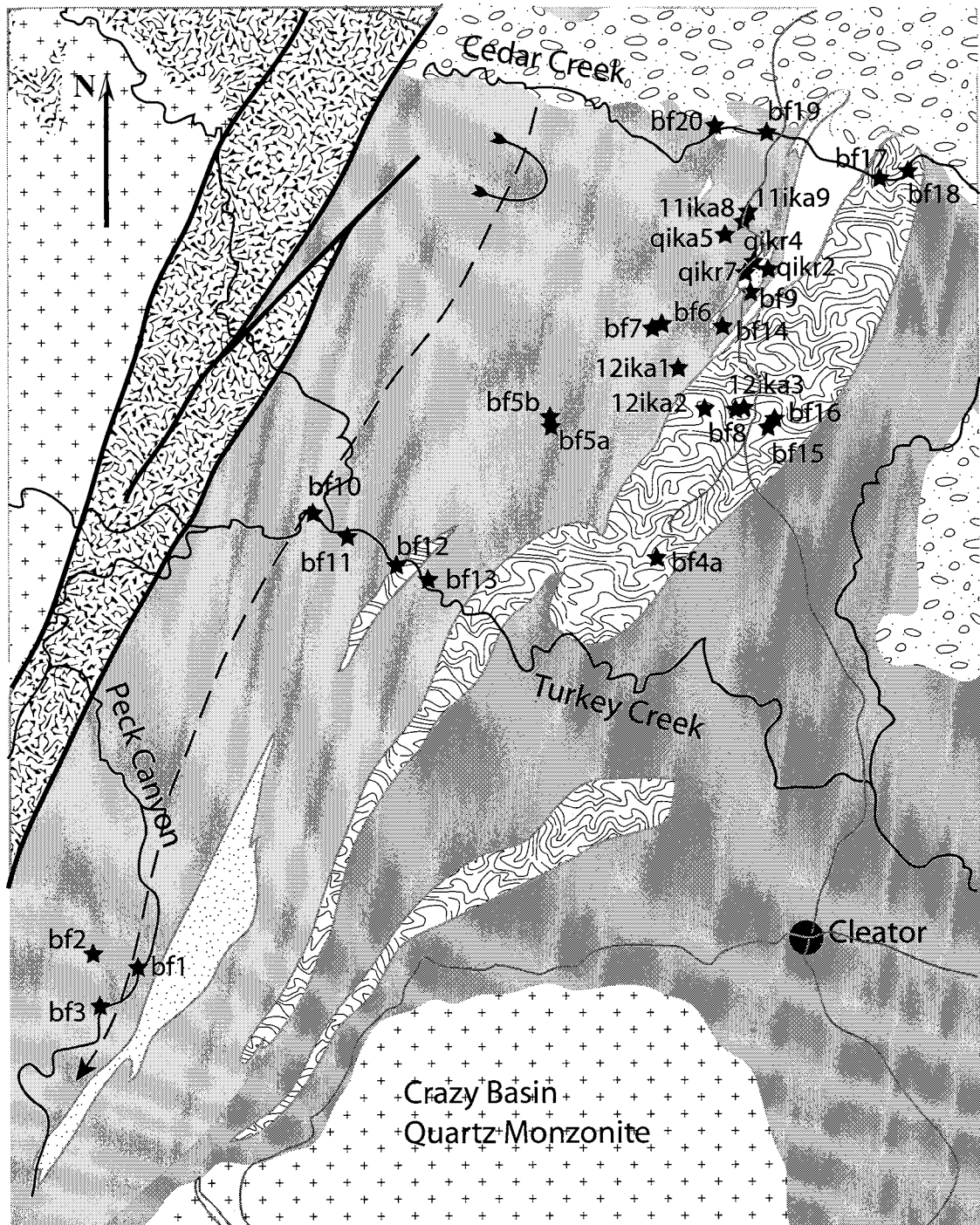


Fig. 10b Enlargement of southern section of Iron King Volcanics and the surrounding units. After Anderson and Blacet (1972b and c). Key listed on Fig. 10c.

Fig. 10c Key to geological map of Iron King Volcanics and surrounding formations



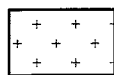
Tertiary and Quaternary sediments



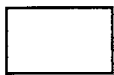
Texas Gulch formation -- sandstone, tuff, slate, limestone and conglomerate



Tertiary granodiorite



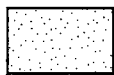
Precambrian intrusives -- includes granites, granodiorite, Alaskite, quartz monzonite, gabbro and quartz porphyry



IKC -- ferruginous chert beds



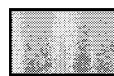
IKAB -- mafic flows at base of Iron King Volcanics interbedded with chert, carbonate and breccia



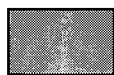
IKR -- bedded tuffs with sericitic base



IKAT -- andesitic-rhyolitic tuffaceous rocks



IKA -- andesitic and basaltic amygdaloidal and pillow flows



Spud Mountain Volcanics



Green Gulch Volcanics



Fault line



Rivers



Roads



Plunging syncline

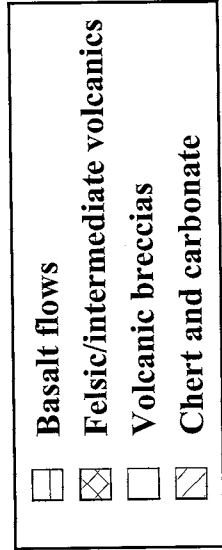
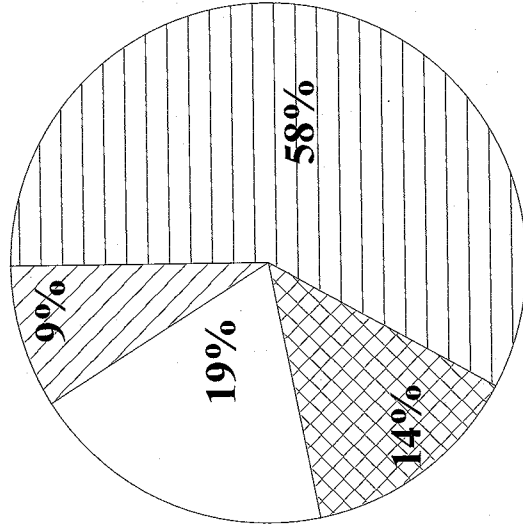
● Town

● Mine

* Sample location

Ⓢ Highway

Southern section



Northern section

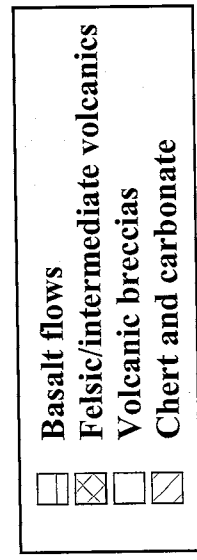
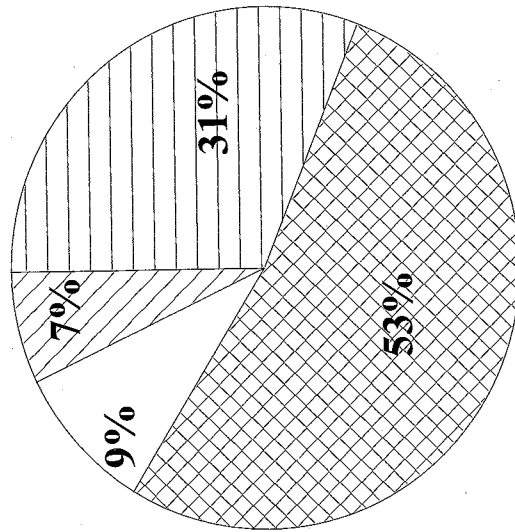


Fig. 11 Pie charts showing the distributions of eruption types characteristic of the northern and southern sections of the Iron King Volcanics. Basalt flows include massive and pillowed flows. Felsic/intermediate volcanics include lava flows and volcaniclastic and pyroclastic material excluding breccias, which are grouped in their own category.

two amphibolite samples previously analyzed by Vance (1989) by XRF. Major element concentrations were determined by standard X-ray fluorescence spectrometry (XRF) at XRAL Laboratories, Don Mills, Ontario. Trace elements were analyzed using inductively coupled plasma mass spectrometry (ICP-MS) on a Perkin Elmer Elan 5000 in the Department of Geological Sciences, University of Saskatchewan. Further discussion of the methods used is included in Appendix B. In addition to the 14 samples analyzed, discussion of the Iron King Volcanics will include the data for 11 samples analyzed by Vance (1989).

Major and trace element results are listed on Table 2. The samples are split into four geochemical groups: enriched plume (five samples), nonenriched plume (eight samples), mafic arc (eight samples), and felsic arc (four samples). The rationale behind the divisions will be explained in the trace elements section.

Classification

Unlike fresh volcanic rocks, Precambrian rocks such as the Iron King basalts cannot be classified using major element schemes such as total alkali versus silica diagrams, because the major elements used in such diagrams (K, Na and even Si) are highly susceptible to remobilization during alteration. Instead, classification schemes that use trace elements that are generally immobile during sea floor alteration, metamorphism and weathering have been used. These trace elements include the HFSE (Th, Nb, Ta, Zr, Hf, Ti and Y), REE and transition metals (Winchester and Floyd, 1977; Polat et al., 1998).

Winchester and Floyd (1977) suggested using Zr/TiO_2 and Nb/Y distributions as

Table 2 Major and trace element results for the Iron King Volcanics. Table continues on following page. Samples named "bf" or followed with the initial "r" were analyzed at the University of Saskatchewan. Samples followed by the initial "v" were analyzed by Vance (1989) on XRF. na = not analyzed. nd = not detected. Standard deviation is provided for those elements that were analyzed more than once.

Sample	* Std dev	Enriched Plume					Nonenriched Plume, Group A					Nonenriched Plume, Group B				
		bf1	bf3	bf4a	bf5b	bf17	bf24	12lka1v	12lka3v	11lka10f	bf10	bf14	bf22	12lka2f		
SiO ₂ (wt %)	--	47.9	46.2	48.0	48.9	45.0	48.3	50.7	50.0	46.1	48.6	47.6	47.2	48.5		
TiO ₂ (wt %)	--	2.10	1.73	1.96	1.79	2.27	0.80	1.15	1.08	1.11	1.35	1.45	1.09	1.15		
Al ₂ O ₃ (wt %)	--	15.4	13.0	12.9	12.9	15.3	14.1	15.7	14.9	15.6	13.1	15.0	14.1	14.7		
Fe ₂ O ₃ T (wt %)	--	14.2	13.2	14.0	14.4	16.0	12.1	12.9	12.0	13.9	14.8	13.3	13.4	13.8		
MgO (wt %)	--	6.1	7.7	8.1	6.6	8.0	8.7	7.0	7.3	7.2	7.7	7.5	7.7	7.3		
CaO (wt %)	--	8.3	10.0	9.7	10.3	4.3	12.1	6.2	8.8	12.8	8.9	8.3	10.1	10.1		
Na ₂ O (wt %)	--	2.8	3.9	3.3	2.5	1.9	2.0	5.6	3.4	1.5	3.1	2.7	2.7	3.6		
K ₂ O (wt %)	--	1.2	0.18	0.20	0.22	0.52	0.16	0.08	0.42	0.19	0.20	0.30	0.17	0.22		
MnO (wt %)	--	0.14	0.17	0.23	0.21	0.14	0.18	0.17	0.17	0.16	0.23	0.15	0.19	0.18		
P ₂ O ₅ (wt %)	--	0.22	0.19	0.20	0.20	0.21	0.06	0.10	0.09	0.10	0.14	0.12	0.10	0.10		
LOI (wt %)	--	1.3	3.8	1.1	0.90	6.7	1.4	0.90	1.5	1.4	1.8	2.7	3.3	0.85		
Total	--	99.64	100.05	99.69	98.89	100.17	99.862	100.39	99.6	99.98	99.85	99.2	100.03	100.51		
Rb (ppm)	0.07	21.0	2.1	1.0	0.70	12.0	9.0	2.0	11.0	1.0	10.0	3.5	13.0	13.0		
Ba (ppm)	0.5	141	186	33	86	36	30	10	70	26	51	43	64	51		
Sr (ppm)	2.7	194	276	264	303	82	167	92	107	235	163	141	198	138		
Th (ppm)	0.045	1.7	0.84	0.91	1.5	1.2	0.24	0.40	0.50	0.35	0.76	0.73	0.60	0.70		
U (ppm)	0.020	0.42	0.16	0.29	0.36	0.42	0.09	na	na	na	0.14	0.18	0.12	0.12		
Sc (ppm)	2.9	51	46	42	44	57	28	49	43	53	53	52	52	48		
V (ppm)	0.35	525	395	394	411	514	316	321	408	373	366	434	365	389		
Cr (ppm)	--	66	164	76	73	80	166	183	175	417	145	61	144	160		
Co (ppm)	--	47.4	42.5	49.7	55.6	61.8	54.6	56.3	52.4	64.0	60.1	60.2	59.2	55.0		
Ni (ppm)	--	47	88	53	61	68	99	102	109	183	69	93	90	88		
Y (ppm)	--	30	24	24	27	25	16	24	19	22	27	25	19	21		
Zr (ppm)	1.1	150	96	132	136	120	45	73	67	49	81	91	58	66		
Nb (ppm)	1.7	14.3	8.8	10.3	12.6	10.2	2.6	6.0	5.5	4.3	6.0	5.7	4.4	5.0		
Hf (ppm)	0.11	4.3	3.0	3.2	3.6	3.4	1.5	2.1	1.9	1.5	2.4	2.8	1.7	2.2		
Ta (ppm)	0.057	0.81	0.53	0.57	0.76	0.64	0.17	0.34	0.30	0.24	0.38	0.38	0.27	0.28		
La (ppm)	0.21	13.1	8.5	9.5	11.9	11.8	2.8	3.0	2.8	3.4	5.4	5.8	4.1	3.9		
Ce (ppm)	0.4	30.8	21.2	24.4	29.4	28.6	7.1	9.0	9.0	9.5	14.0	14.4	10.6	9.9		
Pr (ppm)	0.03	4.0	2.9	3.5	4.1	3.8	1.1	na	na	1.5	2.0	2.1	1.5	1.5		
Nd (ppm)	0.18	19.0	14.5	17.1	18.9	18.6	5.5	7.9	6.9	7.6	9.9	10.5	7.7	7.5		
Sm (ppm)	0.34	5.5	4.1	4.6	4.9	4.9	1.8	2.5	2.1	2.6	2.9	3.2	2.4	2.5		
Eu (ppm)	0.08	1.9	1.4	1.5	1.6	1.7	0.69	0.9	0.78	0.96	1.1	1.2	0.85	0.92		
Gd (ppm)	0.09	6.0	5.1	5.5	5.8	5.6	2.5	3.3	2.8	3.3	4.2	4.3	3.1	3.5		
Tb (ppm)	0.039	1.1	0.84	0.93	0.96	0.94	0.47	0.60	0.52	0.57	0.73	0.72	0.52	0.61		
Dy (ppm)	0.03	5.8	4.8	5.2	5.5	5.1	3.0	na	na	3.7	4.9	4.6	3.5	3.9		
Ho (ppm)	0.009	1.2	1.0	1.1	1.1	1.0	0.66	na	na	0.80	1.1	0.98	0.76	0.84		
Er (ppm)	0.021	3.4	2.8	2.9	3.2	2.8	2.0	na	na	2.3	3.1	2.9	2.2	2.4		
Tm (ppm)	0.005	0.51	0.39	0.40	0.45	0.40	0.29	na	na	0.33	0.46	0.42	0.32	0.35		
Yb (ppm)	0.024	3.4	2.5	2.5	2.8	2.5	1.9	2.1	2.0	2.1	3.0	2.8	2.1	2.3		
Lu (ppm)	0.005	0.60	0.42	0.45	0.47	0.43	0.35	0.33	0.33	0.38	0.51	0.47	0.34	0.39		

* Analytical precision based on replicate analyses of the reference material. Duplicates analyses were not performed for all elements.

Table 2 (cont.)

Sample	Arc Group Mafic										Arc Group Felsic									
	bf6	bf13	10lka3v	10lka6v	10lka9v	10lka10v	10lka11v	qika5v	bf9	qikr2v	qikr4v	qikr7v	bf9	qikr2v	qikr4v	qikr7v				
SiO ₂ (wt %)	49.9	53.6	50.7	51.3	55.2	54.3	54.2	53.6	77.3	78.0	89.4	83.8	77.3	78.0	89.4	83.8				
TiO ₂ (wt %)	1.0	0.98	2.4	0.75	0.72	0.72	0.74	1.8	0.16	0.13	0.13	0.11	0.16	0.13	0.13	0.11				
Al ₂ O ₃ (wt %)	13.9	12.7	12.8	17.4	15.1	16.3	16.7	15.9	12.7	11.8	7.0	7.3	12.7	11.8	7.0	7.3				
Fe ₂ O _{3T} (wt %)	12.2	10.3	15.8	10.0	9.8	10.5	10.7	8.9	1.2	2.2	0.22	2.7	1.2	2.2	0.22	2.7				
MgO (wt %)	7.6	3.2	3.7	4.1	4.1	3.6	3.8	2.4	0.40	2.4	0.20	3.0	0.40	2.4	0.20	3.0				
CaO (wt %)	9.5	7.8	8.1	6.8	5.2	8.8	8.3	7.6	0.10	0.26	0.03	0.07	0.10	0.26	0.03	0.07				
Na ₂ O (wt %)	3.2	2.1	3.2	4.6	3.3	2.0	2.2	3.4	0.12	1.7	0.19	0.03	0.12	1.7	0.19	0.03				
K ₂ O (wt %)	0.18	2.7	0.23	0.08	0.83	0.27	0.28	1.9	6.7	1.2	1.9	1.1	6.7	1.2	1.9	1.1				
MnO (wt %)	0.18	0.60	0.27	0.17	0.16	0.19	0.18	0.09	0.01	0.01	0.00	0.02	0.01	0.01	0.00	0.02				
P ₂ O ₅ (wt %)	0.11	0.18	0.98	0.14	0.14	0.14	0.14	0.48	0.01	0.01	0.01	0.03	0.01	0.01	0.01	0.03				
LOI (wt %)	1.1	5.5	1.9	4.9	5.0	3.6	3.5	3.7	1.4	2.2	1.0	2.0	1.4	2.2	1.0	2.0				
Total	98.793	99.59	100	100.21	99.4	100.32	100.59	99.74	100.022	99.892	100.066	100.171	100.022	99.892	100.066	100.171				
Rb (ppm)	0.5	76.0	11.0	2.0	18.0	7.0	7.0	52.0	48.0	13.0	15.0	7.0	48.0	13.0	15.0	7.0				
Ba (ppm)	18	518	147	65	315	196	217	130	394	120	200	120	394	120	200	120				
Sr (ppm)	172	121	305	429	240	490	415	136	16	88	18	7	16	88	18	7				
Th (ppm)	0.72	2.4	2.5	1.4	1.4	1.5	1.5	3.0	5.2	5.3	3.5	3.8	5.2	5.3	3.5	3.8				
U (ppm)	0.28	1.1	1.4	0.80	1.0	0.90	1.1	1.6	1.7	2.1	1.4	1.5	1.7	2.1	1.4	1.5				
Sc (ppm)	48	27	27	33	35	36	35	26	7	5	1	2	7	5	1	2				
V (ppm)	326	176	215	265	237	260	262	166	3	nd	nd	nd	3	nd	nd	nd				
Cr (ppm)	314	154	6	24	28	24	25	nd	2.5	nd	nd	nd	2.5	nd	nd	nd				
Co (ppm)	54.2	29.4	19.3	27.1	29.3	31.6	29.7	46.7	1.5	0.60	0.30	5.5	1.5	0.60	0.30	5.5				
Ni (ppm)	131	55	10	12	13	12	5	7	2	nd	nd	nd	2	nd	nd	nd				
Y (ppm)	24	33	45	18	17	18	18	44	44	41	32	44	44	41	32	44				
Zr (ppm)	92	150	277	87	79	78	80	249	289	173	143.8	157	289	173	143.8	157				
Nb (ppm)	1.8	11.0	11.3	4.3	4.8	3.7	5.6	19.1	9.9	22.3	12.6	12.8	9.9	22.3	12.6	12.8				
Hf (ppm)	2.9	4.2	4.9	2.3	2.4	2.2	2.3	6.7	9.1	6.7	4.3	4.5	9.1	6.7	4.3	4.5				
Ta (ppm)	0.09	0.73	0.55	0.24	0.21	0.22	0.29	1.1	0.71	1.5	0.84	0.96	0.71	1.5	0.84	0.96				
La (ppm)	8.2	15.4	19.9	9.2	11.4	10.0	11.4	25.2	20.4	38.2	21.6	41.3	20.4	38.2	21.6	41.3				
Ce (ppm)	18.9	37.3	47.6	25.6	26.9	27.4	26.8	64.2	44.9	80.3	38.0	103	44.9	80.3	38.0	103				
Pr (ppm)	2.5	4.7	na	na	na	na	na	na	5.5	na	na	na	5.5	na	na	na				
Nd (ppm)	11.5	20.1	na	12.8	9.9	12.8	11.7	37.3	21.8	18.6	20.0	38.9	21.8	18.6	20.0	38.9				
Sm (ppm)	3.1	5.5	8.5	2.7	3.6	3.0	3.6	7.9	5.1	7.9	7.5	10.8	5.1	7.9	7.5	10.8				
Eu (ppm)	1.2	1.3	2.1	0.93	0.99	1.0	1.0	2.5	1.3	1.2	1.3	2.0	1.3	1.2	1.3	2.0				
Gd (ppm)	4.0	5.6	7.7	2.7	3.0	2.3	2.8	6.9	6.6	8.0	7.3	9.6	6.6	8.0	7.3	9.6				
Tb (ppm)	0.74	1.1	1.2	0.44	0.44	0.46	0.40	1.0	1.3	1.3	1.2	1.5	1.3	1.3	1.2	1.5				
Dy (ppm)	4.4	6.0	na	na	na	na	na	na	7.8	na	na	na	7.8	na	na	na				
Ho (ppm)	0.92	1.2	na	na	na	na	na	na	1.7	na	na	na	1.7	na	na	na				
Er (ppm)	2.7	3.7	na	na	na	na	na	na	4.8	na	na	na	4.8	na	na	na				
Tm (ppm)	0.40	0.56	na	na	na	na	na	na	0.67	na	na	na	0.67	na	na	na				
Yb (ppm)	2.6	3.7	4.9	1.7	2.1	2.0	2.1	4.8	4.1	4.4	3.0	6.9	4.1	4.4	3.0	6.9				
Lu (ppm)	0.53	0.64	0.71	0.30	0.38	0.33	0.37	0.85	0.74	0.74	0.46	1.05	0.74	0.74	0.46	1.05				

an igneous rock classification scheme. The Zr/TiO₂ and Nb/Y ratios are both indices of alkalinity, but only Zr/TiO₂ is an index of fractional crystallization; therefore the combination provides a powerful tool for classifying rocks. Figure 12 shows the Iron King Volcanics plotted on a Zr/TiO₂ vs. Nb/Y diagram with fields from Winchester and Floyd (1977). The felsic arc samples fall in the rhyolite field, as would be expected by their high silica concentrations, while most of the other Iron King Volcanics fall within the tholeiite and basaltic-andesite fields. Throughout this report, the basaltic andesites will be listed with the mafic samples.

Once a tholeiitic rock type is identified, a volcanic series can also be identified using immobile trace elements. MacLean and Barrett (1993) established the Y-Zr plot for this purpose. Most of the Iron King samples fall in the tholeiitic series, and some fall in the transitional series (Fig. 13). None fall in the calc-alkaline field. Samples that fall in the transitional field not only include the arc samples, but some of the plume-derived rocks.

Major elements

Because of the mafic composition of most of the Iron King Volcanics, the major element distributions of the samples are evaluated on variation diagrams with MgO, rather than SiO₂, as the principle variable (Fig. 14a-g). Most of the major elements show no trends among the Iron King samples other than to separate arc samples from plume samples. However, TiO₂ and P₂O₅ separate the plume samples into two groups, the enriched and nonenriched plume groups (Fig. 15a-b). The enriched samples have the highest TiO₂ and P₂O₅ values.

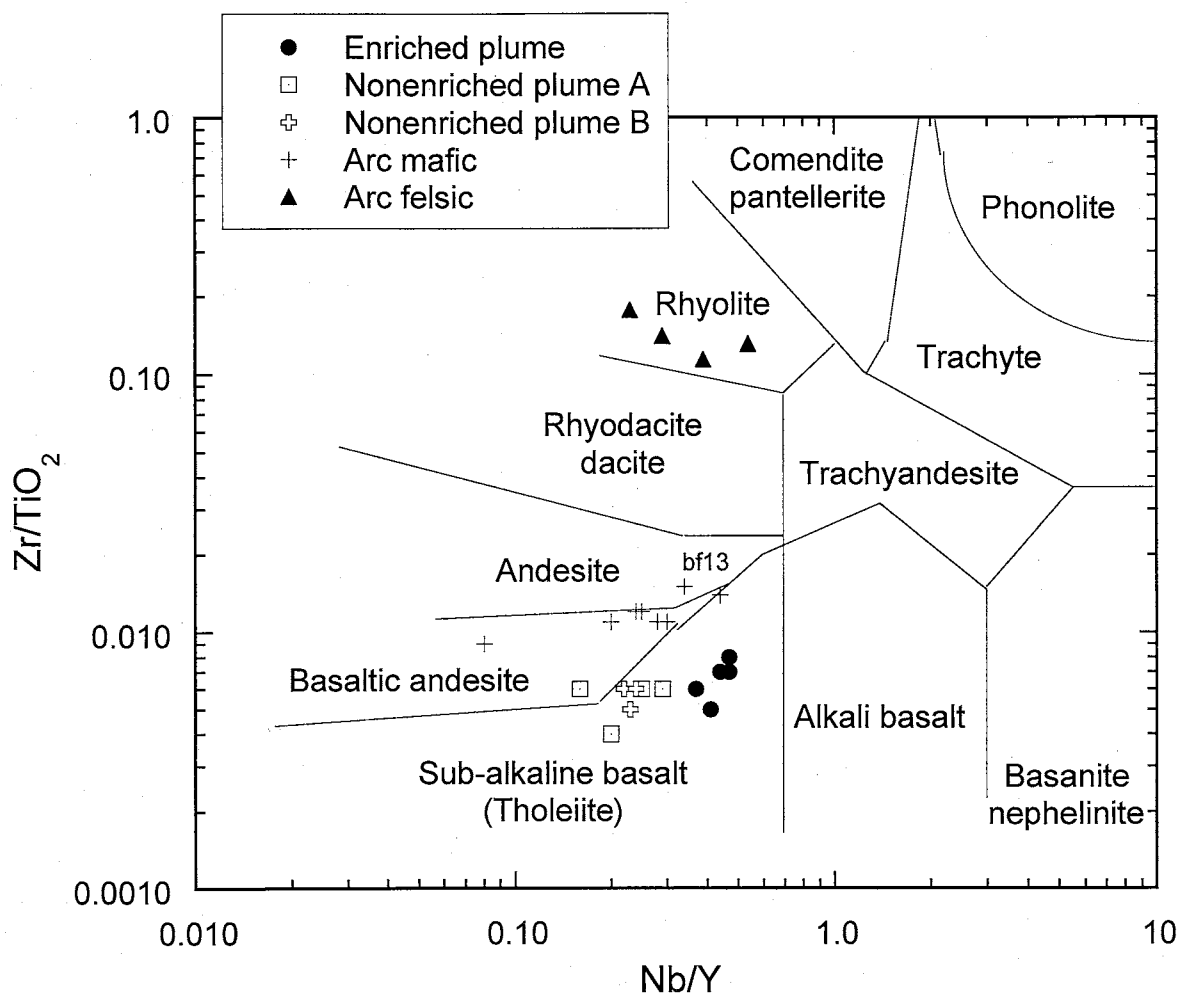


Fig. 12 Trace element diagram from Winchester and Floyd (1977) used to classify rocks from the Iron King Volcanics.

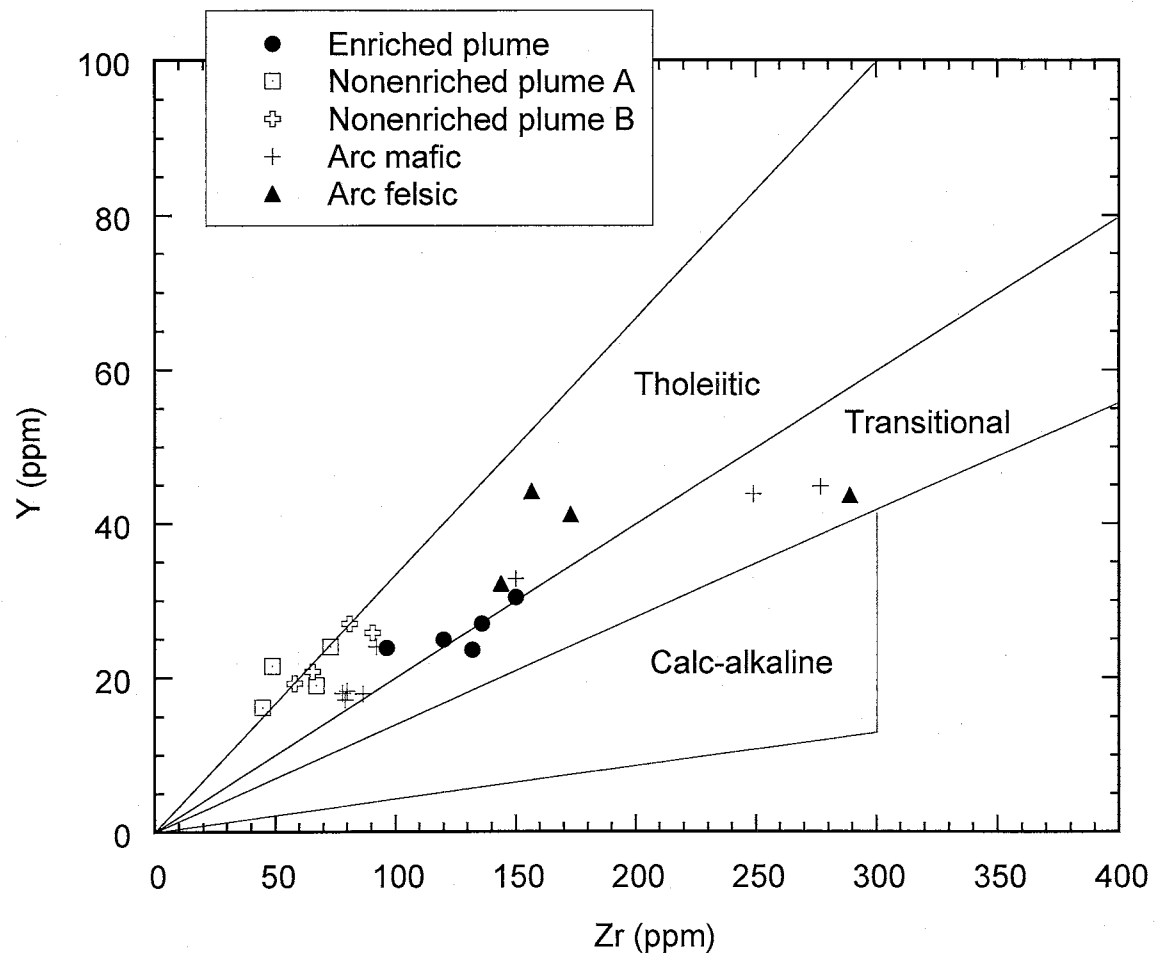
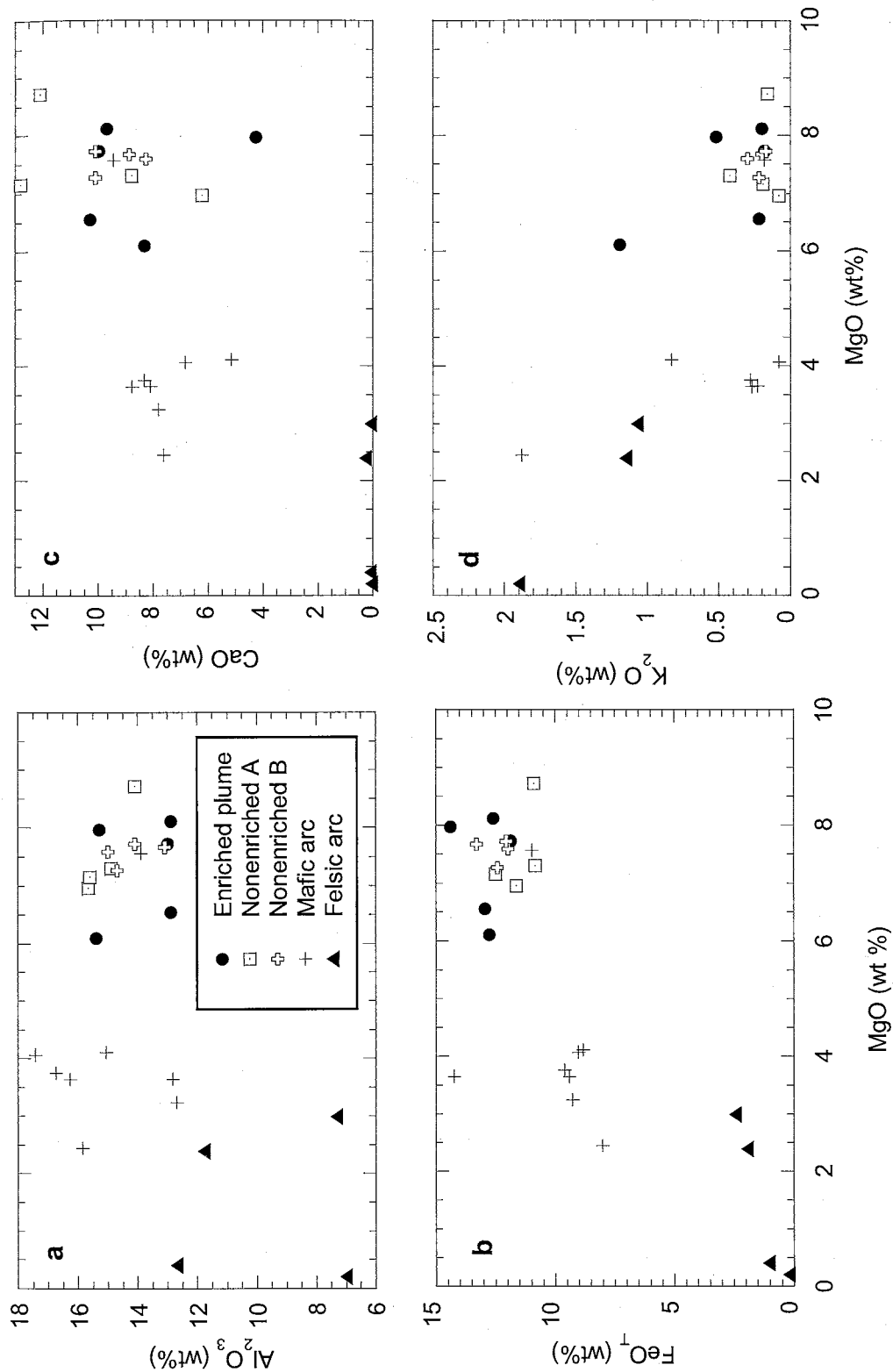


Fig. 13 Volcanic series showing the distribution of the Iron King Volcanics. Boundaries from MacLean and Barrett (1993).



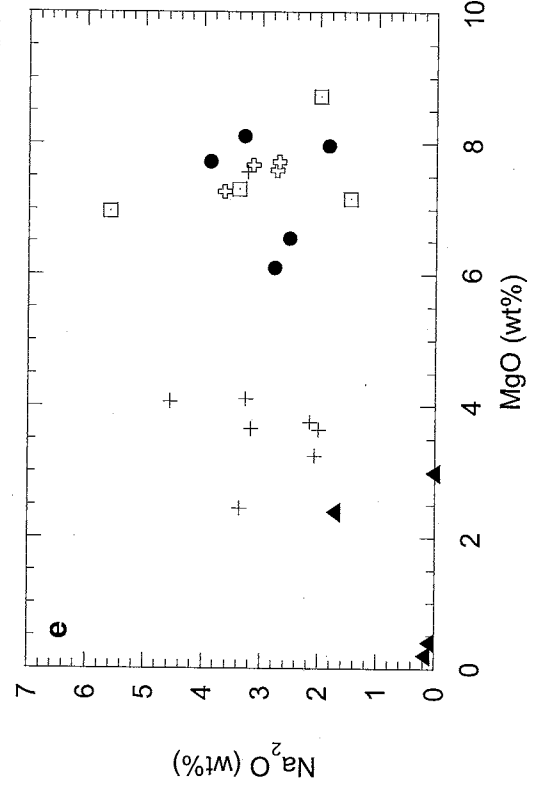
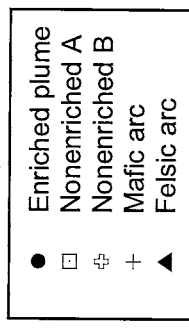
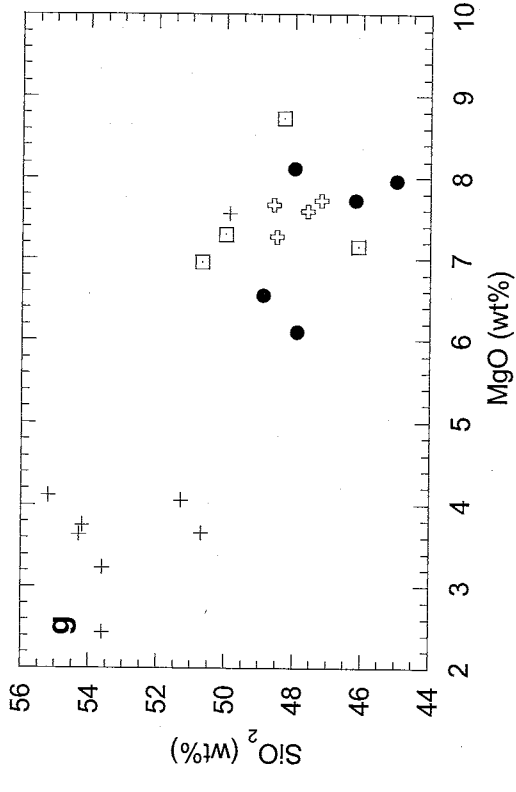
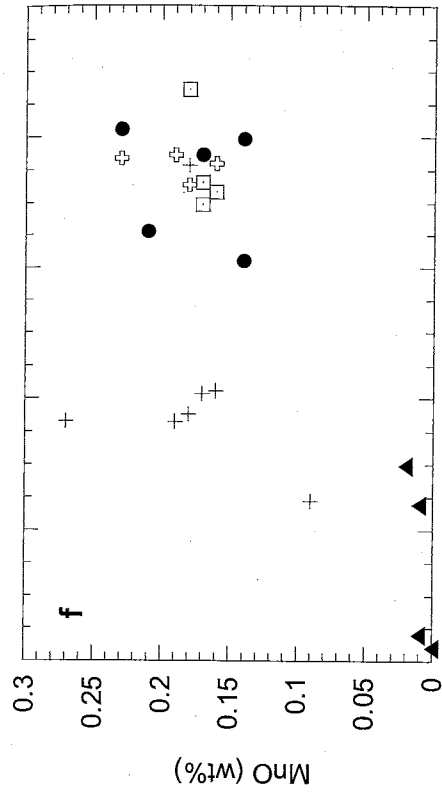


Figure 14a-g (Continued from previous page.)

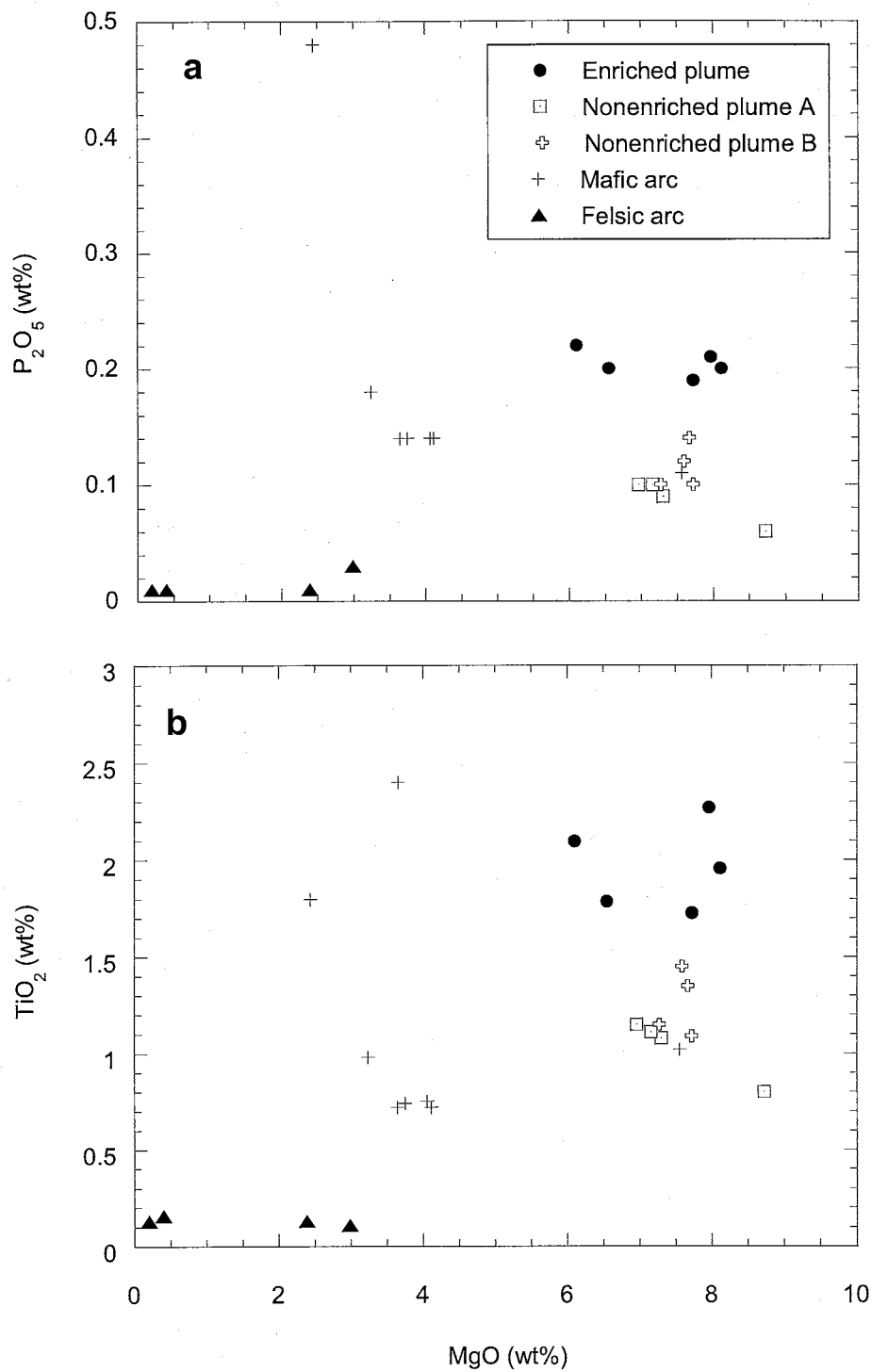


Figure 15a-b Phosphorus and titanium oxide variation diagrams for Iron King Volcanics. Key is the same for both diagrams.

Trace elements

The four geochemical groups in the Iron King Volcanics are defined by incompatible and REE distributions. The groups are referred to as (1) enriched plume, (2) nonenriched plume, (3) mafic arc and (4) felsic arc groups (Figs. 16a-f and 17a-f). The groups were identified by plotting data from known tectonic settings of basalts from normal mid-ocean ridges, ocean islands, arcs and oceanic plateaus as introduced in the tectonic setting section.

Plume versus arc components

The most obvious step in establishing subdivisions among the Iron King Volcanics is distinguishing between two tectonic settings. Several of the Iron King rocks are missing the negative Nb-Ta anomaly characteristic of arc volcanics (Fig. 16d-f); however, a significant number of the rocks carry this signature. The rocks that do not show a negative Nb-Ta anomaly or show a positive Nb-Ta anomaly are referred to as the Iron King plume volcanics. These are rocks that show either flat incompatible and REE distributions or distributions enriched in the most incompatible elements and light REE. The second component is referred to as the Iron King arc volcanics.

Arc volcanics

The most important characteristic of the Iron King arc volcanics is the depletion of Nb and Ta relative to surrounding incompatible elements (Fig. 16a-c). These anomalies are attributed to the strong immobility of Nb and Ta in aqueous fluids rising from subducted slabs into the mantle wedge (Condie, 1986; Saunders, 1984; Pearce,

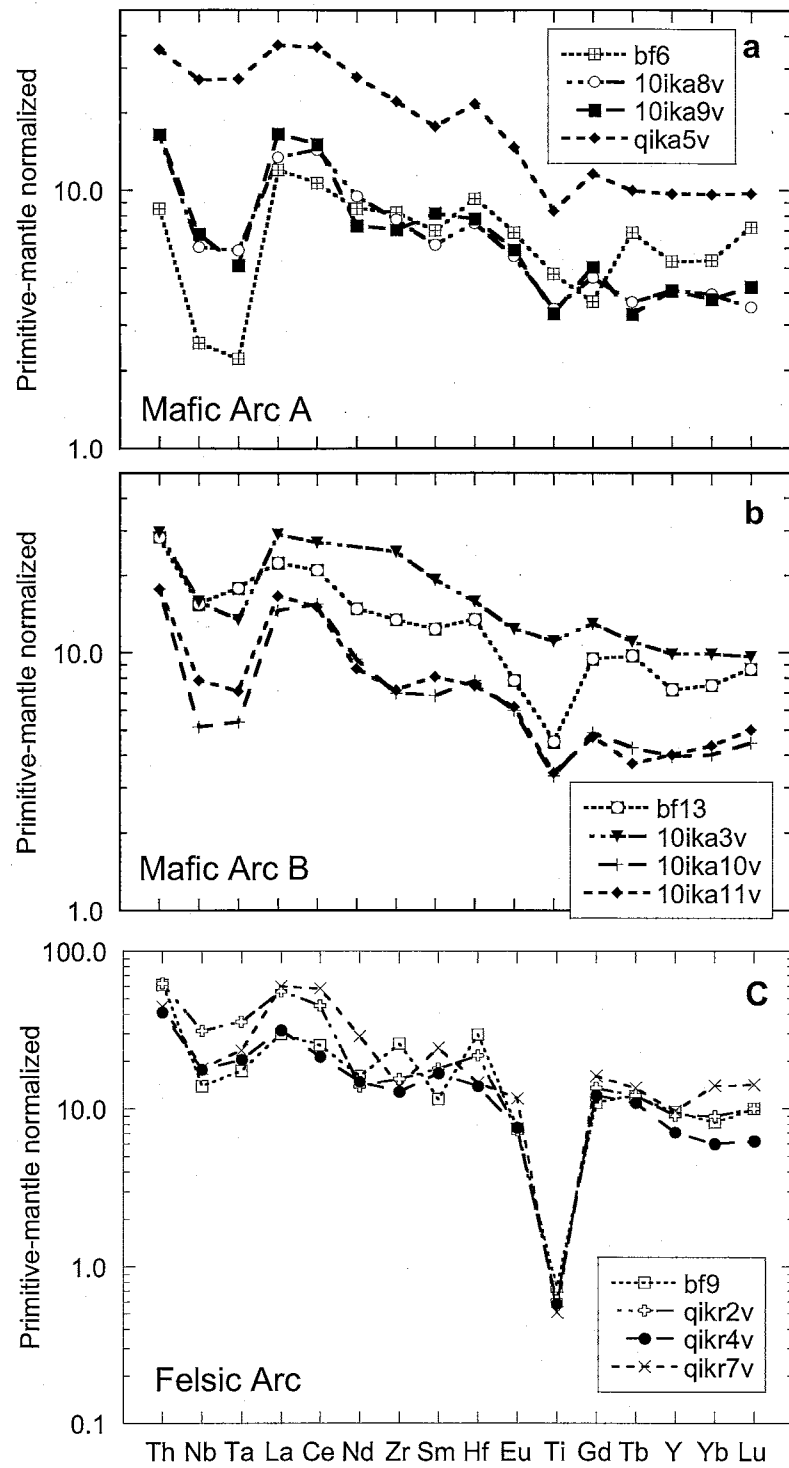


Figure 16a-f Primitive-mantle normalized graphs of the Iron King Volcanics. Primitive-mantle values from Sun and McDonough (1989). Incompatibility of elements increase from right to left. Notice the negative Nb and Ta anomalies and in some cases negative Ti anomalies of a, b and c.

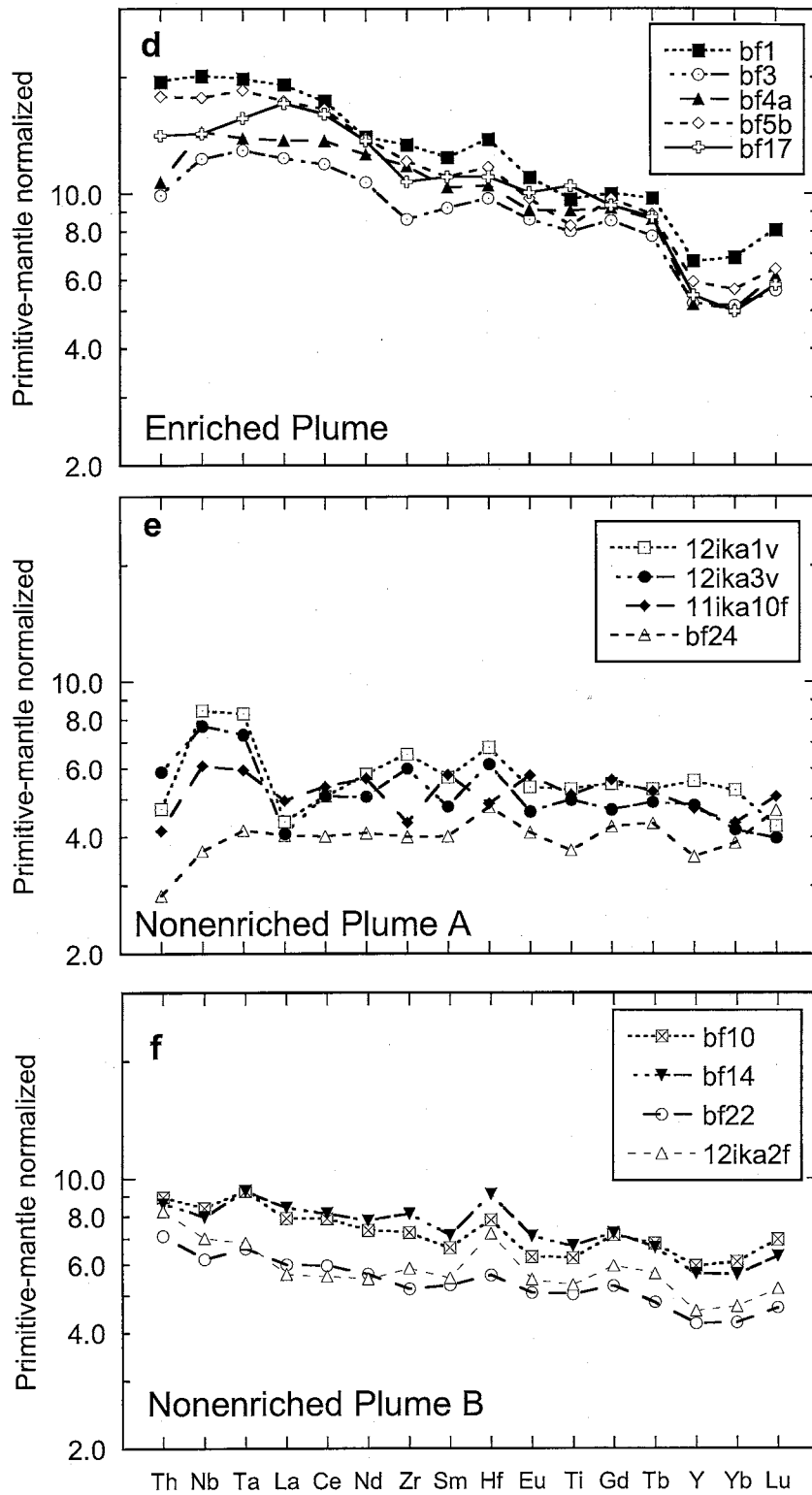


Figure 16a-f (continued) Notice the enrichment of the most incompatible elements in d and the relatively flat distribution of the nonenriched groups in e and f.

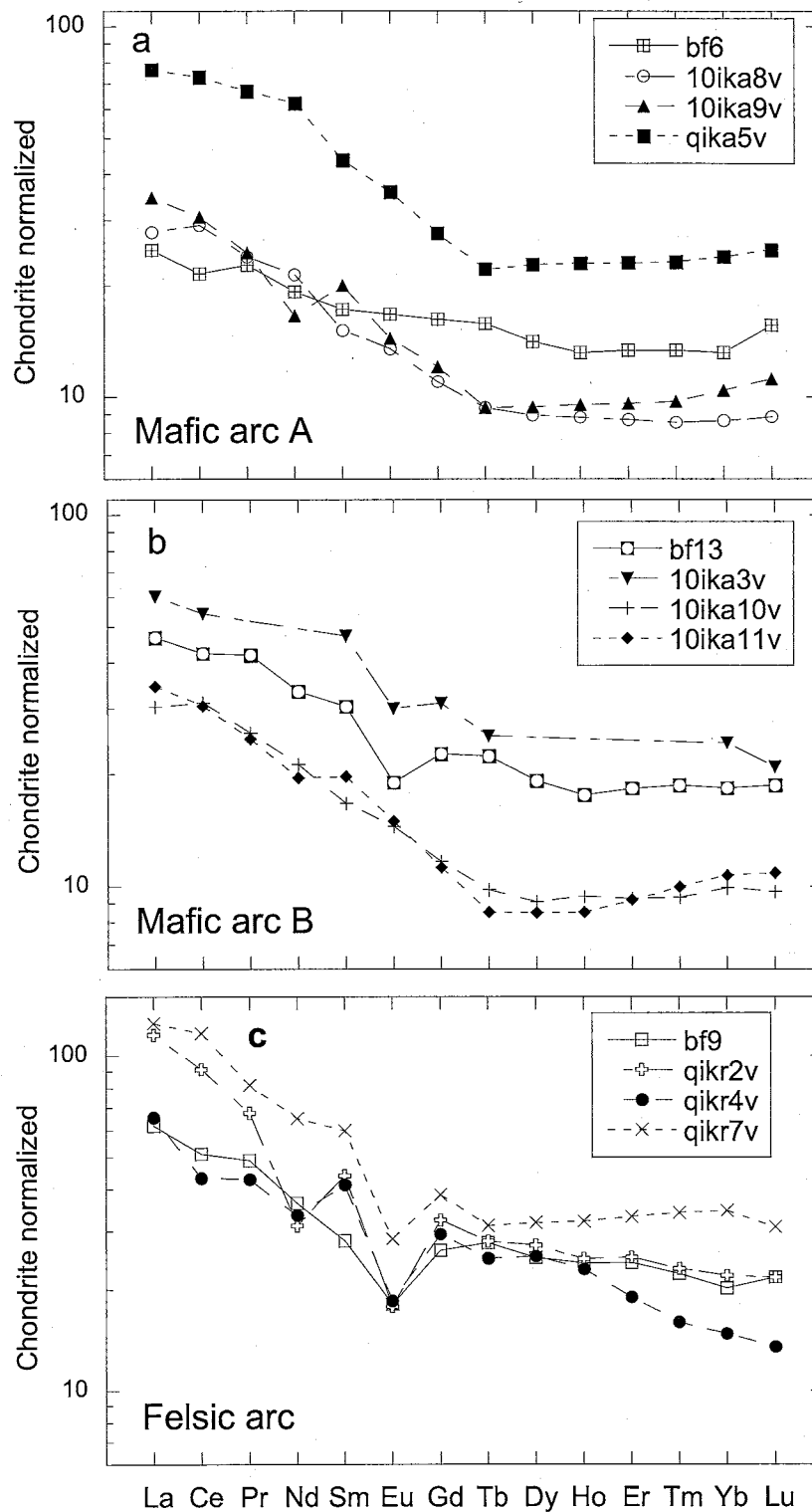


Figure 17a-f REE graphs of the Iron King Volcanics. Chondrite values for normalization from Haskin et al. (1968). Notice the considerable enrichment from middle REE to light REE and the irregular patterns in a-c.

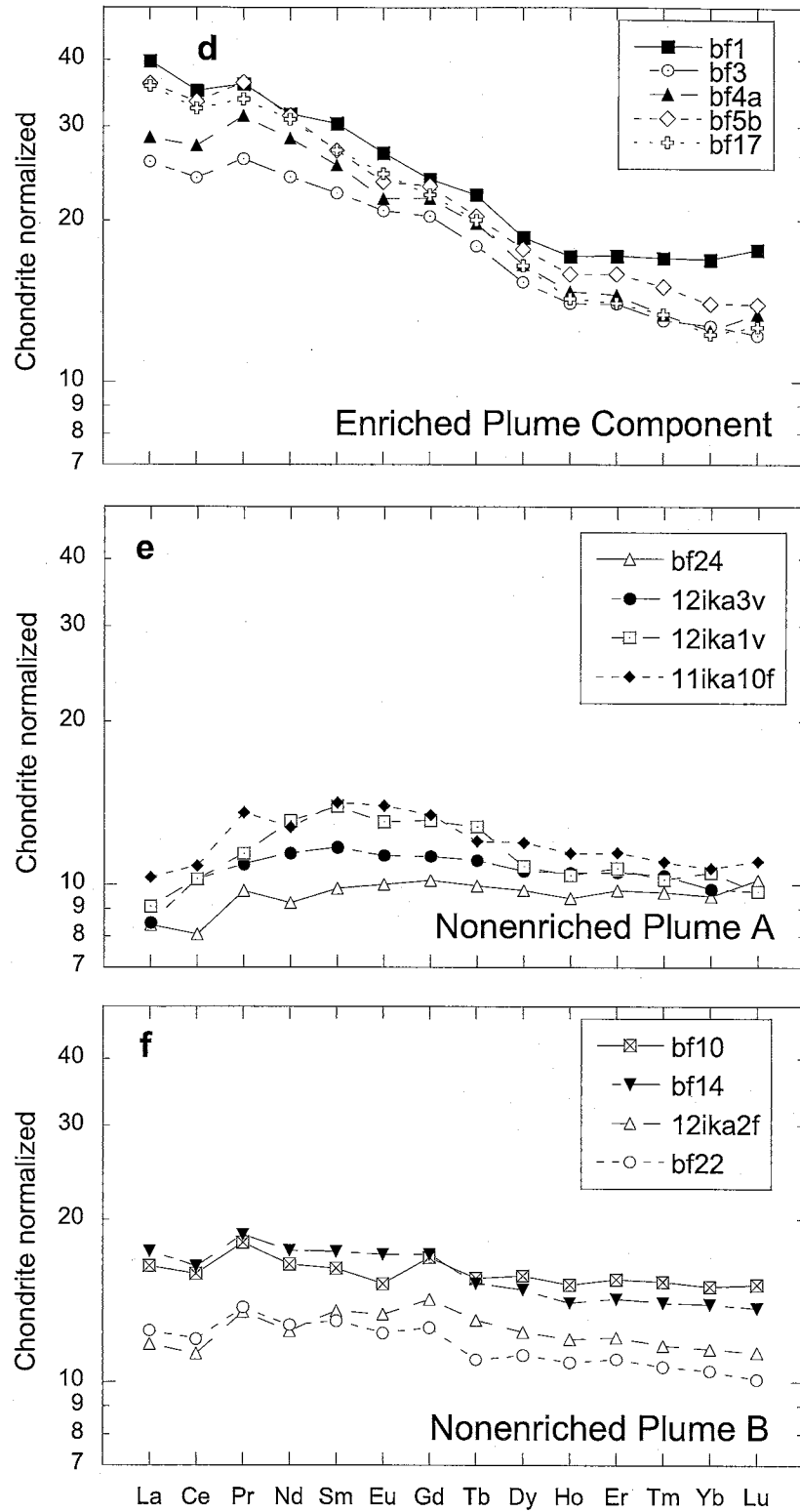


Figure 17a-f (continued) Notice the enrichment in the light REE in d and the relatively flat pattern of e and f.

1983). While most incompatible elements are mobilized in subduction settings, Ta and Nb are not. Besides the Nb-Ta depletion, the Iron King arc samples are consistently enriched in the most incompatible elements. They also show enrichment from the middle REE to the light REE and have a relatively flat distribution of heavy REE (Fig. 17a-c).

Many of the arc samples (bf6, 10ika9v, qika5v, bf13, 10ik10v, bf9 and qika2) show enrichment in Hf on the incompatible element graphs (Fig. 16a-c). The Hf enrichment in the mafic arc rocks is likely inherited from the mantle source. In the case of the felsic samples, this may be caused by zircon accumulating in the magma and remaining in the magma as it erupted. Evidence for this is seen in the thin section of sample, bf9, where zircon is present as an accessory mineral (Appendix A). Notably, sample bf9 has the most significant Hf anomaly and is one of only two samples (the other is 10ika3v) that has a positive Zr anomaly. Felsic sample qika7v is not enriched in Hf and is depleted in Zr (Fig. 16c). Terbium appears to be enriched in bf6, but this is likely an analytical artifact rather than an anomaly in the source magma (Fig. 16a).

A notable anomaly among several samples (bf13, bf9, qika2 and qika4) on the REE diagrams (Fig. 17a-c) includes the depletion in Eu relative to Sm and Gd, a characteristic that probably developed by fractional crystallization of plagioclase. Although most of the arc volcanics have relatively flat HREE distributions, a few become increasingly enriched from the middle to heavy REE (10ika9v, 10ika11v) or increasingly depleted from the middle to heavy REE (qika4v).

The arc samples are divided into mafic and felsic rock types. The trace element distributions in the felsic group are very similar to the distribution of the mafic group. One notable difference is the strong negative Ti anomaly in all of the felsic volcanics

(Fig. 16c). This is likely a fractional crystallization effect of ilmenite. The mafic samples also display negative Ti anomalies (with the exception of sample bf6), but they are generally much weaker than in the felsic samples (Fig. 16a-b). The felsic group also shows a weaker depletion in Nb and Ta than the mafic group (Fig. 16c), but their enrichment from the middle to light REE is greater (Fig. 17c).

Plume-derived basalts

Besides the missing Nb-Ta anomaly, the most striking feature of the Iron King plume component is the development of two unique trace element distributions in both the PMn diagrams and the REE diagram. Most of the samples have relatively flat incompatible and REE distributions (Fig. 16e-f, Fig. 17e-f), but several are enriched in the most incompatible elements and the light REE (Fig. 16d, Fig. 17d). For this reason, the plume-derived basalts are broken into two groups: the enriched group and the nonenriched group. All of the plume-derived rocks are also enriched in Lu relative to Yb on the PMn diagram, but this is probably an analytical artifact.

Two other incompatible element anomalies are characteristic of all enriched plume samples: enrichment in Hf and depletion in Y and Yb, those incompatible elements most strongly controlled by garnet (Fig. 16d). In addition, samples bf3 and bf4a are depleted in Th, while bf3 and bf17 show depletion in Zr. Ti is slightly depleted in bf5b, but it is enriched in bf17. The enriched group also has several REE characteristics common to all samples (Fig. 17d). They are slightly depleted in Ce, and they show no fractionation between Ho to Er. In no other pair of elements is this true for all samples. One sample (bf1) continues this flat pattern through the heavy REE, while the other

enriched samples are depleted in the heavy REE relative to Ho and Er. In terms of incompatible and REE distributions in the various submarine tectonic settings, the overall element distributions in the Iron King enriched group is most similar to ocean island basalts and some oceanic plateau basalts.

Rocks of the nonenriched group (Fig. 16e-f, Fig. 17e-f) show consistently flat incompatible and REE distributions. All show a slight enrichment of Hf relative to Zr. Furthermore, the nonenriched group has much lower overall incompatible element concentrations than the enriched group, with an average of about 6 x chondrites for the nonenriched group and an average of about 10 x chondrites for the enriched group.

A third subdivision among the Iron King Volcanics can be made based on the behavior of the incompatible elements Th, Nb, Ta and La within the nonenriched group. In the nonenriched subgroup A (Fig. 16e), Th and La are notably depleted and Nb and Ta are enriched (except for sample bf24). The overall pattern of subgroup A is flat; however, considerable variation occurs among the mid-range incompatible elements. Zr and Hf are enriched in 12ika1v and 12ika3v, but depleted in 11ika10f. Sm is enriched in 11ika10f, but depleted in 12ika1v and 12ika3v. Sample 11ika10f is enriched in Eu and depleted in Yb. In the case of the nonenriched subgroup B (Fig. 16f), there is a very slight enrichment from the least incompatible elements to the most incompatible elements. All samples in subgroup B show a weak negative anomaly in Nb, Y and Yb and weak to strong Hf enrichment. One sample (bf24) has no clear affiliation with either subgroup. It has a strong negative Th anomaly like the samples in subgroup A, but the rest of its incompatible element distributions appear very similar to subgroup B.

The REE distributions of the nonenriched rocks support the division of these rocks into subgroups (Fig. 17e-f). The nonenriched subgroup A is highly depleted in the light REE, increases in enrichment in the middle REE, but gradually becomes more depleted in the heavy REE. The nonenriched subgroup B shows a slight depletion in Ce, a slight enrichment in Pr, and an otherwise flat distribution in the light REE from La to Gd. From Tb to Lu, the REE distribution flattens out. Overall, few REE show anomalous behavior in any one sample, but 11ika10f is enriched in Pr. As with the incompatible element distributions, bf24 has transitional REE distributions between the subgroups. It is depleted in Ce and enriched in Pr like the nonenriched subgroup B, but the REE distribution of bf24 is slightly enriched in the middle REE as are the subgroup A samples.

DISCUSSION

Introduction

Tectonic studies have attempted to establish the importance of oceanic plateaus as building blocks of the continents. The foremost purpose of this study is to show, using lithologic relationships and geochemistry, that the Iron King Volcanics originated as part of an oceanic plateau. A second goal is to provide information about the source of the mantle plume that produced this plateau. To achieve either of these objectives, we must first show that secondary processes such as weathering, hydrothermal, metamorphic or deformational processes have not significantly altered the geochemical signature of the basalts.

Effects of alteration

Elements in volcanic rocks have variable mobility if the rocks undergo alteration. CIPW norms of the Iron King Volcanics show that major elements such as silica are susceptible to alteration (Table 3). In the Results section, the samples categorized as plume-derived are tholeiites (Fig. 12 and 13). Therefore, they should be silica-saturated or slightly undersaturated in terms of their CIPW norms (Winter, 2001). Instead, weighted norms of diopside, hypersthene, olivine and quartz in the Iron King Volcanics show the plume population to be undersaturated, with the exception of sample bf17. Nearly all of the arc-related samples are oversaturated in silica. This is expected since all of these rocks are basaltic andesites or felsic volcanics. It is probable that silica variation among the plume samples is caused at least in part by the mobility of major elements during alteration. The presence of nepheline and carbonate in the norms of several

Table 3 CIPW weighted norms for Iron King Volcanics.

Sample:	Enriched Plume					Nonenriched Plume, Group A					Nonenriched Plume, Group B				
	bf1	bf3	bf4a	bf5b	bf17	bf24	12ika1v	12ika3v	11ika10f	bf10	bf14	bf22	12ika2f		
Q	0	0	0	0	0	3.2	0	0	0	0	0	0	0		
or	7.2	1.1	1.2	1.4	3.1	1.0	0.47	2.5	1.1	1.2	1.8	1.0	1.3		
ab	23.9	24.4	28.4	21.8	15.8	17.0	41.5	29.1	12.6	27.0	23.6	23.2	27.7		
an	26.5	17.7	20.1	23.8	20.1	29.5	17.5	24.6	35.9	21.4	28.3	26.1	23.3		
ne	0	4.8	0	0	0	0	3.4	0	0	0	0	0	1.8		
di	11.7	25.6	22.6	22.6	0.0	25.3	10.7	15.7	23.0	18.5	10.4	19.7	22.0		
C	0	0	0	0	4.5	0	0	0	0	0	0	0	0		
hy	12.1	0	3.4	22.8	39.3	13.4	0	12.0	12.3	12.7	19.6	8.7	0		
ol	10.7	16.9	17.0	0.59	0	9.1	21.3	10.5	9.2	12.4	8.5	13.7	18.6		
ac	0	0	0	0	2.3	0	0	0	0	0	0	0	0		
mt	2.1	1.9	2.0	2.1	0	1.8	1.9	1.8	2.0	2.2	1.9	1.9	2.0		
il	4.1	3.3	3.8	3.5	4.4	1.5	2.2	2.1	2.1	2.6	2.8	2.1	2.2		
ap	0.51	0.44	0.46	0.46	0.49	0.14	0.23	0.21	0.23	0.32	0.28	0.23	0.23		
c	0	0	0	0	0	0	0	0	0	0	0	0	0		
Total	98.7	96.2	98.9	99.1	93.3	98.6	99.1	98.5	98.6	98.2	97.3	96.7	99.1		
	undersaturated				over	undersaturated				undersaturated					

Sample:	Mafic Arc					Felsic Arc						
	bf6	bf13	10ika3v	10ika8v	10ika9v	10ika10v	10ika11v	qika5v	bf9	qjkr2v	qjkr4v	qjkr7v
Q	0	8.4	5.8	0	10.7	13.2	12.3	6.4	49.7	49.7	80.6	73.4
or	1.1	16.0	1.4	0.47	5.0	1.6	1.7	11.2	39.5	39.5	11.2	6.3
ab	28.1	17.8	27.3	38.8	28.0	17.1	18.3	28.9	1.0	1.0	1.6	0.25
an	23.4	17.7	20.4	27.1	24.4	34.8	35.3	22.8	0.50	0.50	0.15	0.15
ne	0	0	0	0	0	0	0	0	0	0	0	0
di	19.6	17.2	11.8	5.1	0.50	6.8	4.3	10.2	0	0	0	0
C	0	0	0	0	0	0	0	0	5.1	5.1	4.6	6.1
hy	14.2	13.7	22.3	18.9	23.2	19.7	21.4	10.8	2.4	2.4	0.60	11.1
ol	8.5	0	0	1.5	0	0	0	0	0	0	0	0
ac	0	0	0	0	0	0	0	0	0	0	0	0
mt	1.8	1.5	2.3	1.5	1.4	1.5	1.5	1.3	0.16	0.16	0	0.39
il	2.0	1.9	4.6	1.4	1.4	1.4	1.4	3.5	0.30	0.30	0.25	0.21
ap	0.25	0.42	2.3	0.32	0.32	0.32	0.32	1.1	0	0	0	0.07
c	0	0	0	0	0	0	0	0	0	0	0	0
Total	98.9	94.5	98.1	95.0	95.0	96.4	96.5	96.3	98.6	98.6	99.0	98.0
	under	oversaturated		undersaturated		oversaturated			oversaturated			

samples (bf3, bf17, 12ika1v, 12ika2f, bf9, qikr2v, qikr4v, qikr7v) provides added support that these samples have undergone alteration. The carbonate was most likely introduced during formation in amygdules as seen in outcrop. An examination of thin sections supports later introduction of carbonate, because calcite fills in the spaces between other grains (Appendix B).

Loss on ignition (LOI) is the mass lost when a powdered sample is heated to 800°C where structural volatiles, such as water and carbon dioxide, are released (Winter, 2001). Alteration can increase the LOI in volcanic rocks by adding phases that lose mass when heated to 800°C, such as clay minerals, zeolites or carbonates. Several combinations of elements have been plotted against LOI to illustrate the effects of alteration in the Iron King Volcanics. The LOI versus MgO graph shows no overall trend (Fig. 18). Instead the arc and plume volcanics define two groups. The plume basalts are clustered between 6 and 9 wt% MgO without a clear trend. The arc volcanics, on the other hand, display a positive trend from 0 to 4 wt% MgO. The felsic samples appear to have undergone the least amount of alteration of the arc samples. As to overall alteration, the nonenriched plume group has the lowest average LOI. The enriched samples have the greatest variation in LOI relative to the other groups, with bf17 showing the highest volatile content. The mafic arc samples also show variation, but have a higher average LOI than the plume samples. Unlike the LOI-MgO graph, the LOI versus SiO₂ graph (Fig. 19) shows a positive trend among the mafic arc samples, demonstrating that these samples increase in SiO₂ with alteration, while the plume samples have an apparent negative trend showing decreasing silica content with increasing LOI.

The graph of LOI versus CaO/Al₂O₃ demonstrates a considerable difference

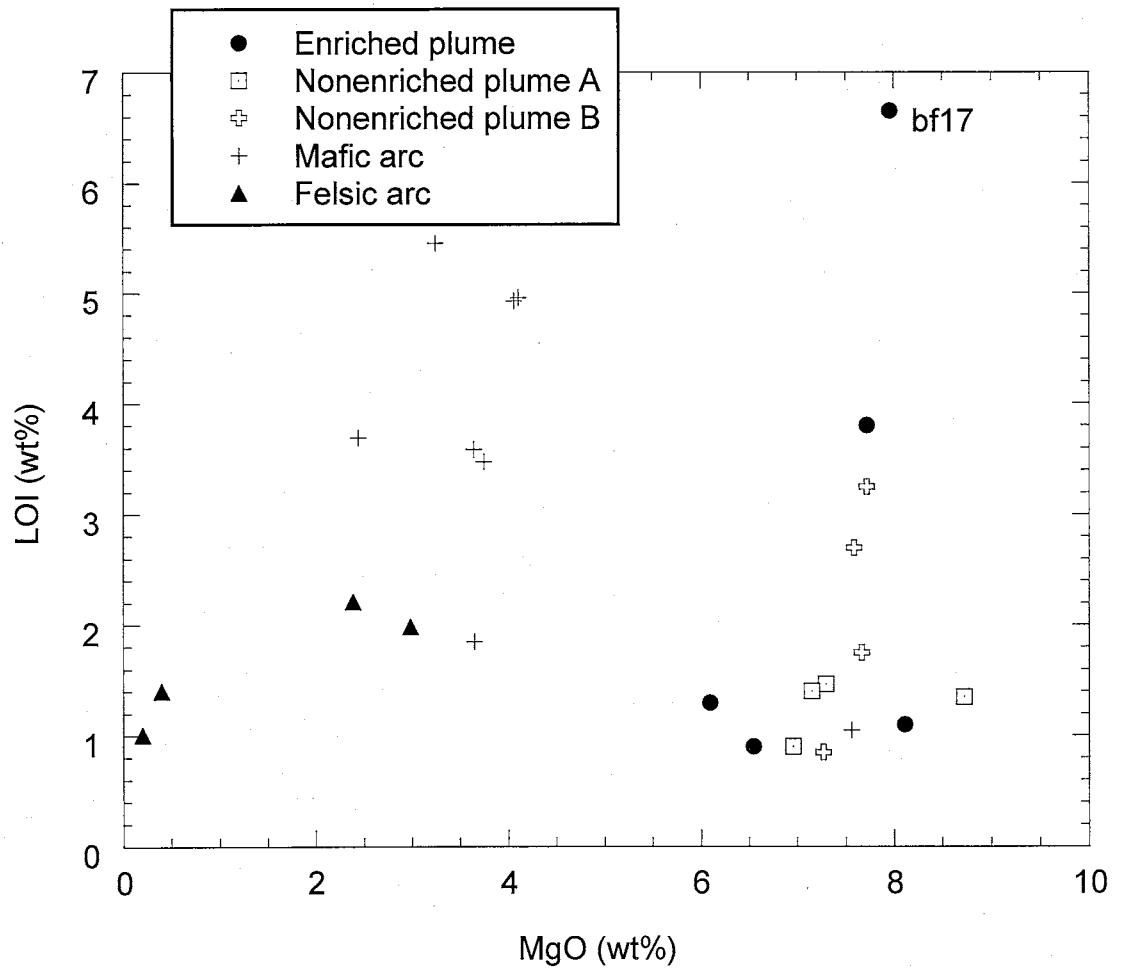


Figure 18 Graph of loss on ignition (LOI) vs. MgO for the Iron King Volcanics.

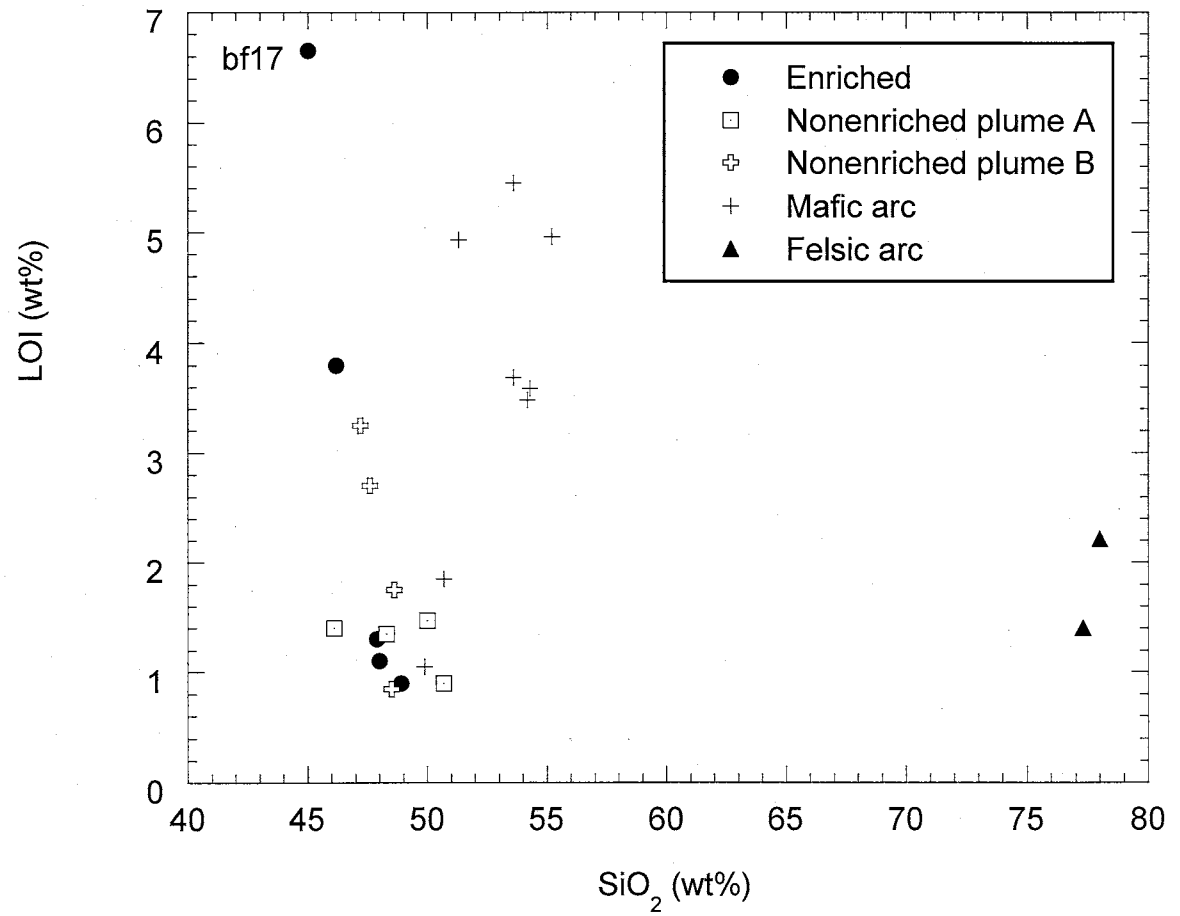


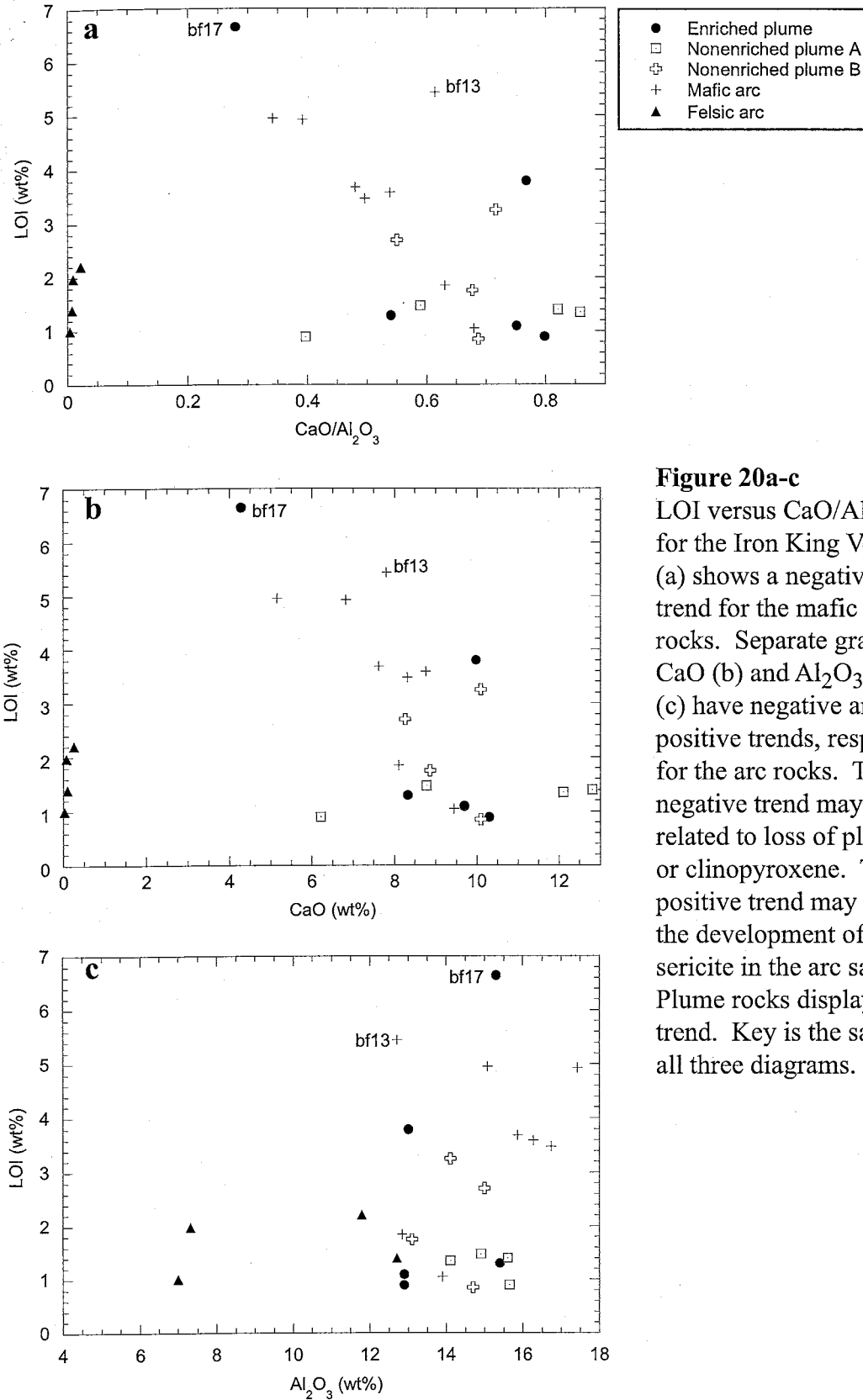
Figure 19 Iron King Volcanics plotted on graph of LOI against SiO₂.

between the arc and plume volcanics (Fig. 20a). The mafic arc rocks show a negative trend (with the exception of sample bf13) and the plume subgroups display no trend. The felsic arc volcanics have insignificant concentrations of CaO and therefore plot near zero in Figure 20a and b. With the exception of bf13, the plot of LOI against CaO has a negative trend, and LOI versus Al_2O_3 results in a weak positive trend. The decreasing CaO with increasing LOI may be caused by the loss during alteration of primary minerals such as clinopyroxene and plagioclase. The increase in Al_2O_3 with LOI may be related to an increase in secondary minerals such as clay and sericite in the arc samples. This is likely the reason for the high amount of Al_2O_3 in the felsic rocks, an explanation supported by a considerable amount of sericite in sample bf9 (Appendix A). However, bf13 defies this explanation with a lower than average Al_2O_3 concentration and a considerable amount of sericite found in thin section.

LOI is also plotted against several trace element ratios. All three groups of mantle plume rocks show no correlation with LOI. An example is the plot of LOI versus Th/Ta (Fig. 21). Although the enriched plume sample bf17 has the highest LOI, its trace element values consistently plot close to primitive mantle values, shown by a vertical line, as is true with other plume basalts with greater than average LOI values. Arc-related samples show similar tendencies. LOI is plotted against the other incompatible element ratios and element concentrations in Appendix C, and no correlations exist with LOI.

Tectonic discrimination

The discussion of the tectonic settings of the Iron King Volcanics emphasizes

**Figure 20a-c**

LOI versus CaO/Al₂O₃ plot for the Iron King Volcanics (a) shows a negative trend for the mafic arc rocks. Separate graphs of CaO (b) and Al₂O₃ (c) have negative and positive trends, respectively, for the arc rocks. The negative trend may be related to loss of plagioclase or clinopyroxene. The positive trend may relate to the development of clay and sericite in the arc samples. Plume rocks display no trend. Key is the same for all three diagrams.

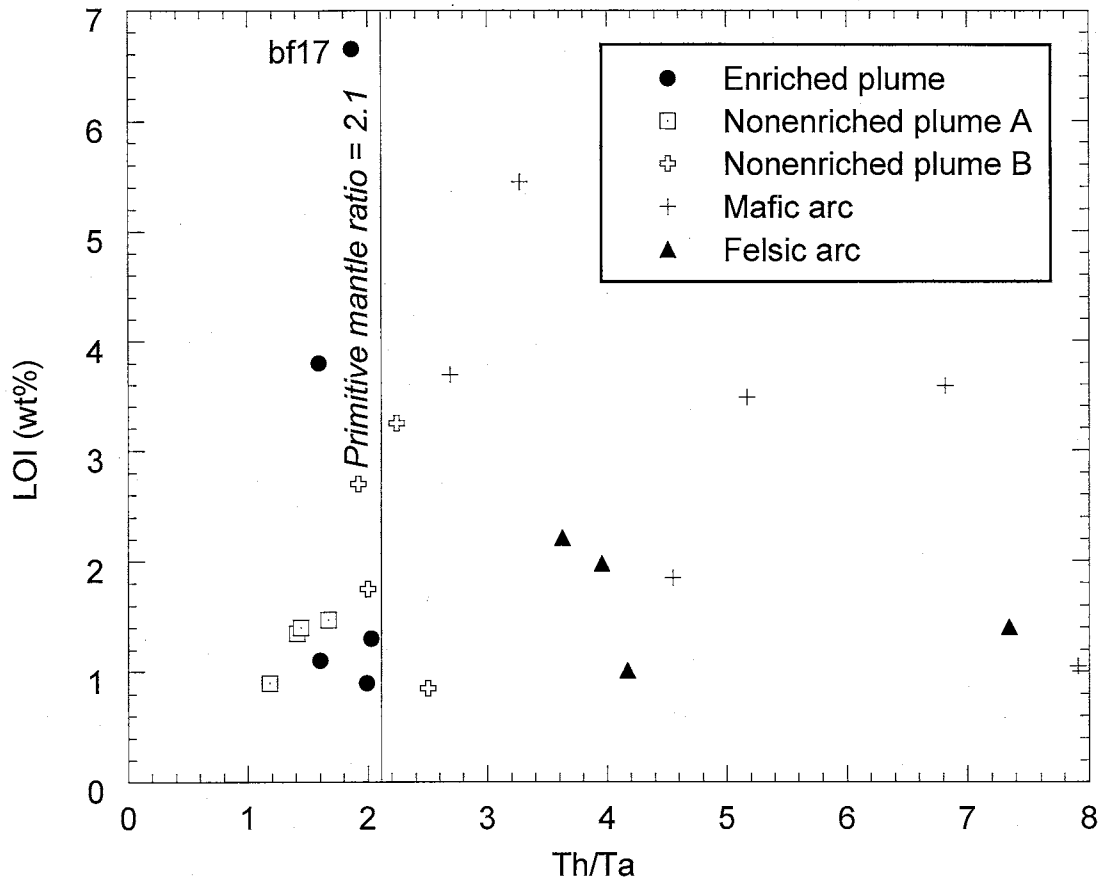


Figure 21 LOI vs. Th/Ta for the Iron King Volcanics. The ratio of Th/Ta does not correlate with alteration and metamorphism. Primitive mantle values from Sun and McDonough (1989).

incompatible trace element distributions and lithologic associations. It has already been suggested (Results section) that the Iron King incompatible element and REE distributions (Fig. 16a-f and Fig. 17a-f) reflect more than one tectonic setting.

Lithologic association

The presence of pillow basalts, hyaloclastic and amygdaloidal textures, and chert from hydrothermal venting in the Iron King Volcanics suggests an oceanic origin for the volcanic sequence with eruptive depths greater than 1100 m. These deep eruptive depths are based on the results of a study by Staudigel and Schmincke (1984) of the La Palma seamount, Canary Islands. The transition from dominantly pillow basalts to dominantly hyaloclastites indicates a decreasing depth of eruption (Batiza and White, 2000), as do decreasing pillow sizes. Staudigel and Schmincke (1984) developed a four-stage model to show this relationship. The deep-water stage (1800-1140 m) is dominated by pillow basalts (5-15% volcanoclastic material; Fisher and Schmincke, 1984), and explosive deposits dominate the three shallower stages. Within the Iron King Volcanics, there appears to be a decrease in pillow size and increase in the proportion of volcanoclastic rocks from west to east in the southern region, suggesting that the eastern volcanics were the product of shallower eruptions than volcanics in the west. Furthermore, the eruption depth of the Iron King Volcanics must have been shallow enough to allow vesiculation. The Iron King Volcanics is not dominated by volcanoclastic material in any location, an observation that supports deep-water eruption.

In general, submarine eruption does not favor a continental origin for the Iron King, such as continental flood basalts and continental rifts. The distribution of rock

types in the Iron King Volcanics provides added support for an oceanic origin. Felsic volcanics are abundant in the northern section of the Iron King Volcanics, whereas basalt flows that carry plume geochemical signatures dominate the lithologic types in the southern section (Fig. 11). Mafic samples that carry arc geochemical signatures are also found in the north. With the help of this evidence, an interpretive map of the Iron King Volcanics has been constructed that shows an approximate boundary between the arc and plume components (Fig. 22) using the locations of samples from each component. An attempt was made to determine the boundary between the enriched and nonenriched plume groups, however, the distribution of the samples from each group is so complex that no separate geographical regions could be distinguished. The complex distributions are caused by the multiple folds and minor shear zones within the Iron King Volcanics that were not included on maps of the area. Furthermore, if the arc sequence developed on top of the oceanic plateau, interfingering of arc and plume volcanics should have developed at depth. For these reasons, no boundary between plume groups was proposed, and the boundary drawn between the arc and plume components is very generalized. Nevertheless, Figure 22 is useful to show some lithologic and geochemical division between these components. Note that unlike continental volcanic sequences, the plume component of the Iron King Volcanics are dominated by basalt flows and the arc component does not have a bimodal distribution of felsic and mafic lavas but grades from felsic through intermediate to mafic lavas (Fig. 11 and 12).

Besides island arc basalts, oceanic tectonic settings include mid-ocean ridges, ocean islands and oceanic plateaus. It is unlikely that the Iron King plume component represents a mid-ocean ridge (ophiolite) sequence for two reasons: (1) There are no

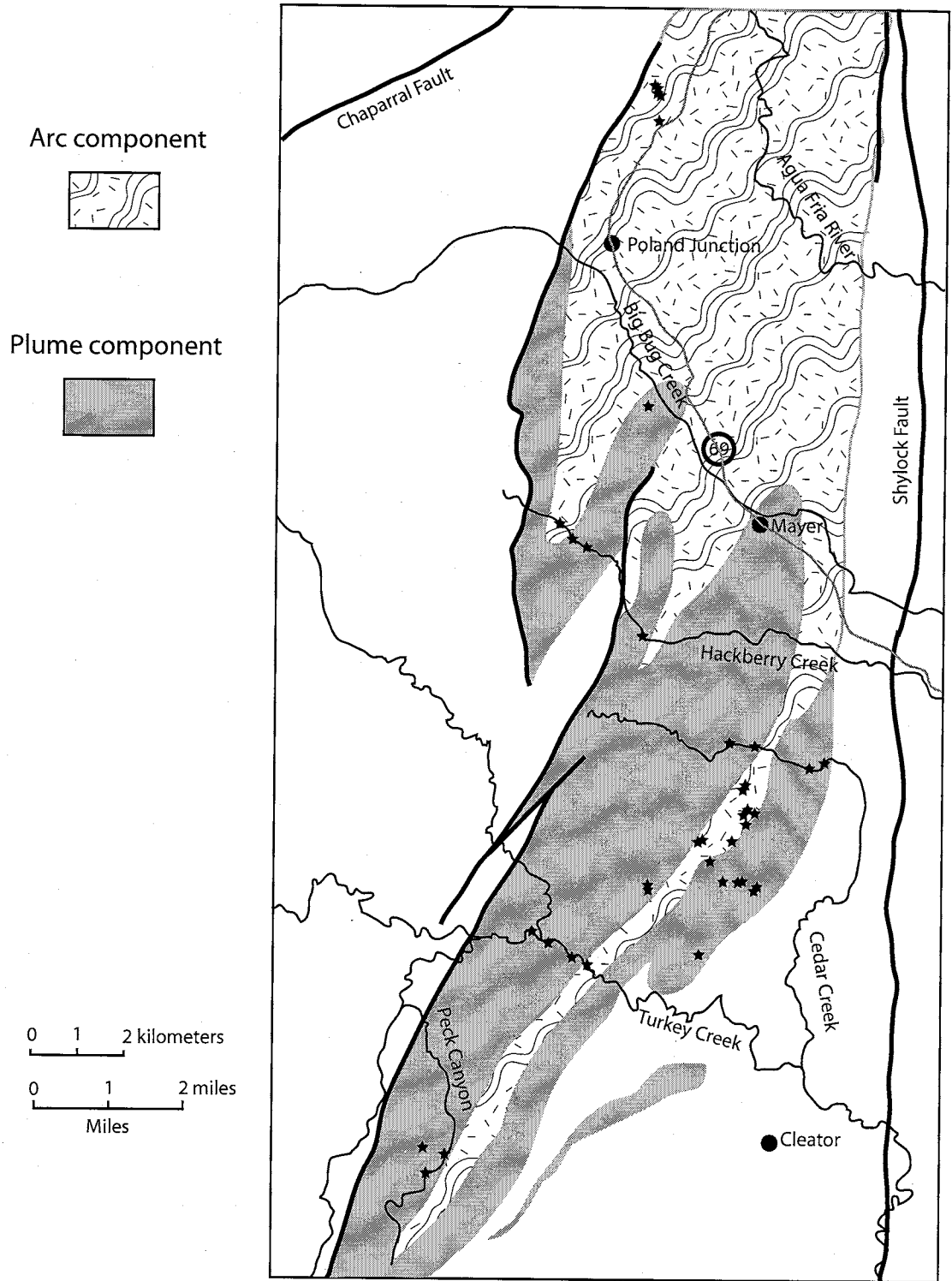


Fig. 22 Interpretive map of the distribution of arc and oceanic plateau assemblages within the Iron King Volcanics (base map from Anderson and Blacet [1972a and b]).

sheeted dikes present in the Iron King Volcanics, and (2) the occurrence of hyaloclastites in mid-ocean ridge sequences is rare (Batiza and White, 2000), whereas they have a significant presence in the Iron King Volcanics. The similarity of origin of ocean islands and oceanic plateaus make lithologic discrimination between the two difficult. The fragmented and deformed nature of the Iron King Volcanics prevents recognition of the large-scale features of the original volcanics. If seamounts or aseismic ridges were present, they are unrecognizable. In this case, magma type is a stronger tool for distinguishing between the two tectonic settings. Ocean island magmas undergo more differentiation, resulting in a greater proportion of intermediate to felsic compositions than found in oceanic plateaus. As seen on rock classification schemes (Fig. 12 and 13), rock types in the Iron King Volcanics range from tholeiite to rhyolite, but the southern plume section is dominated by basalts.

Lithologic assemblages in the southern assemblage of the Iron King Volcanics, suggest formation as part of an oceanic plateau. No ultramafic or gabbroic rocks occur in this assemblage, however, as is typical of an idealized oceanic plateau sequence (Kerr et al., 1998). Because the upper parts of oceanic plateaus may be obducted (Kerr et al., 1998), it is possible that the Iron King pillow basalts represent an upper sequence that has been sheared from the roots of the plateau during accretion.

Geochemical evidence

Several trace element diagrams have been constructed to indicate the tectonic origin of the Iron King Volcanics. As with rock classification graphs, the Th/Ta vs. La/Yb graph utilizes immobile elements with known ratios in basalt sources (Fig. 23).

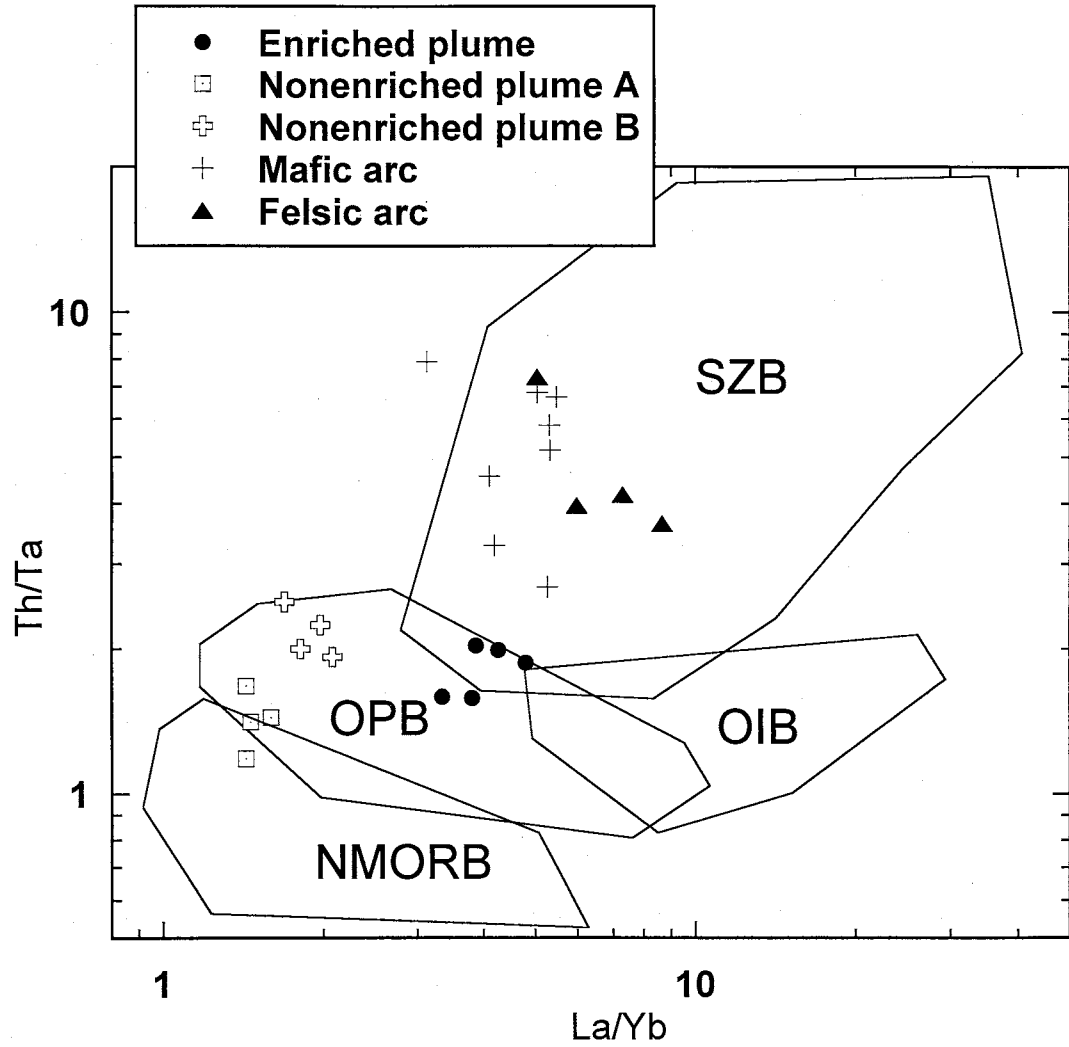


Fig. 23 Th/Ta vs. La/Yb graph showing fields for N-MORB, oceanic plateau basalts (OPB), oceanic island basalts (OIB), and island arc basalts (SZB). The Iron King plume basalts fall mostly within the oceanic plateau field and define two populations: enriched and depleted. Fields from Tomlinson and Condie (2001).

Included on the graph are fields by Tomlinson and Condie (2001) for MORB, subduction zone basalts (SZB), OIB and OPB. The Iron King enriched group has a greater La/Yb ratio than the nonenriched subgroups, while the mafic and felsic arc groups have a greater Th/Ta ratio than either of the two plume groups. The plume-related samples fall within the OPB field, and the arc-related samples fall within the SZB field. However, not all of the Iron King samples fall clearly into one field. For example, members of nonenriched subgroup A fall near or in the N-MORB field. The enriched plume samples fall within or near the subduction zone field as well as the oceanic plateau field.

Fitton et al. (1997) found that a graph of Nb/Y vs. Zr/Y helps distinguish between plume and MORB (Fig. 24). This graph takes advantage of the fact that N-MORB is more depleted in Nb than other incompatible elements and that the lower mantle that produces mantle plumes is enriched in Nb relative to the upper mantle that produces MORB (Fitton et al., 1997). Fitton et al. (1997) attribute this to the behavior of Nb in subduction zones. Niobium is not mobilized at subduction zones and as a result is carried by the subducting slabs into the mantle where it is recycled through the mantle, possibly reappearing in mantle plumes. On the graph of Nb/Y and Zr/Y, Iceland basalts and MORB cluster in a parallel fashion on each side of a boundary determined by the formula

$$\log (\text{Nb}/\text{Y}) = 1.92 \log (\text{Zr}/\text{Y}) - 1.740$$

(Fitton et al., 1997). The Iceland plume basalts plot above this boundary within what is called the Iceland array. MORB plots below this boundary. In the case of the Iron King Volcanics, the plume samples fall in the Iceland/plume array (with the exception of bf4a) (Fig. 24). Most of the mafic arc samples, on the other hand, fall within the MORB array, confirming a depletion of Nb in the mantle source of the arc rocks. Even the most

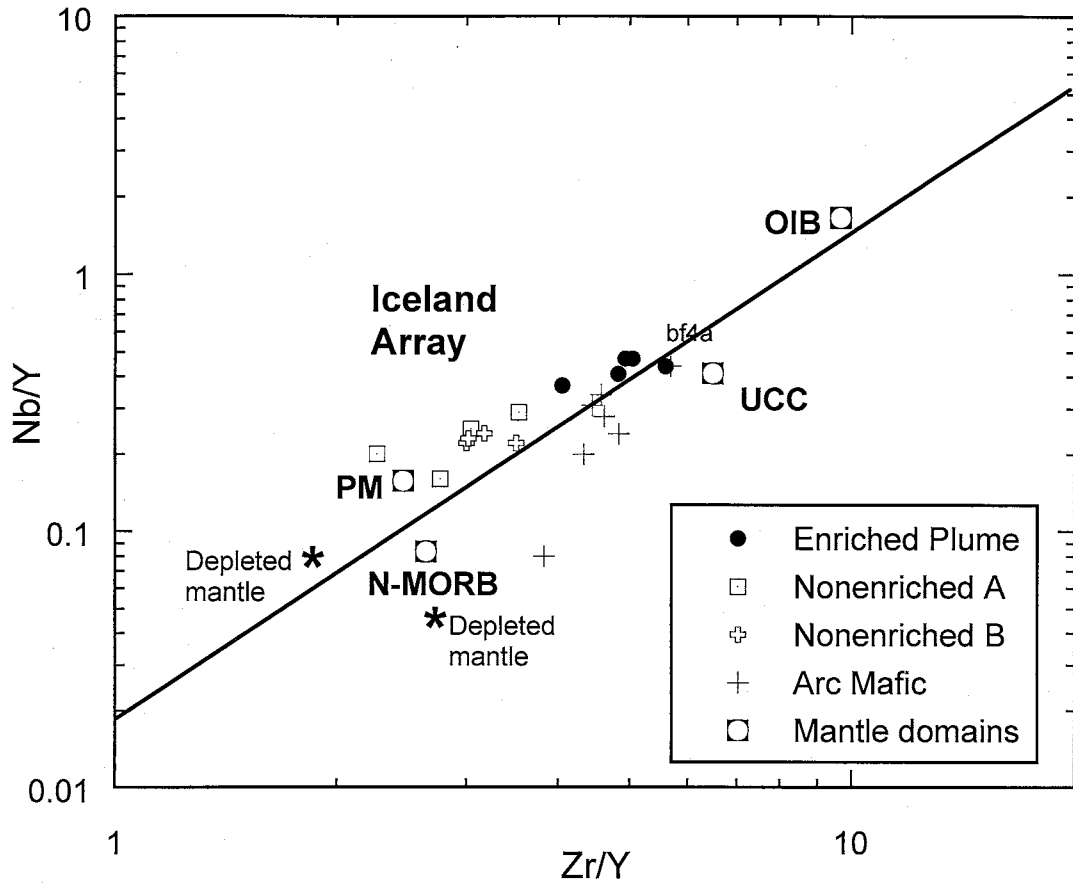


Fig. 24 Nb/Y vs. Zr/Y graph of Iron King basalts. Plume-related basalts plot above the line and mid-ocean ridge basalts plot below the line (after Fitton et al., 1997). The Nb depletion of the Iron King arc basalts cause them to plot below the line. The enriched plume samples have the lowest degree of melting. OIB, primitive mantle (PM) and NMORB are from Sun and McDonough (1989) except for upper continental crust from Condie (1993).

plot within the Iceland array. Figure 24 includes hypothetical depleted sources for both arrays. It is suggested that the closer proximity of some Iron King plume basalts to the deep depleted mantle value than to the enriched value of OIB plume basalts indicates a relatively deep depleted mantle source for these basalts. The depleted nature of the source may be a relict geochemical signature of recycling subducted material. Kerr et al. (2000) note that back-arc basins derived from a plume-derived mantle source may have geochemical signatures similar to oceanic plateaus. The incompatible element diagrams for the Iron King plume populations have no negative Nb-Ta anomalies though, and this fact is considered sufficient to show that they are not the result of the back-arc basin processes.

The Nb/Y-Zr/Y graph is useful in suggesting a plume source for the Iron King Volcanics; however, it cannot distinguish OPB from OIB, since both have plume sources. OIB is distinguished from OPB using other incompatible ratio-ratio diagrams. One example is a Sm/Yb versus Nb/Zr graph (Fig. 25). On this graph, OIB has significantly higher ratios of Sm/Yb and Nb/Zr than basalts from other oceanic tectonic settings. Like the ratio of La/Yb, the Sm/Yb ratio is controlled by garnet in the restite, which concentrates heavy REE. OIB, which has a lower degree of melting than oceanic plateaus, has much lower Yb because more garnet is left in the restite, a tendency that will be explained in greater detail in the next section. The Iron King plume basalts plot within the arc and MORB fields, well away from the OIB field.

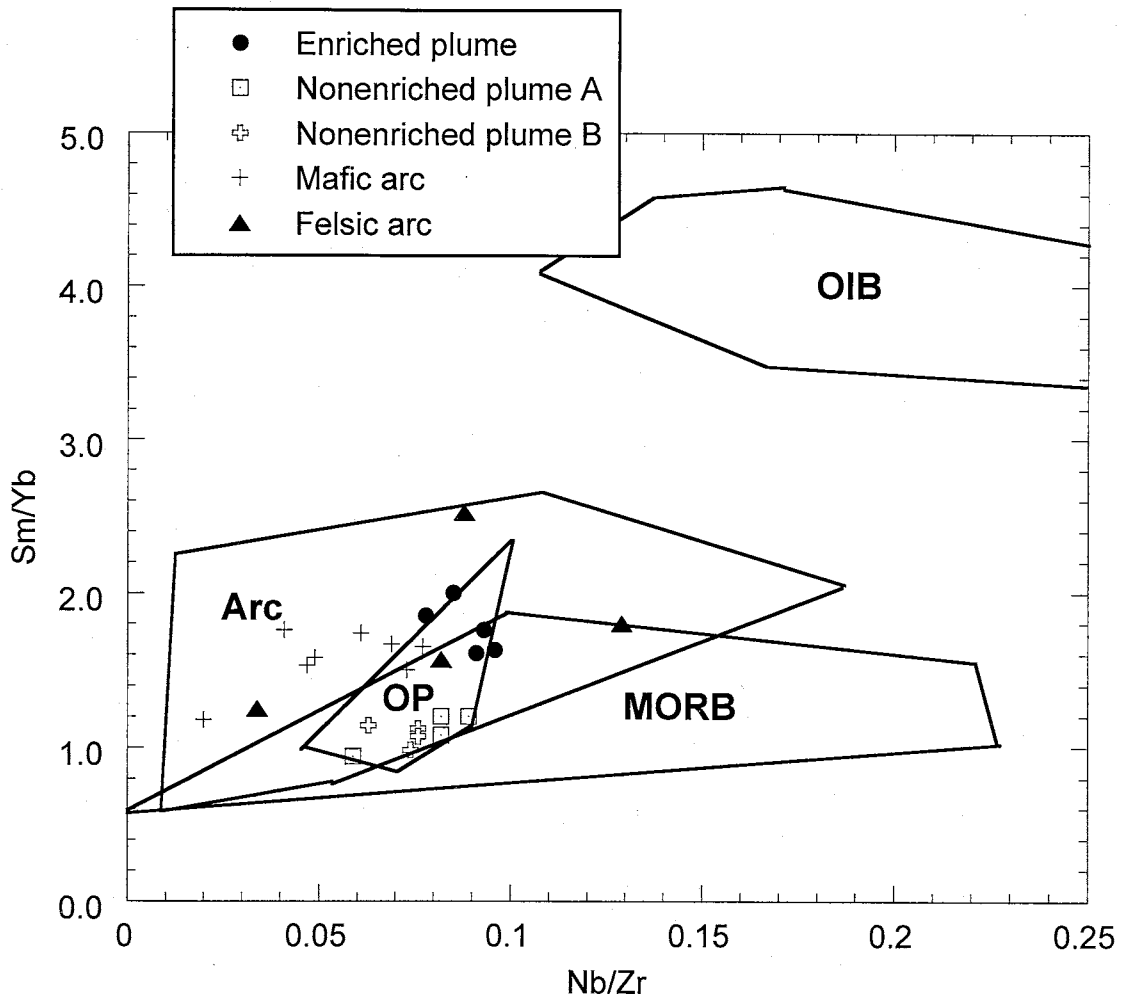


Fig. 25 Iron King Volcanics plotted on Sm/Yb vs. Nb/Zr graph. Tectonic fields generated from the following sources: arc values from Pearce (1995), Woodhead (1998), Ewart (1998), Kepezhinskias (1997), Togashi (2000) and Shinjo (2000); OIB values from Devey et al. (2000), Chaffey et al. (1989), Roden et al. (1984), Dupuy et al. (1989), Sun and McDonough (1989); MORB from Sun et al. (1979) and Tarney (1979); OP from F. Frey et al. (1991), Mahoney et al. (1993), Neal et al. (1997), Kerr et al. (1997) and Sinton et al. (1997).

Magma models

Introduction

The trace element composition of the mantle has considerable influence on the chemical composition of basaltic magmas derived from the mantle. Trace element composition can vary from depleted, like that found in shallow depleted mantle that produces MORB or deep depleted mantle that produces some Iceland plume basalts (Fitton et al., 1997), to enriched, like the mantle plume sources that produce OIB. The mineral composition of a mantle source can affect how trace elements are distributed in the melt as well. Incompatibility of an element can change depending on the mineral composition of a mantle source. Garnet is an important restite phase during melting of the mantle. Several trace elements that are normally considered incompatible, including Y and Yb, are highly compatible in garnet. Partial melting, a mantle process that occurs as a mantle plume approaches the bottom of the lithosphere, is only one process that influences magma trace element composition. Shallow processes also affect the composition of a magma. One of the main processes considered in the following discussion is fractional crystallization, which occurs in the magma chambers within the lithosphere. Crustal contamination, a second process related to the lithosphere, will be considered first.

Continental contamination

Although it is unlikely that the Iron King Volcanics, which have already been shown to originate in a submarine environment, are contaminated by continental material, it is nevertheless important to show geochemically that they are not contaminated.

Sharma (1997) used a graph of Th versus Ta (Fig. 26) to show that the two components of the Siberian Trap flood basalts, the high Ti and low Ti lavas, were contaminated by continental crust. By plotting trend lines of three basalt populations (primitive mantle, Siberian Trap high Ti basalts and Siberian Trap low Ti basalts) on the Th-Ta graph, he showed that the greater the continental contamination, the greater the slope of the line and therefore the greater the Th-Ta ratio (Fig. 26). Sharma (1997) proposed that the low Ti basalts were generated by greater degrees of melt combined with greater contamination by continental crust. Unlike the Siberian Trap basalts, which deviated strongly from the primitive mantle, the Iron King plume-derived basalts follow the primitive mantle line closely, indicating little or no continental contamination (Fig. 26). The Iron King arc component, on the other hand, shows a strong affinity to the low-Ti Siberian Trap basalts. There are two possible reasons for a high Th-Ta ratio in the arc volcanics: (1) the arc source was contaminated by continental crust, or (2) the ratio was affected by the characteristic depletion of Ta in the mantle wedge that produced the Iron King arc volcanics.

Fractional crystallization

Two models are introduced here to represent the effect of fractional crystallization on trace element distributions in the Iron King plume volcanics. A graph of Ni vs. Mg number (Fig. 27) indicates that, in general, fractional crystallization has had considerable influence on the Iron King plume basalts because most Ni values are less than 100 ppm (Condie, 2001). Furthermore, the graph shows a positive trend among the plume volcanics that follows the general fractional crystallization trend established by Clague

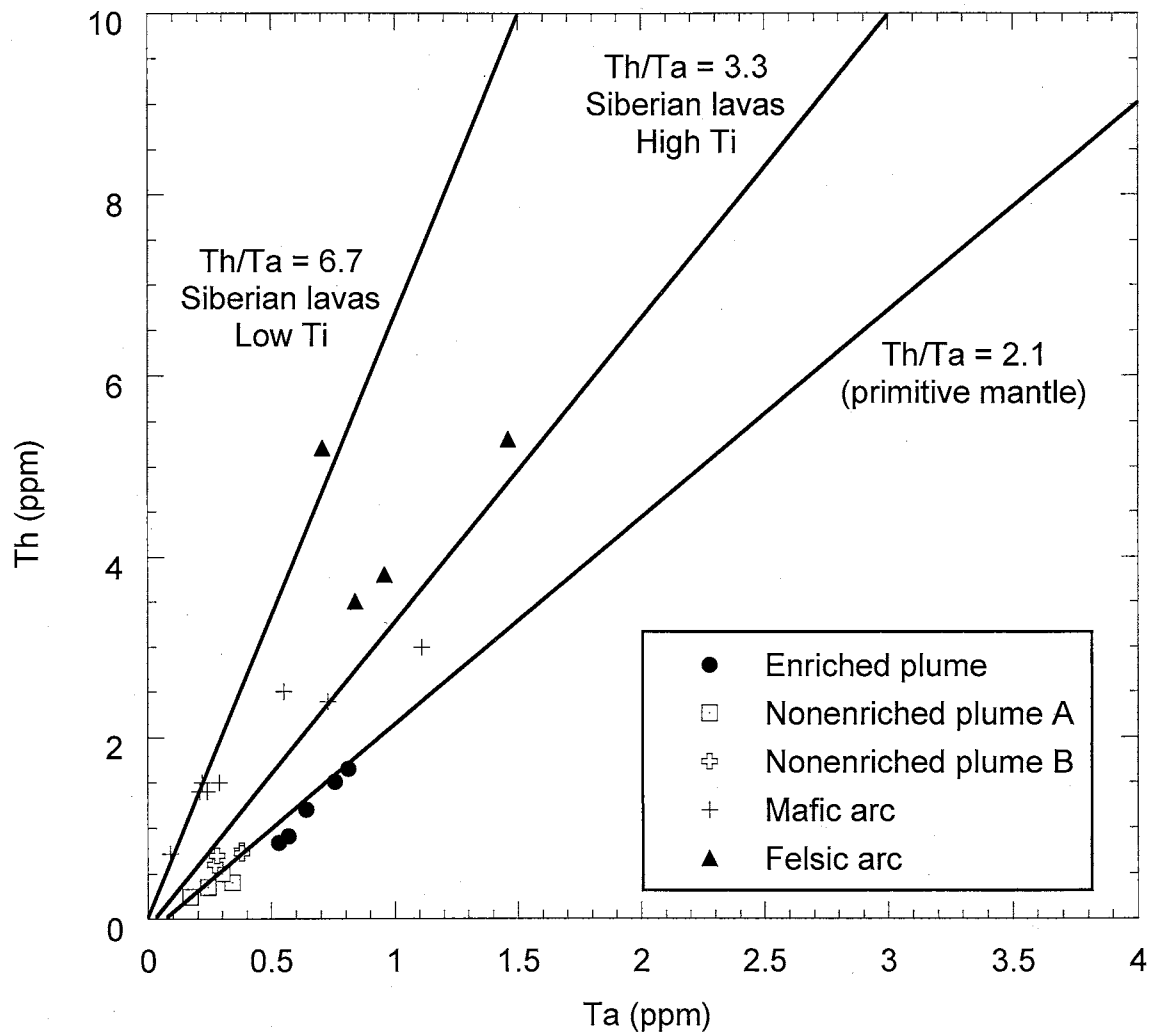


Fig. 26 Th vs. Ta graph of Iron King Volcanics. Siberian lava trends from Sharma (1997). Primitive mantle ratios from Sun and McDonough (1989).

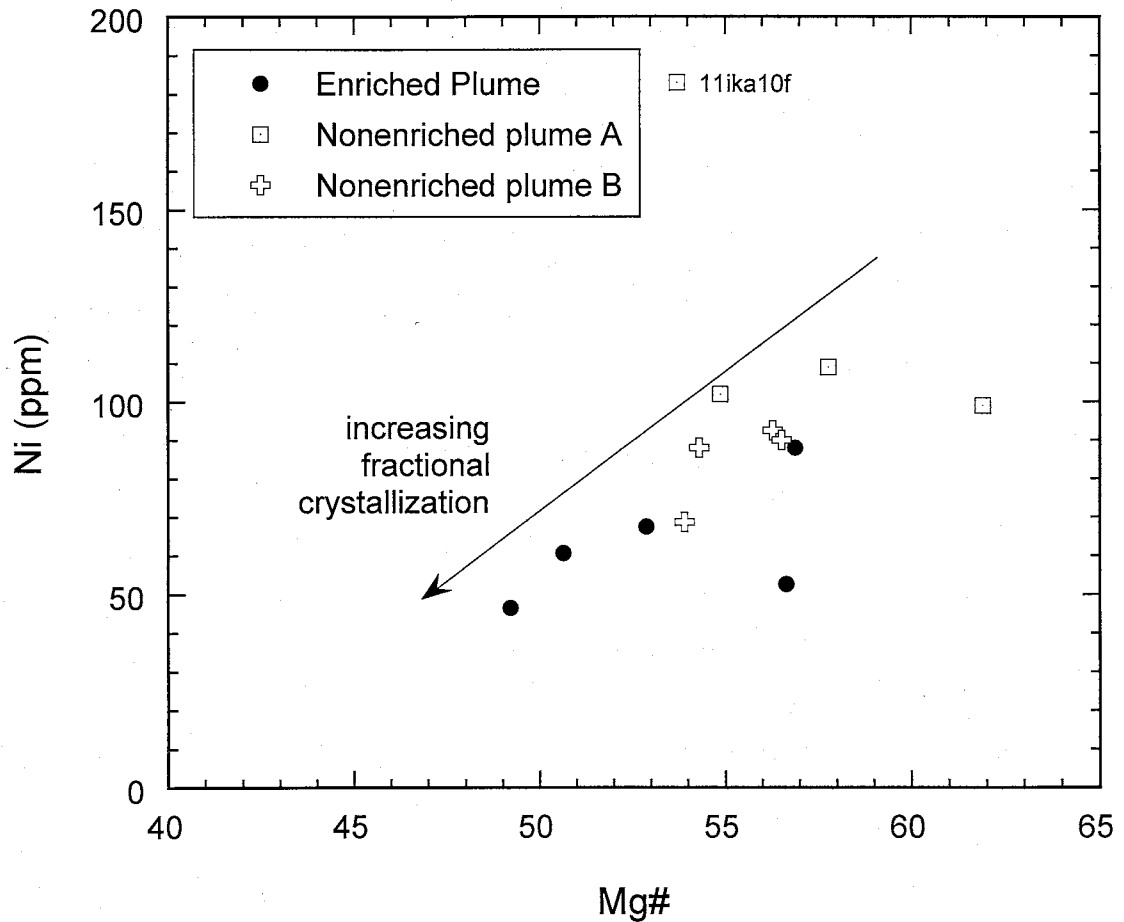


Fig. 27 Graph of Ni vs. Mg# for the plume-related members of the Iron King Volcanics. Because Ni and Mg# decrease in the melt as fractional crystallization progresses, as shown by a generalized trend line after a study by Clague and Frey (1982), the positive trend supports that Iron King mafic samples underwent fractional crystallization. (Mg# = $\text{MgO}/[\text{MgO} + \text{FeO}_T + \text{Fe}_2\text{O}_3]$ using molecular ratios.)

and Frey (1982). The enriched group has lower Ni and Mg number values, supporting that fractional crystallization has had a greater affect upon this group, because more of the mineral phases that contain Ni have been removed from the magma (ie. olivine). Nonenriched sample 11ika10f has an anomalously high concentration of Ni that may be related to accumulation of olivine from the magma chamber prior to eruption.

To test the effect of fractional crystallization on incompatible element distributions in Iron King plume magmas, the ratios of Th/Ta and La/Yb can be calculated at specific degrees of crystallization in a magma chamber and plotted on a ratio-ratio diagram. The Rayleigh equation

$$[1] \quad C_L = C_O [F^{(D-1)}]$$

(Rollinson, 1993) is used where C_O represents trace element compositions in the most primitive melt that undergoes fractional crystallization. C_L is the concentration of the resulting melt. F is the percent of melt left after a specific amount of crystallization (1-F). D is the bulk distribution coefficient.

One of the least evolved Iron King samples (bf4a) was chosen (based on its high MgO values) to represent a starting melt (C_O). Its concentrations of Th, Ta, La and Yb are used to calculate a final melt values (C_L) for these elements. C_L is calculated at five different percents of crystallization (1-F): 10, 20, 30, 40 and 50% (1-F), which are equivalent to 90 to 50% melt (F). D values (Table 4) were calculated using the equation

$$[2] \quad D = m_1K_1 + m_2K_2 + m_3K_3 + m_4K_4$$

(Rollinson, 1993) assuming crystallization proportions (m) of 0.10 olivine, 0.50 clinopyroxene, 0.32 plagioclase, and 0.08 magnetite (compiled by Condie for tholeiitic magma at shallow depths, personal communication, 2001) and the partition coefficients

Table 4 Bulk distribution coefficients (D and P) for fractional crystallization and batch melting (where appropriate) calculated from the partition coefficients (K) listed on Table 5.

Element	D (fxl)	D (melting)	P (melting)
Th	0.04	0.009	0.02
Ta	0.08	0.004	0.007
La	0.2	0.008	0.03
Yb	0.4	1	3

Table 5 Mafic partition coefficients (K) from Rollinson (1993) and Condie (personal communication, 2001).

Element	olivine	clinopyroxene	plagioclase	magnetite	orthopyroxene	garnet
Th	0.004	0.05	0.05	0	0.008	0.001
Ta	0.002	0.008	0.04	0.8	0.005	0.006
La	0.00001	0.07	0.15	1.5	0.007	0.002
Yb	0.02	0.60	0.07	0.9	0.15	7.0

(K) listed in Table 5.

When the resulting values are plotted on the Th/Ta-La/Yb diagram (Fig. 28), fractional crystallization is shown to have a negligible affect on La/Yb (3.88-4.34) and virtually no affect on Th/Ta (1.60-1.64) for up to 50% fractional crystallization. Unlike compatible elements like Ni, incompatible trace element ratios in the Iron King plume volcanics are relatively unaffected by fractional crystallization.

Partial melting

A similar model can be constructed to demonstrate the effect of batch melting on the Th/Ta and La/Yb ratios in the Iron King Volcanics using the batch melting equation

$$[3] (C_L = C_O/[D+F(1-P)])$$

from Rollinson (1993), where C_O is the source solid, C_L is the melt, D is the bulk distribution coefficient of the solid at the onset of melting; F is the fraction of melting (assuming 20 percent); and P is the bulk distribution coefficient of the minerals that go into the melt. Since the composition of the mantle source for the Iron King magmas is unknown, an assumption is made that the source (C_O) was that of primitive mantle.

The bulk distribution coefficient D , shown on Table 4, was calculated assuming melting with garnet left in the restite using equation [2]. The partition coefficients (K) are for a garnet lherzolite source (Table 5). The mineral proportions (m) are 0.60 olivine, 0.10 clinopyroxene, 0.15 orthopyroxene, and 0.15 garnet (compiled by Condie, personal communication, 2001). The partition coefficient P , also shown on Table 4, was calculated using the equation

$$[3] \quad P = p_1K_1 + p_2K_2 + p_3K_3 + p_4K_4$$

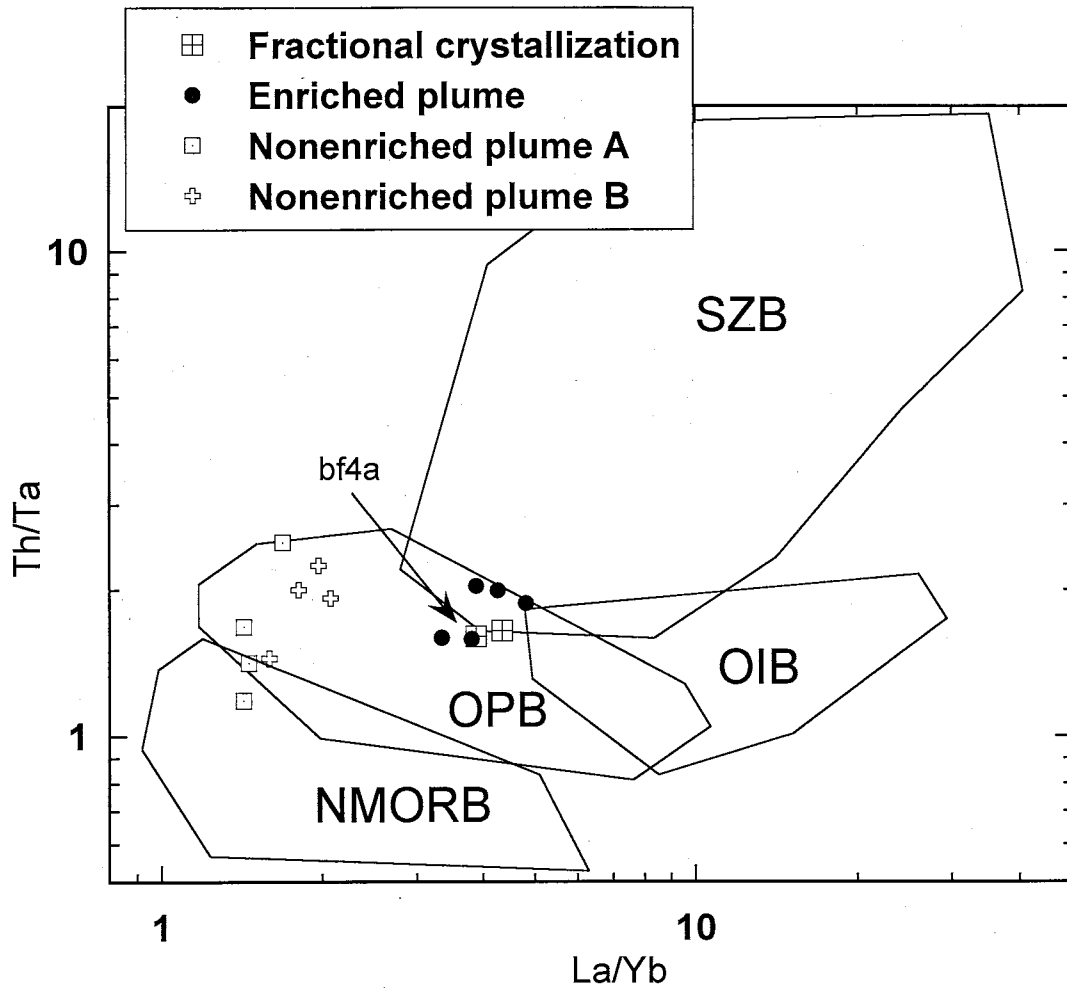


Fig. 28 Calculated results for fractional crystallization model for the Iron King Volcanics. Fractional crystallization was calculated from 10 to 50% crystallization ($1-F$). Sample bf4a was established as C_0 , a representative starting melt responsible for the Iron King plume basalts, based on its high MgO value. Squares with crosses represent the melt values (C_L) at 10% (left) and 50% (right). Fields for N-MORB, OPB, OIB, and island arc basalts (SZB) from Tomlinson and Condie (2001).

where p is the fraction of the mineral contributed to the melt: 0.05 olivine, 0.45 clinopyroxene, 0.05 orthopyroxene, and 0.45 garnet (compiled by Condie, personal communication, 2001).

The resulting plot (Fig. 29) indicates that like fractional crystallization, the Th-Ta ratio changes little during partial melting (1.92 to 2.06), while the La/Yb ratio varies from 25 to 4.5 for 20% melting. The large variation of La/Yb during batch melting is attributed to the presence of garnet in the restite. The Yb concentration in the melt is low at only 5% melting, but by 20% melting, its concentration is much greater, since it is retained in residual garnet.

This model supports that the mineral phases left in the restite can have considerable control on the incompatible element distribution in magma. The depth and pressure at which melting takes place and the amount that the source is melted also have considerable control over how partial melting changes magmatic trace element distributions.

Source material control on melting

Another set of incompatible element ratios that are particularly sensitive to mineral phases present in the source is La/Sm and Sm/Yb. We have already seen that Yb is sensitive to the presence of garnet in the restite. White and Duncan (1996) used factor analysis to show that variations of highly incompatible elements such as La are also dominated by partial melting, but are virtually unaffected by fractional crystallization. Light REE such as La are more incompatible in most mantle phases (such as spinel) than middle REE such as Sm (Lassiter and DePaolo, 1997). Lassiter and DePaolo (1997)

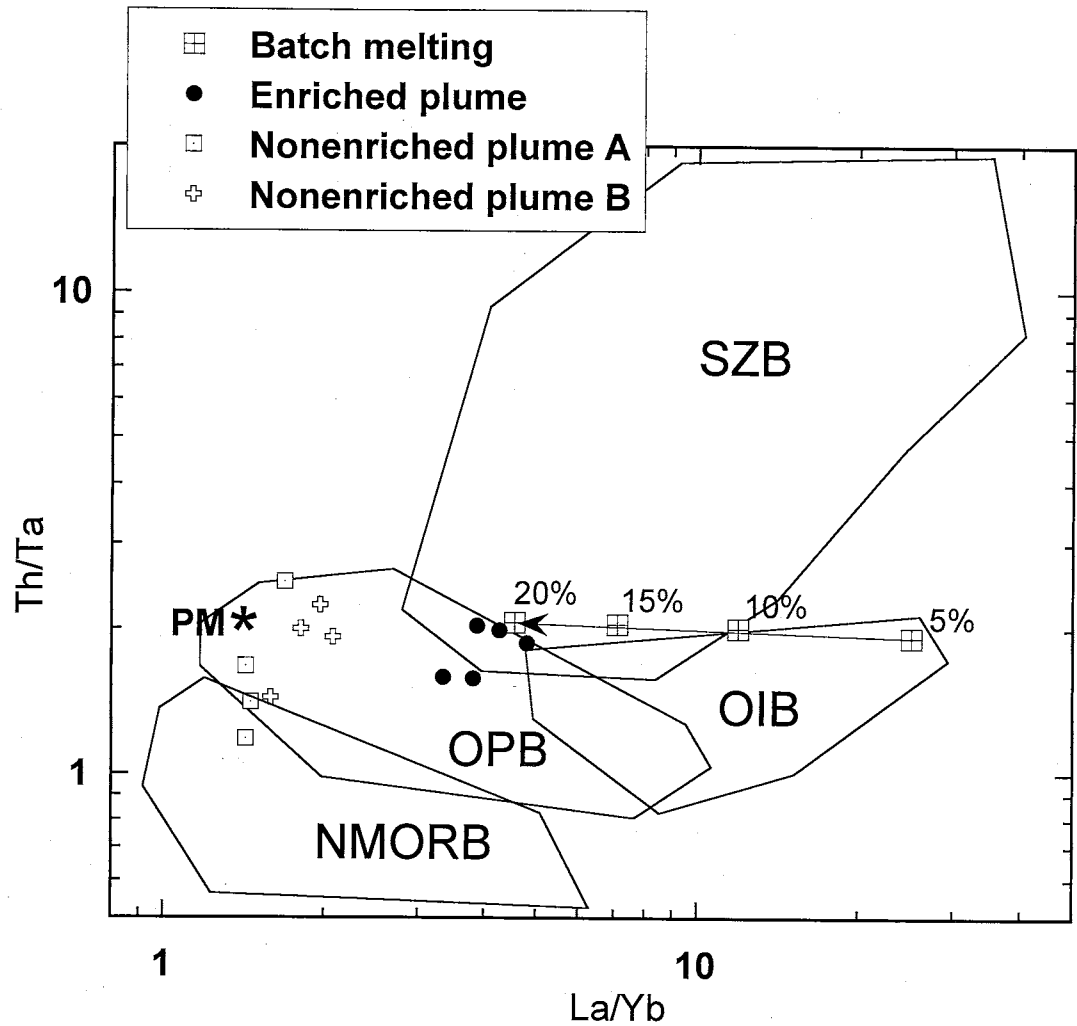


Fig. 29 Calculated melt compositions (C_L) of a batch melting model. Primitive mantle (PM) was used as C_0 , the original source. Batch melting was calculated for four degrees of melting (F) 5, 10, 15 and 20%. Fields for N-MORB, OPB, OIB, and island arc basalts (SZB) from Tomlinson and Condie (2001). Primitive mantle (PM) from Sun and McDonough (1989).

showed that when used together La/Sm and Sm/Yb have a very useful relationship. First, the graph has a positive correlation in basalts affected by partial melting (Fig. 30).

Second, basalts that have a subvertical trend indicate melting of spinel peridotite, whereas basalts that show a roughly horizontal trend indicate melting of a garnet peridotite. In the case of the Iron King Volcanics, the enriched plume components are clearly set apart from the nonenriched plume components, suggesting a higher degree of melting for the nonenriched plume rocks. Furthermore, the relatively flat positive trend of the Iron King plume basalts supports a garnet lherzolite source and indicates a melting depth of greater than 75 km because of the instability of garnet at shallower depths (Lassiter and DePaolo, 1997).

Depth of melting

Although OPB and OIB are both produced by plumes, they have significantly different geochemical signatures. This difference is related to the depth and degree of melting of the two basalt types. As we have already seen, trace element distributions of OIB are enriched in the most incompatible elements. Kerr et al. (2000) state that this indicates deep melting within the garnet stability field. The flat REE distribution of OPB indicates either shallow melting or high degrees of melting in the garnet stability field that result in no garnet left behind in the restite (Kerr et al., 2000), a possibility already suggested by the La/Sm-Sm/Yb graph (Fig. 30).

It can be shown using the relationship of Al_2O_3 to pressure that melting of the Iron King source occurred within the garnet stability field. Herzberg (1995) showed that the melting pressure of a magma (and therefore its depth of melting) can be determined

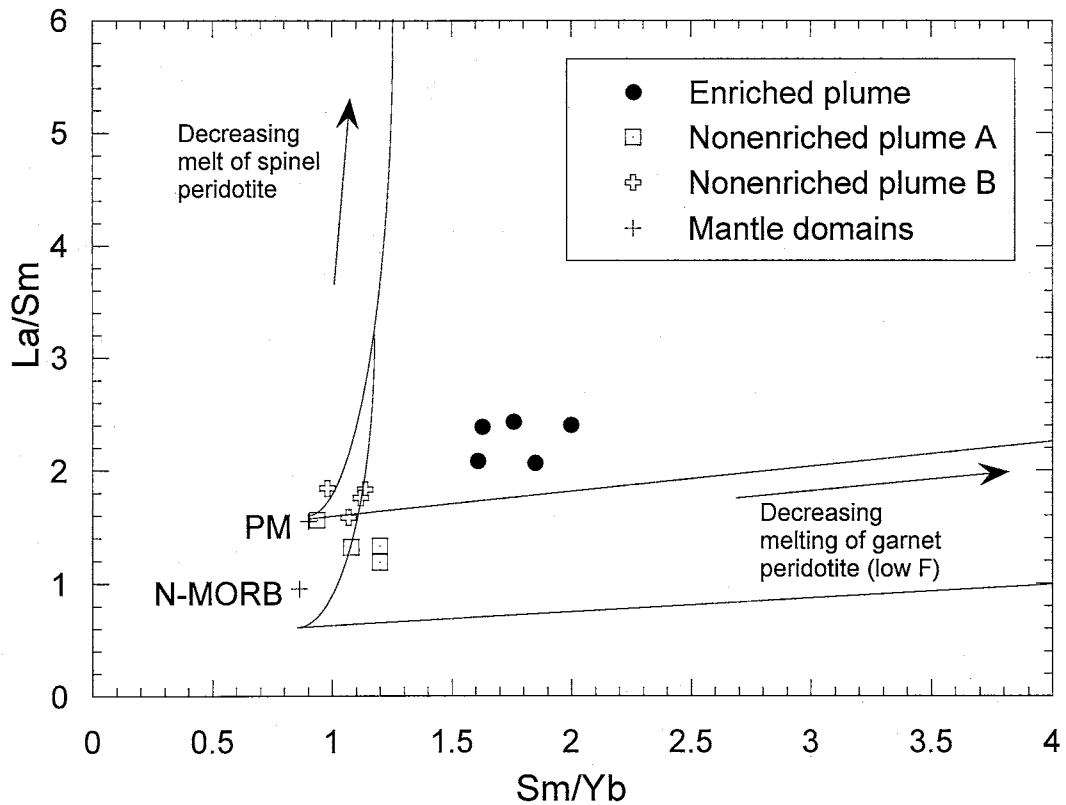


Fig. 30 La/Sm and Sm/Yb diagram of Iron King Volcanics after Lassiter and DePaolo (1997). Primitive mantle and N-MORB values from Sun and McDonough (1989). The plume basalts follow the decreasing melting of garnet peridotite. This supports the idea that the Iron King plume component originated in the garnet stability field below 75 km.

by the relationship of Al_2O_3 to $\text{CaO}/\text{Al}_2\text{O}_3$. At high pressures, the solubility of the garnet (a high Al mineral phase) is reduced. Therefore, magmas produced at high pressures have low concentrations of Al, which remains behind in the restite. Herzberg (1995) found that these variables change with depth with a predictable gradient. Figure 31a-b is a graph of Al_2O_3 to $\text{CaO}/\text{Al}_2\text{O}_3$ with Herzberg's fields and pressure points. The fields (or sails, as Herzberg calls them) represent primary magmas generated between the solidus and liquidus. The significance of the sail can be demonstrated by describing what happened to a primary magma between the pressures of 2.5 and 4 GPa. The $\text{CaO}/\text{Al}_2\text{O}_3$ ratio of the magma is controlled by the presence of garnet and clinopyroxene. The ratio remains on the solidus (on the left in this pressure range) until garnet in the solid is exhausted. Once it is melted, $\text{CaO}/\text{Al}_2\text{O}_3$ is free to vary to a composition to the right of the solidus, but within the sail. After clinopyroxene is melted, $\text{CaO}/\text{Al}_2\text{O}_3$ will remain constant along the vertical line on the right. In Herzberg's study (Fig. 4, 1995), Hawaiian tholeiites and alkali basalts plot around pressures of 2 to 4 GPa, with the majority concentrated between 2 and 3 GPa. The Iron King plume basalts are plotted on Figure 31a, with pressure values ranging from 2 to 3 GPa. Figure 31b is a graph of Al_2O_3 to $\text{CaO}/\text{Al}_2\text{O}_3$ on which values from modern oceanic plateau and older oceanic plateau terranes are plotted. Their distribution is very similar to that of the Iron King plume basalts. Most of the modern oceanic plateaus plot within Herzberg's field, but several of the plateau basalts, along with some of the Iron King basalts, plot to the left of the solidus. This is likely an effect of decreasing clinopyroxene and increasing secondary minerals in the rocks with alteration and can be demonstrated by observing the distribution of samples taken from the Hikurangi Plateau plotted on Figure 31b.

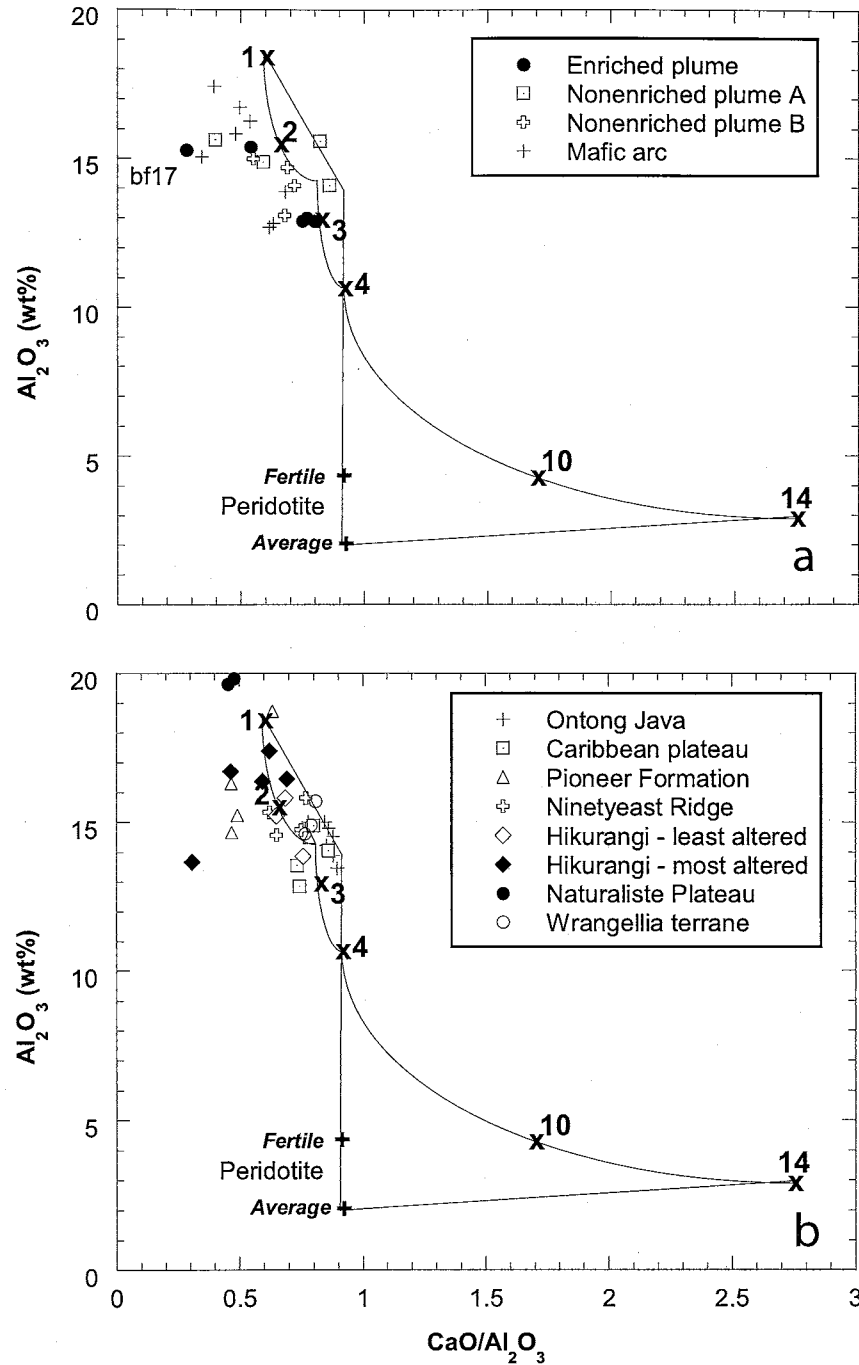


Fig. 31a-b Al_2O_3 vs. $\text{CaO}/\text{Al}_2\text{O}_3$ graph for (a) Iron King Volcanics and (b) other oceanic plateaus. Fields and numbers representing the pressures in GPa from Herzberg (1995). The sails represent primary magmas generated between the solidus (line that contains the pressure values) and the liquidus (that crosses the solidus at 4 GPa). Data for oceanic plateaus are from Mahoney et al. (1993), Neal et al. (1997), Kerr (1997), Dostal and Church (1994), Frey et al. (1991), Mortimer and Parkinson (1996), Mahoney et al. (1995), and Barker (1994).

Parkinson (1996) divided these rocks into groups of least altered and most altered.

The most altered samples plot to the left of the solidus. It is notable that the Iron King basalt with the highest LOI value (bf17) plots far to the left of the solidus also.

Nevertheless, several of the Iron King basalts plot within or close to Herzberg's OP field, between 2 and 3 GPa. These pressures correspond with melting depths of 64 to 96 km and are consistent with depths within the garnet stability field.

Degree of melting

The distribution of heavy rare earth elements (such as Yb and Lu) and Y provide significant information about the degree of melting of mafic magmas. They have a strong affinity for garnet, which, when present in the restite, serves to retain HREE during small degrees of melting when other incompatible elements are partitioned strongly into the melt. This can be seen from their partition coefficients (Table 5). All other partition coefficients for any element or mineral phase differ from HREE in garnet from 1 to 3 orders of magnitude. Magmas that have undergone high degrees of melting of the source contain considerable amounts of HREE if garnet is completely melted.

Two diagrams discussed earlier show the effect of melting on the Iron King Volcanics and have been reproduced in Figure 32 to emphasize this effect. The Th/Ta-La/Yb graph (Fig. 32a) has Yb in the denominator of the ratio on the x-axis.

We would expect basalts with higher degrees of melting to lie to the left of basalts with lower degrees of melting. In the case of the Iron King samples, the depleted plume samples lie far to the left, closest to primitive mantle values. This indicates that the source of the depleted plume samples underwent greater melting than the source of the

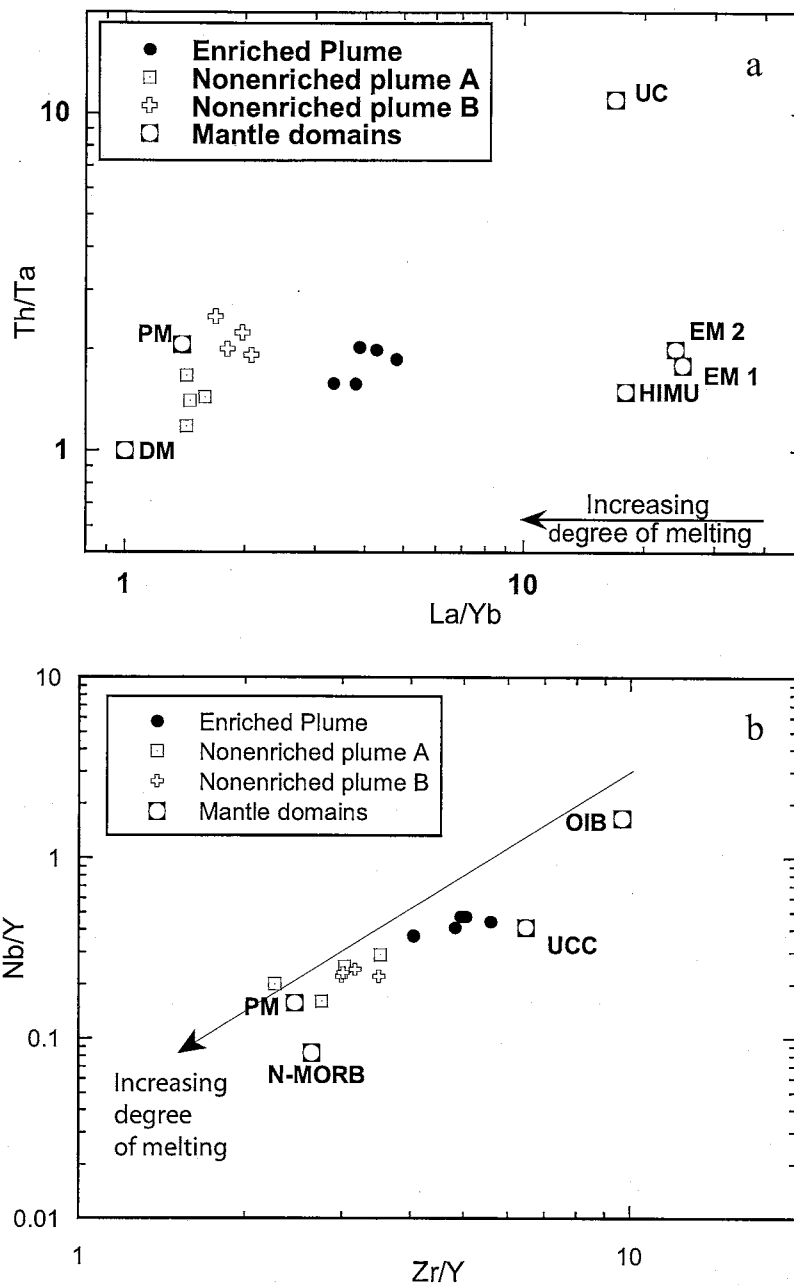
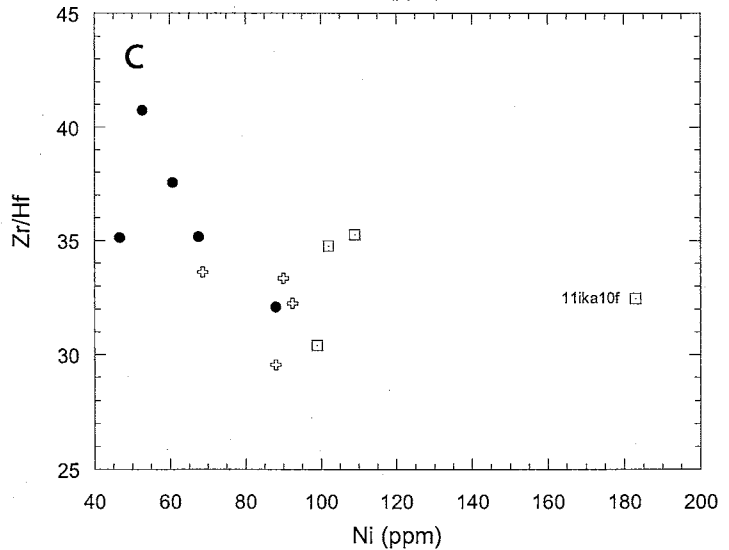
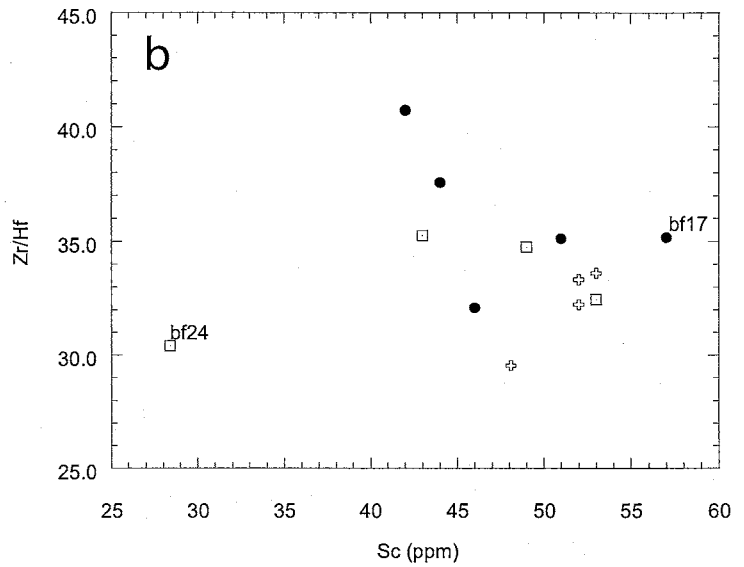
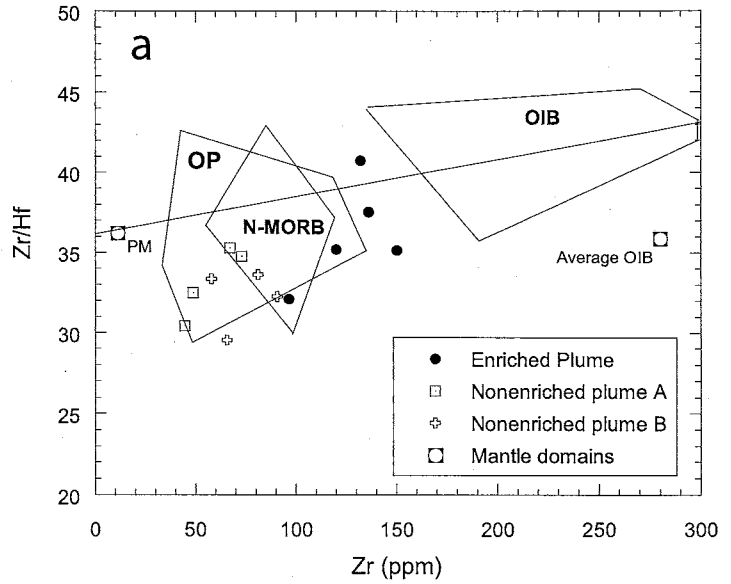


Fig. 32a-b Trace element diagrams that demonstrate the effect of small to large degrees of melting on trace element ratios. In both cases, nonenriched plume subgroup A displays the largest degree of melting and the enriched plume group shows the smallest degree of melting. Primitive mantle (PM), N-MORB and OIB values from Sun and McDonough (1989). Upper continental crust value (UCC) from Condie (1993). Trend lines in (a) from Tomlinson and Condie (2001). Trend line in (b) is general direction of increasing degree of melt described by Fitton et al. (1997).

enriched samples. In the depleted plume samples, more garnet would have been melted, releasing more Yb to the melt, in turn lowering the La/Yb ratio. Yttrium is also controlled by garnet, and for the same reasons described above, samples that plot to the lower left on the Nb/Y and Zr/Y graph (Fig. 32b) have undergone greater degrees of melting. A general trend line has been included on Figure 32b that illustrates the findings of Fitton et al. (1997): Fractional melting trends of garnet and spinel lherzolite generally follow the Iceland array, and increasing degrees of melt cause lower Nb/Y and Zr/Y ratios.

Hafnium and Zr are fractionated in the Iron King Volcanics rather than retaining the primitive mantle ratio considered common to oceanic basalts. David et al. (2000) studied the problem of Hf-Zr fractionation and showed that although fractional crystallization can affect the Zr/Hf ratio, partial melting usually controls the ratio of Zr and Hf. In a graph of Zr/Hf vs. Zr (Fig. 33a), the authors found that MORB and OIB can be distinguished from each other by their degrees of melting (about 10% and 3 to 5% respectively). David et al. (2000) attribute this behavior to differences in partition coefficients between the two elements ($D_{\text{Hf}} > D_{\text{Zr}}$). The line in Figure 33a illustrates the trend along which melting occurs, with magmas produced by the highest degree of melting on the left. In the case of the Iron King Volcanics, the basalts fall near the MORB field, suggesting they represent melts of about 10% rather than the 20% melt suggested for some oceanic plateaus. As expected, the enriched subgroup shows the smallest degree of melting. David et al. (2000) also illustrate the effect of fractional crystallization on the Zr/Hf ratio by comparison to compatible elements such as Sc and Ni. They found that Sc showed a negative correlation with Zr/Hf, indicative of the effect

Fig. 33a-c Zr/Hf vs. Zr (a), Sc (b) and Ni (c) for the Iron King Volcanics. Key is the same for all diagrams. David et al. (2000) found that OIB and MORB follow the trend line in (a) from right to left as the degree of melting increases. N-MORB and OIB fields from David et al. (2000). OP field reflects data from Frey (1991), Mahoney et al. (1993), Kerr et al. (1997), Sinton et al. (1997) and Dostal and Church (1994). N-MORB, primitive mantle and OIB average values from Sun and McDonough (1989).



of clinopyroxene crystallization. In the case of the Iron King rocks, a weak trend was found on the Sc graph (Fig. 33b), and unlike the study by David et al. (2000) a weak negative crystal fractionation trend was also evident on the Zr/Hf vs. Ni graph (Fig. 33c), indicative of olivine crystallization. However, since both trends are weak and D_{Hf} (0.04) is only slightly higher than D_{Zr} (0.01) for olivine, it is possible that fractional crystallization plays only a small part in the fractionation of Zr and Hf, whereas the affect of degree of partial melting is more significant.

Difference between enriched and nonenriched plume components

It is clear that varying degrees of melting of a garnet lherzolite source may account for the observed differences between the enriched and nonenriched subgroups of plume-derived Iron King Volcanics. Fractional crystallization cannot be a factor because the crystallization only redistributes the major elements and some compatible elements, not the incompatible trace elements by which the two populations are identified. The same is true for alteration and crustal contamination. It is unlikely that the plume subgroups were created by differing depths of melting, because the two groups plot together on the depth of melting diagrams, $\text{CaO}/\text{Al}_2\text{O}_3$ vs. Al_2O_3 .

Varying degrees of melting in the Iron King mantle plume source could have been caused by two different processes: (1) lithospheric thinning above the plume resulting in early versus late melting phases, or (2) varying degrees of melting related to location of melting in the plume head.

The first possibility involves erupting the two subgroups at different times during decompression melting of the plume. The lithosphere is thinned during extension and

incubation by the underlying mantle plume. Lassiter and DePaolo (1997) describe the case of continental flood basalts in which high degrees of melting are achieved as the lithosphere is thinned. Geochemical changes within many flood basalts indicate increasing melt fraction and decreasing depth of melting as eruption progresses from early to late phases (Condie, 2001). Although oceanic plateaus differ geochemically from continental flood basalts, studies indicate that some lithospheric thinning may occur during the creation of an oceanic plateau, even though the "lithospheric geochemical signature" found in continental flood basalts is missing and the degree of melting is lower than that of continental flood basalts (Lassiter and DePaolo, 1997). If this were the case for the Iron King Volcanics, the enriched group that was generated by smaller degrees of melting would have melted earlier at greater lithospheric thickness than the nonenriched group. As a plume rises to the lithosphere, adiabatic decompression results in higher temperatures and causes progressively greater degrees of melting (Condie, 2001).

The enriched plume magma could have been erupted early during a period of small degrees of melting, not only picking up a geochemical signature indicative of the degree of melting, but carrying a signature similar to the original plume source. This would explain why this subgroup has incompatible element distributions similar to OIB. As melting increased, oceanic crust (MORB) may have been assimilated by the plume head, producing the nonenriched subgroup. A problem with this proposal is the relationship of the Iron King Volcanics to MORB on the graph of Nb/Y vs. Zr/Y (Fig. 24). If the depleted mantle region that produces MORB had been mixed with the source melt of the Iron King plume basalts within the mantle, we would expect the Iron King

basalts to fall within the MORB array. Instead, they fall within the plume array between the depleted and enriched end members.

The composition of the enriched and nonenriched plume basalts could also reflect regions with different compositions in a mantle plume head. It is proposed that as the plume rose, it entrained more enriched mantle as the plume head developed. The enriched plume material was incorporated into the outer regions of the plume head, while the central region of the plume head remained relatively nonenriched. High degrees of melting occur in the central part of the plume head where temperatures increase at a given depth as the plume rises (Condie, 2001). In the distal regions of the plume head, lower temperatures are retained, and smaller volumes of melt are produced. Alkaline magmas are produced in these cooler, outer regions of the plume. Interestingly, the enriched Iron King plume rocks, which reflect lower degrees of melting, also plot closer to the alkali basalts field on the Zr/TiO₂ versus Nb/Y classification diagram (Fig. 12). They are also enriched in incompatible elements, a characteristic common to alkali basalts (Fisher and Schmincke, 1984). A similar theory could explain why the two nonenriched subgroups developed a slightly different geochemical signature: perhaps nonenriched subgroup A formed closest to the plume center, while nonenriched subgroup B formed further away. On graphs that indicate degrees of melting trends (Fig. 32), nonenriched subgroup A consistently shows greater degrees of melting. The nonenriched B group retained a nonenriched character, but also developed a geochemical signature resulting from smaller degrees of melting.

Models for the association of Iron King plume volcanics with arc volcanics

There are four possible models for the association of the Iron King arc component with the Iron King plume component: (1) The two components developed separately, but were accreted to the continent at about the same time; (2) the two developed separately and then collided before their accretion to the continent; (3) the arc component developed on the edge of an oceanic plateau before the whole mass was accreted; or (4) the arc component developed on the edge of an oceanic plateau after it collided with the continent.

The separate development of the two components suggested in scenario 1 is feasible since the two components have no apparent geochemical affinities. But because the deformational features in both components are identical and because they are structurally interfingered, it is unlikely that the arc and plume components were accreted as separate bodies as suggested in the first model.

In the second model, the arc component could have developed as an island arc in the vicinity of a subduction zone. As the oceanic plateau entered the subduction zone, it may have collided with the island arc. This event is similar to the collision of the Solomon Islands with Ontong Java oceanic plateau in the Eocene (Petterson et al., 1999). Petterson et al. (1999) described an event in which the Ontong Java plateau approached a subduction zone between the Pacific Plate and the Australia-India Plate and jammed subduction and stopped formation of the Vitiaz Arc above the subduction zone. This jamming flipped the subduction direction from the southwest to the northeast and forced the arc system into an accretionary prism on the side of the plateau. Should the Iron King plume and arc components have become associated in such a manner, a portion of the

accretionary prism and the oceanic plateau on which it was attached could have become obducted to the North American continent and preserved in the rock record. However, there is no evidence in the Iron King Volcanics for trench sediments or melange common to accretionary prisms, so this model seems improbable.

The third model is another scenario in which the oceanic plateau approached, jammed and flipped a subduction zone. After this event, ocean floor began subducting beneath the plateau, allowing an island arc to develop along the edge of it. As with the previous model, the arc basalts ride on top of the oceanic plateau, so when an upper portion of the oceanic plateau is obducted, the oceanic arc is also.

Petterson et al. (1999) provide additional models for the obduction of oceanic plateaus onto continental crust, one that suggests a fourth model for the Iron King Volcanics. An oceanic plateau collides with the continent, and because of its thickness, it successfully clogs the subduction zone and forces the subduction zone to "backstep" to behind the plateau (Fig. 34). In this way, subduction continues in the same direction rather than flipping direction. The subduction zone is now pulling oceanic floor beneath the plateau, and arc volcanoes begin erupting on the outer edge of the oceanic plateau. In the case of the Iron King Volcanics, the collision of the plateau with the continent is followed by subsequent collision of additional terranes with the now accreted Iron King Volcanics. It is possible that collisions on the outer edge of the oceanic plateau where the arc volcanics formed are sufficient to cause the deformational and structural features now seen in both the plume and arc components. If this activity can successfully explain the deformational and structural features, it is the preferred model, because long-time unidirectional growth of the continent, such as that found in the southwest United States,

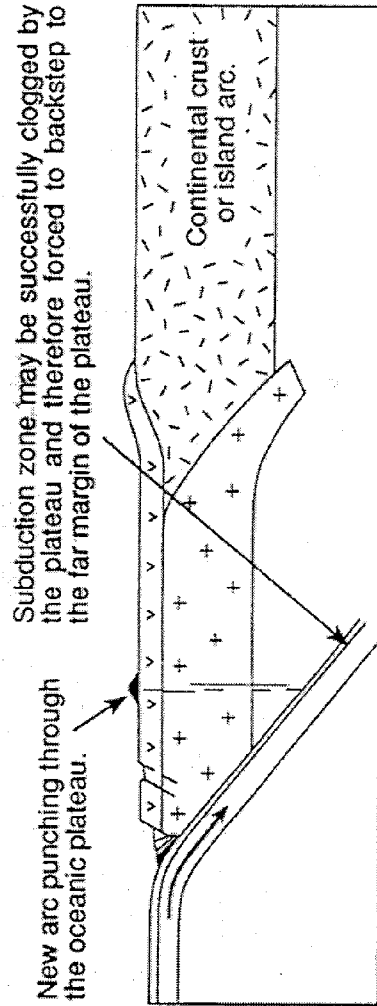


Fig. 34 Diagram from Petterson et al. (1999) demonstrating a possible model for the accretion of the Iron King Volcanics. The oceanic plateau collides with a continent, obducting some material and jamming the subduction zone. Subduction is forced from in front of the oceanic plateau (a) to behind the plateau (b). A new arc develops on top of the oceanic plateau. Collisions of additional oceanic terranes occur on the backside of the plateau.

suggests that the direction of subduction may have remained consistent throughout the Yavapai Orogen. A problem with this model is related to the probable obduction involved in the preservation of the Iron King Volcanics. None of the deeper ultramafic rocks expected in an oceanic plateau are present in the Iron King Volcanics. It is likely that a back-stepping subduction zone would prevented the full subduction of such lower oceanic plateau ultramafic units and obduction of the upper mafic units. If this model were the correct one, the presence of ultramafic rocks is expected.

CONCLUSIONS

To support the importance of mantle plume sources to the generation of continents, it is necessary to show that fragments of oceanic plateaus and ocean islands are present in the continents in significant volumes. The recognition of remnants of oceanic plateaus in the continental rock record is not yet significant. The tectonic provinces found in the southwest United States have for decades been considered juvenile terranes that were accreted to the continent between 1.8 and 1.65 Ga (Hoffman, 1988, 1989). These terranes were largely interpreted to be arc greenstones (Anderson and Silver, 1976; Smith, 1992; Condie, 1986). The lithologic and geochemical evidence has already been presented that identifies one of these greenstones as a previously unrecognized fragment of an oceanic plateau associated with an island arc sequence. The 1.75-Ga Iron King Volcanics was accreted to the North American continent around 1.70 Ga.

The lithologic evidence that supports an oceanic source for the Iron King Volcanics include pillow basalts, hydrothermal sediments, volcanoclastic breccias and tuff. Basalts dominate the oceanic plateau sequence. Felsic and intermediate volcanics dominate the arc volcanic sequence. Geochemical evidence to support an oceanic plateau origin includes flat rare earth element and incompatible element distributions and trace element ratios. When compared to other oceanic tectonic environments, such as oceanic plateaus, ocean islands, island arcs and mid-ocean ridges, the Iron King Volcanics reflect the geochemical signature of an oceanic plateau.

Geochemical results also allow us to make several interpretations about the mantle source and the processes that acted on the Iron King plume component before its extrusion. The Iron King plume-derived basalts are further divided into an enriched and a nonenriched group based on REE and incompatible element distributions as well as incompatible element ratios. The trace element distributions in these two populations were differentiated in part as a result of different degrees of melting related to location within the mantle plume head and possibly through compositional variations within the plume. It is proposed that the primary plume came from a deep depleted source and that the more enriched material was added to the plume during entrainment. The enriched Iron King subgroup shows evidence of smaller degrees of melt than the nonenriched population. The smaller degrees of melting are attributed to a location in the plume head that is distant from the hotter, central plume tail from which the nonenriched population may have originated. Although the melting that produced the Iron King plume magmas probably occurred at shallow depths (<100 km), the melt was generated within the garnet stability field (>75 km).

Two models are proposed for the association of plume-generated basalts and the island-arc volcanics based on similar deformation apparent in the two groups:

- (1) An oceanic plateau and an island arc developed separately and collided with the continent separately.
- (2) An oceanic plateau approached and possibly clogged a subduction zone. In the process an island arc formed on the edge of the plateau. The whole body of volcanic material was accreted to Laurentia around 1.7 Ga.

- (3) The Iron King plateau collided with an island arc, and the whole composite was then accreted to the continent around 1.7 Ga.
- (4) An oceanic plateau collided with the continent, forcing the subduction zone to back-step from the front of the plateau to the back of the plateau. An arc system developed on the back edge of the plateau. More oceanic terranes collided with the plateau along this edge.

Additional studies are suggested to test these models: dating of the arc and plume components separately, a ground magnetic survey to better determine how the arc and plume components are distributed of the Iron King Volcanics, and Nd and Os isotope studies to verify that the two components come from different mantle sources.

APPENDIX A

Petrographic report of the Iron King Volcanics

Six thin sections were examined as part of this study: five amphibolites and one quartz-sericite schist. Of the amphibolites, protoliths include two basalts, two basaltic andesites, and one andesite based on geochemical classification. The quartz-sericite schist protolith is considered to be rhyolitic flow or tuff (Anderson, 1972).

Sample **bf1** is a fine-grained amphibolite with 45 to 50% non-twinned to poorly twinned plagioclase and quartz, 30 to 40% hornblende, 10 to 20% chlorite and 3 to 5% opaque minerals, such as ilmenite or magnetite. Trace minerals include apatite, hematite and clinozoisite. Foliation is defined by bands of amphibole and plagioclase. Amphibole has rounded to ragged edges, although some amphiboles show relict subhedral shapes. Chlorite has a similar form and pleochroic colors similar to amphibole, a feature characteristic of all of the amphibolites. The plagioclase and quartz crystals in bf1 vary from xenoblastic to idioblastic in about equal portions. The quartz in all six thin sections displays undulatory extinction.

Sample **bf5b** is an amphibolite with 40% plagioclase, 30-40% hornblende, 10-20% chlorite and <5% opaque minerals. The coarse-grained crystals are predominantly amphibole, whereas xenoblastic quartz and poorly twinned plagioclase make up the surrounding fine-grained material. Accessory minerals include clinozoisite, hematite and calcite. The sample is highly altered, but appears to reflect lower amphibolite to upper greenschist facies mineralogy. Foliation is weak, controlled by plagioclase and quartz.

Amphiboles have very ragged edges. Quartz and plagioclase display primarily xenoblastic textures.

Sample **bf6** is an amphibolite with 40 to 50% plagioclase and quartz, 30 to 40% hornblende, 20% chlorite and 3 to 5% opaque minerals. Trace minerals include calcite and hematite. No relict textures are preserved, and foliation is poor, limited to bands of plagioclase and quartz.

Sample **bf9** is the only sample studied of metarhyolite from the Iron King Volcanics. It is a quartz-sericite schist with relict phenocrysts of mainly quartz that are surrounded by very fine-grained quartz, non-twinned to poorly twinned plagioclase, and sericite. The sample contains about 5 to 10% quartz phenocrysts, 60% fine-grained quartz and plagioclase, and 30% fine-grained sericite. Accessory minerals include opaque minerals, hematite, chlorite and zircon. The rock has a well-developed foliation defined by sericite. The relict phenocrysts retain euhedral faces although most show sericite alteration within and on the edges of the crystals.

Sample **bf13** is a very fine-grained, well-foliated amphibolite and from the major element composition, it probably had an andesite protolith. Mineral distributions are 30 to 40% sericite, 20 to 30% hornblende, 25% plagioclase and quartz, 5 to 10% opaque phases, and 5 to 10% calcite. Hematite is present as an accessory mineral. Although **bf13** is very fine-grained, larger grains of quartz, plagioclase, opaque minerals, amphibole and muscovite are present.

Sample **bf22**, an amphibolite, differs from the other amphibolite samples (**bf1**, **bf5b**, **bf6**, **bf13**) in that it clearly belongs in the greenschist metamorphic facies rather than the amphibolite facies. It contains 20 to 25% actinolite, 30% quartz and plagioclase,

30% chlorite, 3 to 5% opaque minerals, <5% calcite and <5% epidote. More than 40% of the material is sericitized, especially within the plagioclase and quartz. Accessory zircon is also present. Foliation is poor in this sample, in part because foliation has a bi-directional habit. Although not strongly twinned, calcite in this sample follows foliation. It is likely a secondary mineral, filling in spaces between other minerals.

APPENDIX B

Analytical methods

About 500 grams of the 14 samples chosen for chemical analysis were ground in an agate mill. Major element analysis was completed by standard X-ray fluorescence spectrometry (XRF) at XRAL Laboratories, Don Mills, Ontario. The detection limits are listed on Table 6.

Qianli Xie, manager of the geochemical laboratory at the Department of Geological Sciences, University of Saskatchewan, oversaw the trace element analysis, which was done by inductively coupled plasma mass spectrometry (ICP-MS), using a Perkin Elmer Elan 5000 spectrometer. The analytical methods of Jenner et al. (1990) were used. Samples were prepared using HF-HNO₃ closed-vessel digestion and Na₂O₂ sinter sample digestion. Two sample preparation methods were necessary because some samples contain refractory mineral phases that do not always completely dissolve by the HF-HNO₃ closed-vessel dissolution method (Xie, personal communication). These mineral phases include zircon and baddeleyite, which contain Zr and Hf (Xie and Kerrich, 1995). Data for high-field strength elements such as Zr, Nb, Y, Hf and Ta, and the rare earth elements were collected using solutions prepared by the Na₂O₂ sinter method. The remaining trace elements were analyzed in solutions made using the HF-HNO₃ method. Fan and Kerrich (1997) state that this combination of methods produces reproducible data. Xie provided the following descriptions of the two preparation methods.

Table 6 Detection limits of major and trace element analyses for the Iron King Volcanics. Trace element detection limits are not applicable to samples analyzed by Vance (1989).

Oxide or element	Detection limits
SiO ₂ (wt %)	0.01
TiO ₂ (wt %)	0.001
Al ₂ O ₃ (wt %)	0.01
Fe ₂ O _{3 T} (wt %)	0.01
MgO (wt %)	0.01
CaO (wt %)	0.01
Na ₂ O (wt %)	0.01
K ₂ O (wt %)	0.01
MnO (wt %)	0.01
P ₂ O ₅ (wt %)	0.01
Rb (ppm)	0.154
Ba (ppm)	0.093
Sr (ppm)	0.151
Th (ppm)	0.006
U (ppm)	0.006
Sc (ppm)	0.601
V (ppm)	0.033
Cr (ppm)	0.003
Co (ppm)	0.0001
Ni (ppm)	0.005
Y (ppm)	0.004
Zr (ppm)	0.013
Nb (ppm)	0.004
Hf (ppm)	0.01
Ta (ppm)	0.001
La (ppm)	0.004
Ce (ppm)	0.01
Pr (ppm)	0.003
Nd (ppm)	0.02
Sm (ppm)	0.018
Eu (ppm)	0.01
Gd (ppm)	0.019
Tb (ppm)	0.005
Dy (ppm)	0.004
Ho (ppm)	0.004
Er (ppm)	0.01
Tm (ppm)	0.002
Yb (ppm)	0.009
Lu (ppm)	0.005

In the Na_2O_2 sinter digestion method, about 200 mg of each powdered sample is mixed with about 800 mg of ground Na_2O_2 in a dry, HCl-washed nickel crucible. The crucibles were then heated in a muffle furnace at about 480°C for $1\frac{1}{2}$ hours. After cooling, each sample was removed from its crucible by adding distilled de-ionized water (DDI water) and loosening the solid with a glass stirring rod. The slurry was centrifuged to 1750 rpm for 10 minutes and decanted. Centrifuging and decanting was repeated. Two and a half ml of 8 N HNO_3 were added to each sample. The centrifuge tubes were placed in an ultrasonic water bath for 30 minutes. If the solids were not completely dissolved, ultra-pure oxalic acid was added and allowed to work on the solids for no more than 2 or 3 hours. The solutions were placed in 125-mL bottles, diluted to about 100 g with DDI water and shaken. At this point, the samples were ready for chemical analysis. The sample batch included one standard, one blank and one duplicate sample prepared by this method. The reference material used was MRG-1, an augite-olivine gabbro from Mount Royal at Montreal, Quebec.

To prepare the samples using the HF- HNO_3 closed-vessel digestion, 100 mg of rock powder of each sample was weighed into a Teflon beaker, which had been acid washed with HNO_3 and heated HCl and rinsed with ultra-pure water. One milliliter of concentrated, twice-distilled 16 N HNO_3 was swirled with each sample, followed by the addition of 1.5 ml of twice-distilled HF. Each beaker was heated to 100°C for three days. If at this point a sample was not completely dissolved, the solution was evaporated to dryness and the process was repeated. Once dissolved, each solution was once again evaporated, 2 ml of 8-N HNO_3 was added, and the new solution was heated for 30 minutes. This last step was repeated twice. The solution was then cooled and transferred

to a 125-ml bottle where it was diluted to 80 to 100 g with DDI water and shaken. At this point the sample was ready for analysis. As with the Na_2O_2 sinter method, one standard of MRG-1, one duplicate and one procedural blank was prepared by this method.

Before analysis by ICP-MS, several calibration solutions were prepared. These included two external calibration standards, STDA and STDB, acid blanks and spiked samples. The external calibration standards consisted of about 6 g of STDA and STDB. Unspiked samples were made of about 3.5 g sample and 3.5 g 0.2N HNO_3 . Spiked samples were made with 3.5 g sample and 3.5 g spike. Element concentrations for standards A and B and spikes are listed on Table 7. Acid blanks contained about 6 g of 0.2 N HNO_3 . During the run, every three samples were bracketed on each side with the two standards and an acid blank. Each sample was followed by a spiked sample. One duplicate was included for the whole batch. The run was concluded with the two standards and a blank of DDI water.

Detection limits, which measure instrument performance, vary among the trace elements (Table 6). The calculation was based on average acid blank plus one standard deviation. The reference standard MRG-1 was measured twice during the first run of the Iron King samples and once during a second run of the samples. A comparison of these measurements to the laboratory's average MRG-1 values and to the MRG-1 accepted values published by Govindaraju (1994) serves to indicate the data's accuracy. The MRG-1 values returned during the analysis of the Iron King Volcanics are listed on Table 8.

RSD percents for the elements discussed in this report are listed on Table 8 as well. This precision indicator was calculated from the values measured by several

Table 7 Element concentrations in the calibration standards STDA and STDB and the spike solution used for ICP-MS analysis (after Jenner et al., 1990).

Elements	STDA (ppb)	STDB (ppb)	Spike (ppb)
Rb	200	200	
Ba	600		10000
Sr	600		10000
Th	100		1500
U	100		1500
Sc	200		
Y		100	
Zr	200		5000
Hf	100		
La	100		2000
Ce	100		
Pr	100		2000
Nd	400		4000
Sm	400		4000
Eu		200	
Gd		400	
Tb		100	
Dy		300	
Ho		100	
Er	200		2000
Tm	100		700
Yb	100		
Lu	100		

Table 8 The reference standard MRG-1 was run three times during two runs of the Iron King Volcanics. Columns 2 and 3 contain the values collected during run 1. Column 4 contains the values measured during run 2. Column 5 contains the standard deviation of these runs. Column 6 contains the average values for MRG-1 as measured in the Department of Geological Science laboratory at the University of Saskatchewan. The laboratory's average includes more than 350 analyses since 1992. The relative standard deviation percent (% RSD) for the average in 6 is listed in column 7. The accepted values for MRG-1 as published by Gorvindaraju (1994) are listed in column 8. No values reported for Rb, Ba, Sr, Th, U, and Sc in the fourth column because they were not included in the second run.

Element	MRG-1 run 1, analysis 1	MRG-1 run 1, analysis 2	MRG-1 run 2	Standard deviation	U. of S. average	% RSD	Gorvindaraju (1994)
Rb	7.9	7.7	--	0.07	7.6	8	8.5
Ba	48	47	--	0.5	49	3	61
Sr	305	300	--	2.7	291	6	266
Th	1.14	1.05	--	0.045	0.89	11	0.93
U	0.25	0.29	--	0.020	0.26	10	0.24
Sc	56	62	--	2.9	61	8	55
Y	12.0	12.4	11.5	0.35	12.7	8	14.0
Zr	101	103	100	1.1	107	5	108
Nb	22	19	23	1.7	22	7	20
Hf	4.0	3.9	4.2	0.11	3.9	5	3.8
Ta	0.88	0.82	0.96	0.057	0.63	7	0.80
La	8.8	8.9	9.3	0.21	9.0	4	9.8
Ce	25	25	26	0.4	26	3	26
Pr	3.6	3.7	3.7	0.03	3.8	3	3.4
Nd	17.8	17.8	18.2	0.18	18.2	3	19.2
Sm	4.3	4.3	5.0	0.34	4.5	6	4.5
Eu	1.4	1.4	1.6	0.08	1.4	3	1.4
Gd	4.3	4.6	4.5	0.09	4.1	3	4.0
Tb	0.63	0.65	0.56	0.039	0.56	3	0.51
Dy	2.9	3.0	3.0	0.03	3.1	3	2.9
Ho	0.48	0.50	0.50	0.009	0.52	4	0.49
Er	1.17	1.22	1.19	0.021	1.23	4	1.12
Tm	0.15	0.14	0.14	0.005	0.15	5	0.11
Yb	0.82	0.79	0.85	0.024	0.85	5	0.60
Lu	0.14	0.14	0.15	0.005	0.11	6	0.12

different analysts using several different batches of MRG-1. More than half of the elements returned RSD% of 5 or less. Only two elements, Th and U, had RSD percents greater than 8, indicating good overall precision for the other elements. Thorium had the greatest percent at 11. The poor precision for Th and U may be related to their low concentrations in the standard.

Ni, Cr, Co and several other metals were analyzed separately. This precaution was necessary because instrument components made of Ni were used for the earlier analysis. During the separate analysis, a platinum-tipped sampler and platinum skimmer cones replaced the nickel sampler and cones usually used. The solution prepared by the HF-HNO₃ method was used for analysis of these metals.

Reanalysis

Nine samples were reanalyzed for REE and selected HFSE: bf1, bf3, bf4a, bf5b, bf6, bf9, bf17, bf14 and 11ika10f. The samples were rerun because several were found to have unexpected fractionation between Hf and Zr, between Nb and Ta, and between Yb and Y. Samples were prepared for the second run using only Na₂O₂ sinter sample digestion.

The two data sets and the percent differences between the values for each element are listed on Table 9. For several samples (bf1, bf3, bf14), the second analyses resulted in greater fractionation than the first. For this reason, some fractionation in the first data set was considered "real," especially between Hf and Zr. For most of the samples, the percent difference was <10%, including several samples with zero percent difference for Lu and Tm. Sample bf9, a schist with felsic volcanic origins, had the greatest differences

Table 9 Comparison of two different runs on the ICP-MS for nine Iron King Volcanics samples, procedural blanks and reference standards. Values are in parts per million, except for procedural blank (ppb). Percent difference = $[(A-B)/\text{average of A and B}] \times 100$; n.d. = not detected or below detection limits.

Element	Y	Zr	Nb	Hf	Ta	La	Ce	Pr	Nd	Sm	Eu	Gd	Tb	Dy	Ho	Er	Tm	Yb	Lu	
bf1 run 1	30	150	11.8	4.3	0.80	12.9	30.4	4.0	18.8	4.7	1.6	5.9	1.05	5.8	1.20	3.4	0.51	3.4	0.67	
bf1 run 2	28	145	11.6	4.8	0.91	13.5	31.3	4.3	19.6	5.5	1.8	6.3	0.95	6.0	1.22	3.4	0.52	3.4	0.67	
% difference	6	3	2	11	13	5	3	5	4	4	15	15	7	10	4	2	0	2	1	0
bf3 run 1	24	96	7.4	3.0	0.51	8.2	20.4	2.9	14.0	3.9	1.4	4.9	0.88	4.8	0.98	2.8	0.39	2.5	0.51	
bf3 run 2	20	87	7.2	3.3	0.56	8.4	20.7	2.9	14.7	4.5	1.6	5.1	0.80	4.9	1.01	2.9	0.42	2.7	0.51	
% difference	15.9	10.1	2.3	8.0	9.3	2.3	1.4	0.3	4.9	14.0	12.2	4.2	9.5	3.1	3.0	3.9	7.4	4.6	0.0	
bf4a run 1	30	132	10.3	3.2	0.57	9.4	24.1	3.5	16.9	4.6	1.5	5.4	0.95	5.2	1.03	2.9	0.40	2.5	0.50	
bf4a run 2	24	123	9.9	3.8	0.68	9.3	24.0	3.5	16.3	4.8	1.6	5.5	0.82	5.1	0.99	2.7	0.40	2.4	0.45	
% difference	23.7	7.2	4.2	14.9	17.6	0.2	0.4	0.9	3.9	5.3	4.6	1.3	14.7	1.4	4.0	5.7	0.0	4.9	10.5	
bf5b run 1	30	136	12.6	3.6	0.75	11.8	29.1	4.1	18.7	4.9	1.6	5.7	1.01	5.5	1.11	3.2	0.45	2.8	0.57	
bf5b run 2	27	126	11.6	3.8	0.80	11.7	29.0	4.1	18.7	5.6	1.7	5.9	0.90	5.6	1.09	3.2	0.45	2.8	0.54	
% difference	9.7	8.1	8.4	4.9	6.5	0.8	0.6	0.7	0.3	13.5	7.2	2.8	11.5	1.6	1.8	1.3	0.0	0.7	5.4	
bf6 run 1	49	92	3.4	1.0	0.09	8.1	18.7	2.5	11.4	3.1	1.1	4.0	0.74	4.4	0.92	2.7	0.40	2.6	0.53	
bf6 run 2	18	83	3.2	2.9	0.29	7.9	17.2	2.5	11.5	3.5	1.2	4.4	0.70	4.5	0.96	2.8	0.40	2.7	0.55	
% difference	90.6	10.3	6.3	94.4	105.3	2.7	8.7	0.4	0.8	11.3	6.8	7.6	5.6	2.9	4.3	4.8	0.0	2.3	3.7	
bf9 run 1	44	289	9.9	9.1	1.23	20.1	44.3	5.5	21.5	5.0	1.2	6.5	1.30	7.8	1.68	4.8	0.87	4.1	0.74	
bf9 run 2	36	248	5.6	7.5	0.42	13.2	38.2	4.4	15.1	4.1	1.0	5.1	0.95	6.5	1.35	3.8	0.53	3.1	0.56	
% difference	20	15	55	19	96	41	15	23	35	19	21	23	31	18	22	23	23	23	26	28
bf14 run 1	25	91	5.3	2.8	0.37	5.6	14.0	2.1	10.2	3.1	1.2	4.2	0.80	4.6	0.98	2.9	0.42	2.8	0.55	
bf14 run 2	23	83	5.2	3.0	0.40	5.3	13.4	2.0	9.8	3.3	1.2	4.3	0.68	4.5	0.97	2.9	0.42	2.7	0.53	
% difference	9.5	8.8	1.5	6.2	7.8	6.4	4.4	5.9	4.6	6.0	4.2	2.8	16.2	2.2	1.0	0.4	0.0	2.6	3.7	
bf17 run 1	34	120	10.2	2.3	0.44	11.0	26.7	3.8	17.4	4.6	1.6	5.2	0.94	5.1	1.00	2.8	0.40	2.5	0.49	
bf17 run 2	21	121	11.8	4.2	0.92	10.2	24.7	3.5	16.3	4.7	1.6	5.1	0.81	4.9	0.96	2.8	0.39	2.5	0.51	
% difference	47.6	0.8	14.8	59.8	70.6	7.6	7.4	7.7	6.3	2.2	0.6	1.6	14.9	4.4	4.1	1.4	2.5	2.0	4.0	
11ka10f run 1	22	48	4.3	1.5	0.24	3.4	9.4	1.5	7.5	2.5	1.0	3.3	0.66	3.7	0.80	2.3	0.33	2.1	0.43	
11ka10 run 2	19	49	4.5	1.7	0.26	3.4	9.4	1.5	7.8	2.7	1.0	3.4	0.57	3.6	0.74	2.2	0.32	2.1	0.41	
% difference	10.9	1.9	3.8	11.3	8.0	1.5	0.4	4.7	4.0	7.6	6.1	3.3	14.6	2.7	7.8	2.7	3.1	0.9	4.8	
Procedural blank, run 2	0.09	3.77	1.48	0.05	0.02	0.01	0.03	0.01	0.07	0.02	0.00	0.06	0.00	0.01	0.00	0.01	0.00	0.01	0.00	
Procedural blank, run 1	0.08	0.22	0.17	0.66	0.01	0.02	0.02	n.d.	0.01	0.02	n.d.	0.08	n.d.	0.01	n.d.	n.d.	n.d.	0.01	n.d.	
% difference	12	178	159	172	67	67	40	0	150	0	29	0	0	0	0	0	0	0	0	
MRG-1, run 1, analysis 1	12	101	21.9	4.0	0.88	8.8	25.1	3.6	17.8	4.3	1.4	4.3	0.63	2.9	0.48	1.2	0.15	0.82	0.14	
MRG-1, run 2	12	100	22.9	4.2	0.96	9.3	26.1	3.7	18.2	5.0	1.6	4.5	0.56	3.0	0.50	1.2	0.14	0.85	0.15	
% difference	4.2	0.4	4.5	4.1	8.7	5.5	3.8	1.9	2.1	14.9	12.2	3.4	11.8	2.4	4.1	1.7	6.9	3.6	6.9	
MRG-1, run 1, analysis 2	12	103	18.9	3.9	0.82	8.9	25.3	3.7	17.8	4.3	1.4	4.6	0.65	3.0	0.50	1.2	0.14	0.79	0.14	
MRG-1, run 2	12	100	22.9	4.2	0.96	9.3	26.1	3.7	18.2	5.0	1.6	4.5	0.56	3.0	0.50	1.2	0.14	0.85	0.15	
% difference	7	2	19	7	16	4	3	0	2	16	10	2	15	1	0	2	0	7	7	

for almost every element – from 15% for Ce to 98% for Ta. Heterogeneity within the sample is the likely cause of deviation. Thin section analysis confirms this heterogeneity.

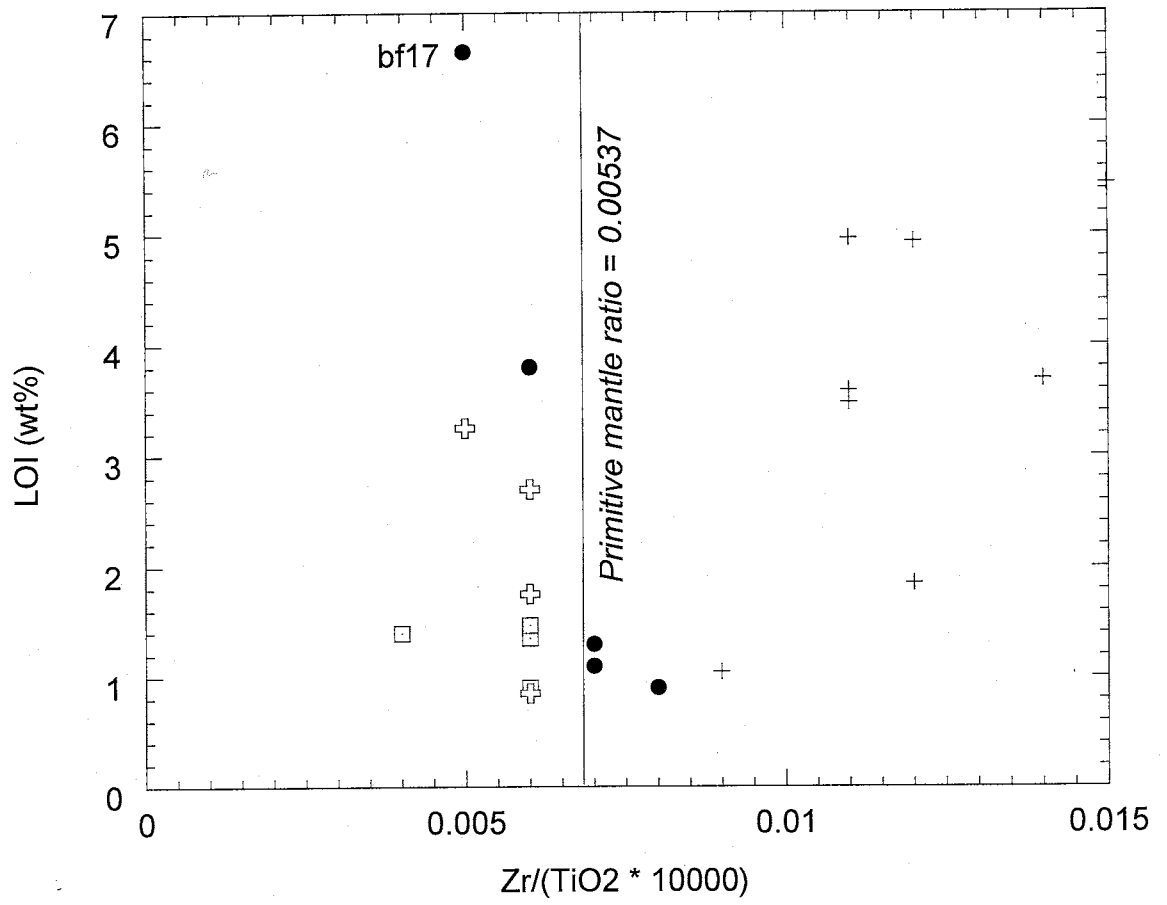
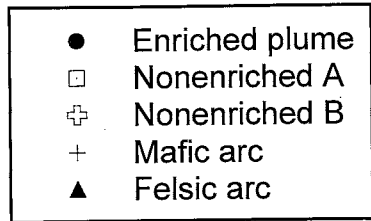
Yttrium, Hf, Ta, Sm and Tb show minor variation between the two runs. Low concentrations may be one cause of such imprecision. Tb and Ta have concentrations well below 1 ppm, for example. A mineral phase that did not dissolve completely during sample digestion may also be responsible for these variations. Jenner et al. (1990) described a third possible source of low precision among some elements, especially Ta and Nb: memory effects in the equipment and/or solution instability. Variation in REE, Hf and Ta values may also result from interference by Ba and REE oxides. Jenner et al. (1990) state that oxides produce the most significant interference on these elements. One of the most significant is that of $^{143}\text{Nd}^{16}\text{O}^+$ on $^{159}\text{Tb}^+$. Nevertheless, the authors add that according to their standard analysis the corrections followed in their protocol should be sufficient to correct such interference. If oxides cause these differences, this may indicate that the oxide correction used is not sufficient.

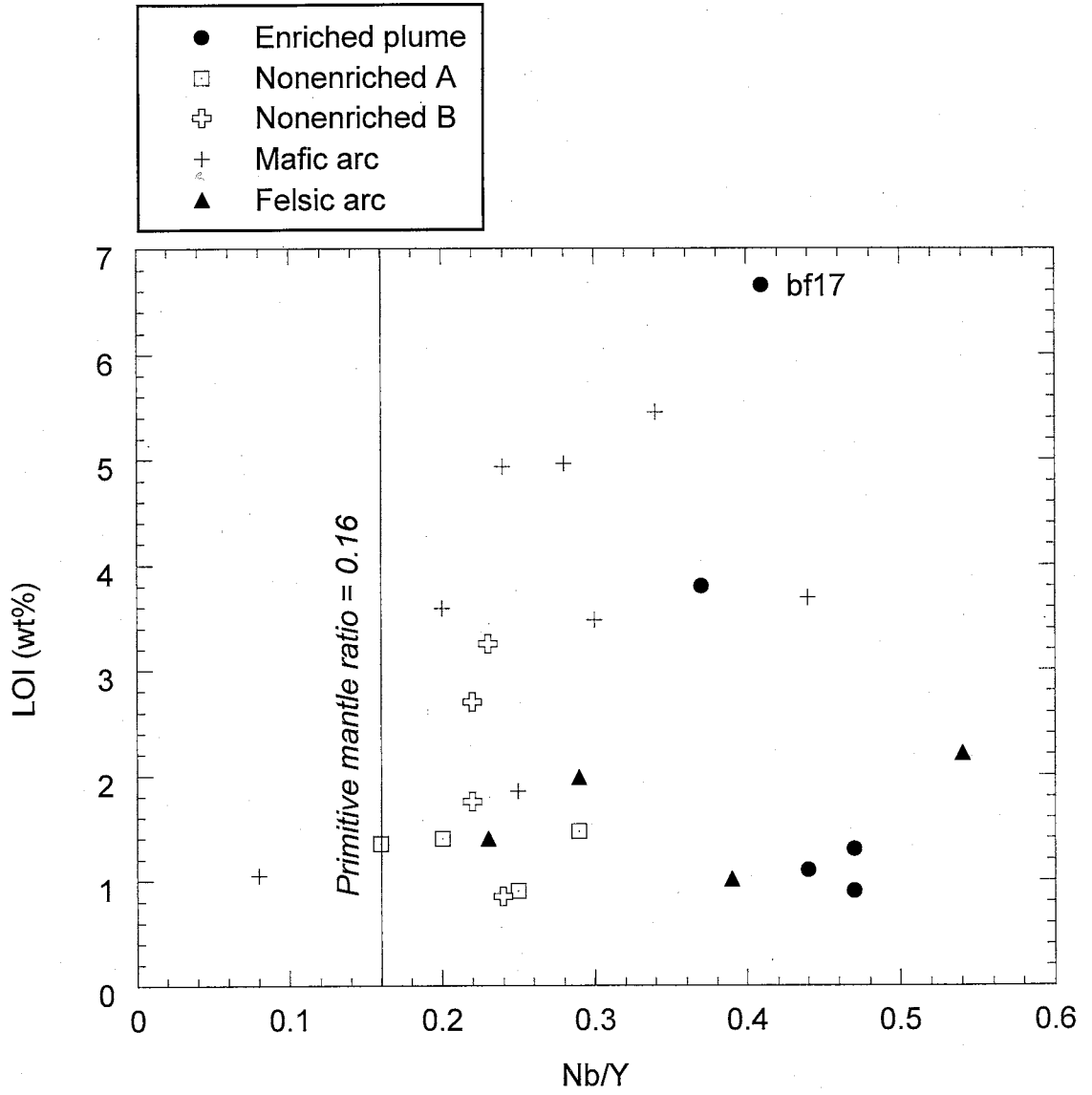
APPENDIX C

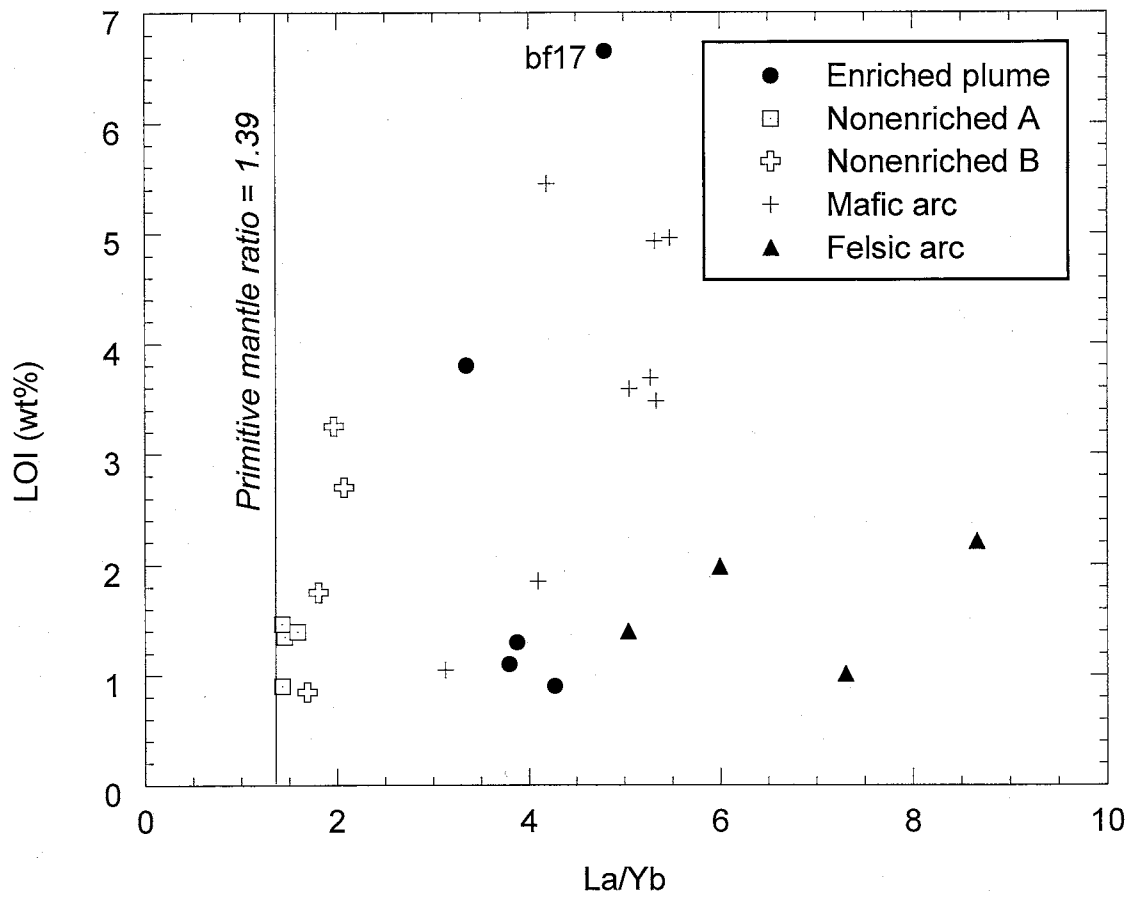
Loss on ignition diagrams for incompatible elements and element ratios

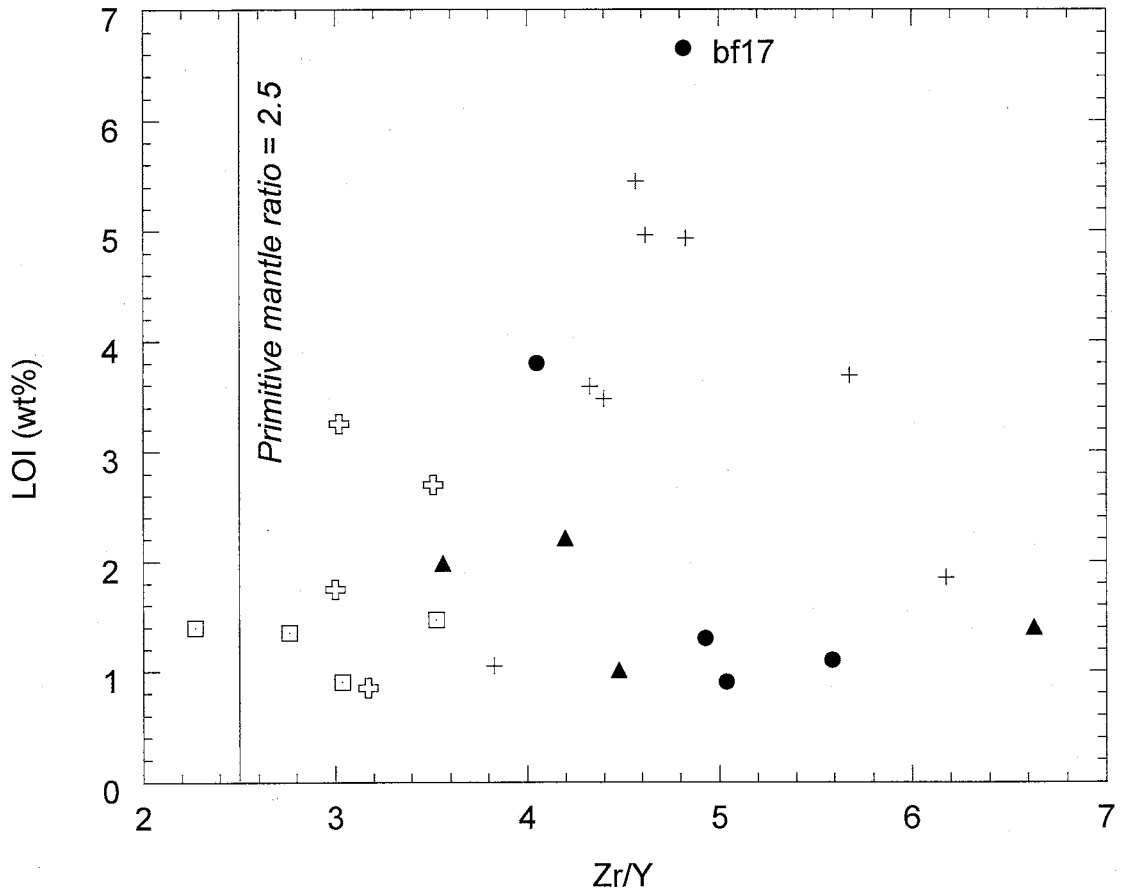
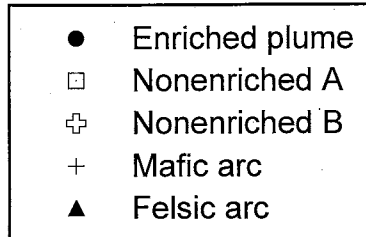
LOI graphs after Polat et al. (1999) showing that the ratios of trace elements do not correlate with LOI for the Iron King Volcanics. Graphs included in this appendix:

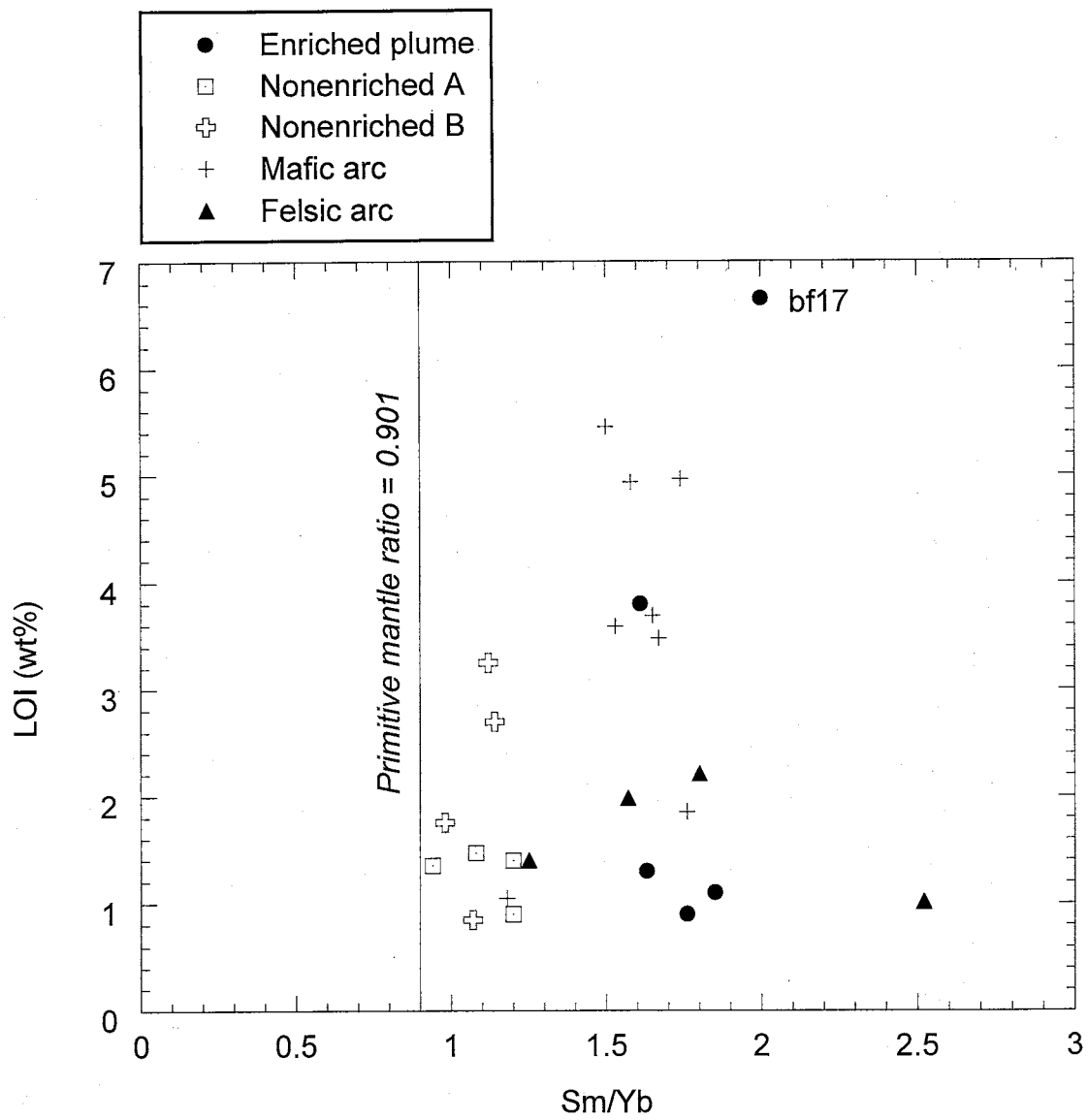
LOI versus Zr/TiO₂
LOI versus Nb/Y
LOI versus La/Yb
LOI versus Zr/Y
LOI versus Sm/Yb
LOI versus Nb/Zr
LOI versus Th
LOI versus Ta
LOI versus Zr/Hf
LOI versus La/Sm

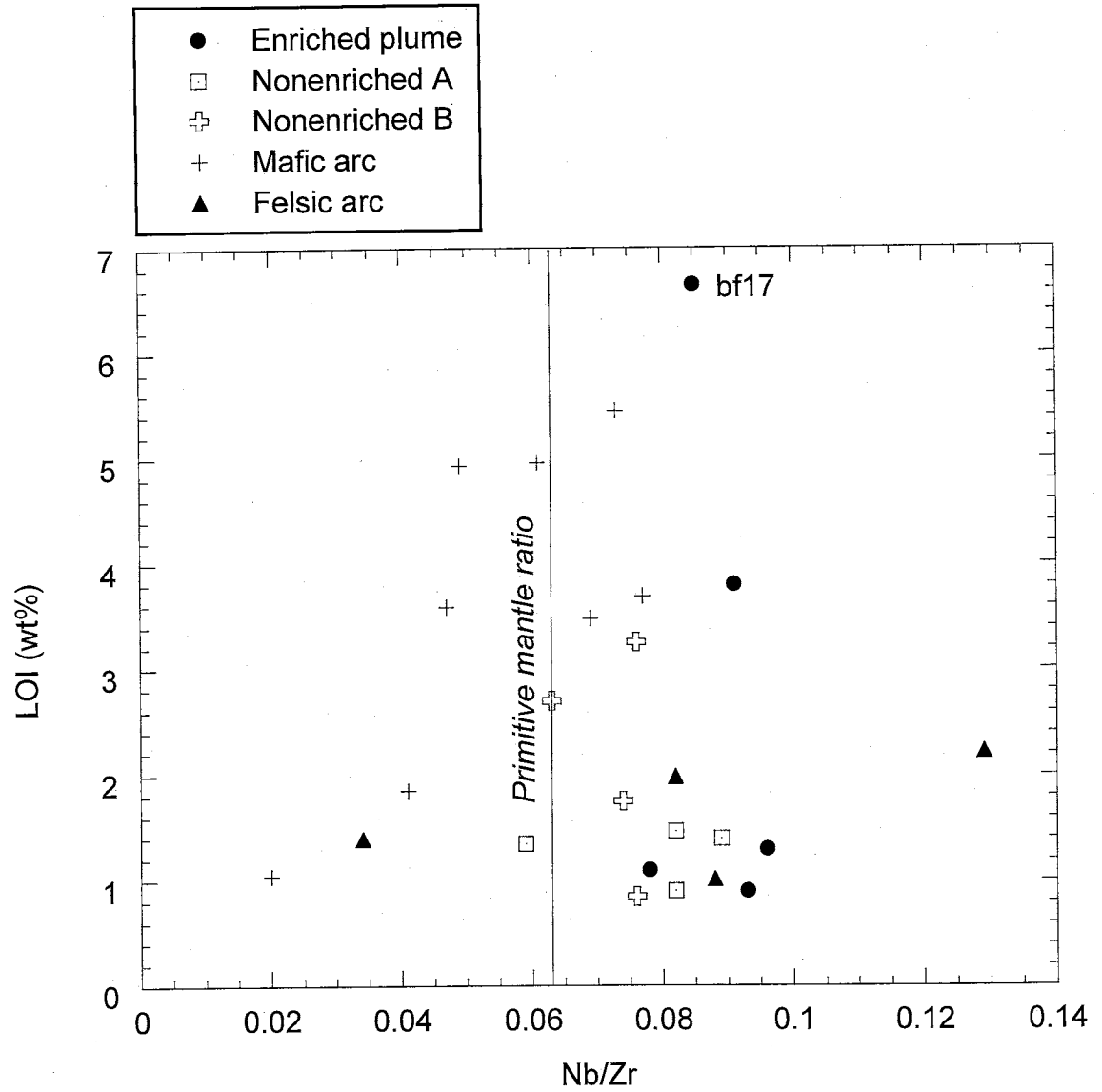


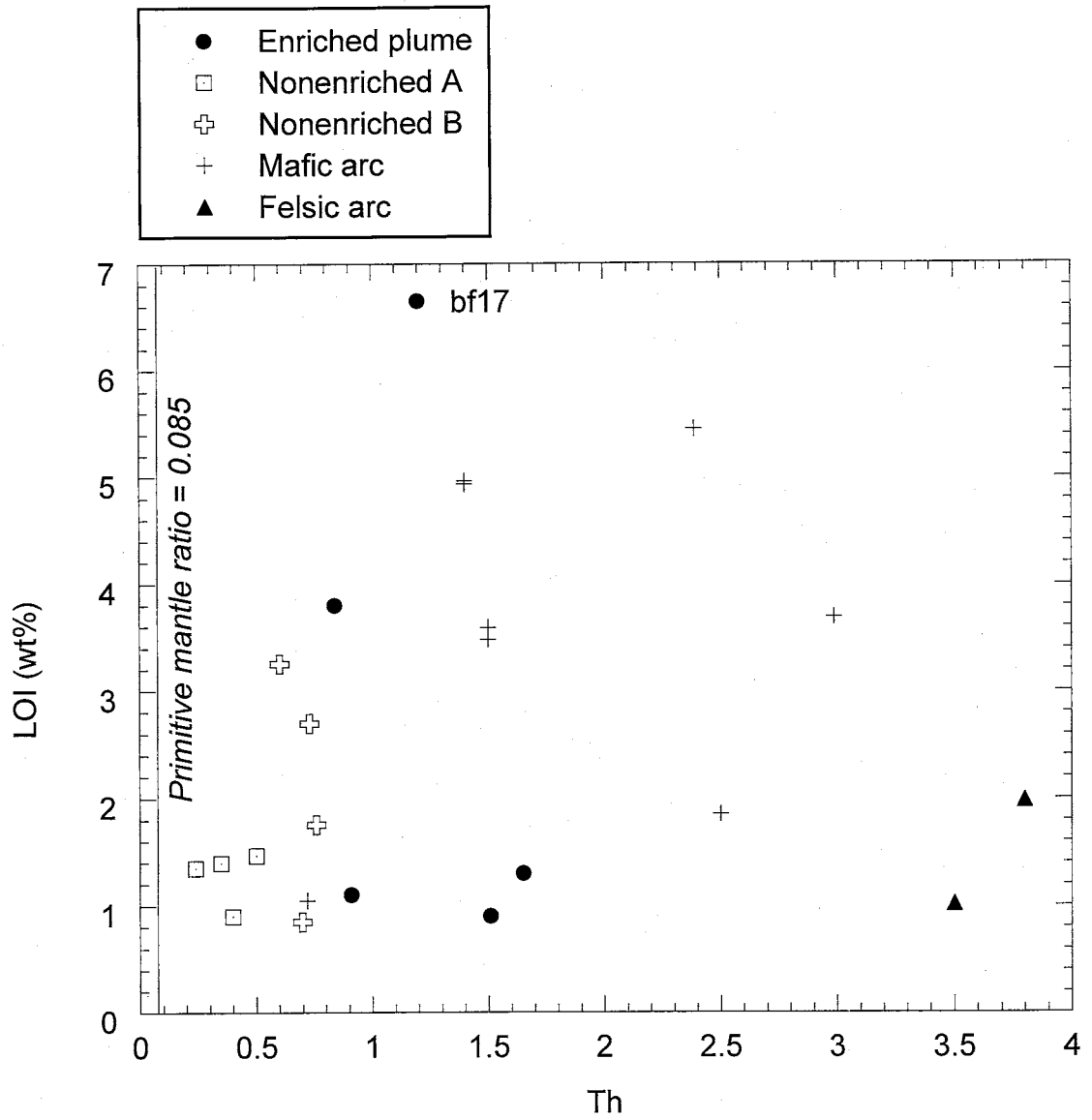


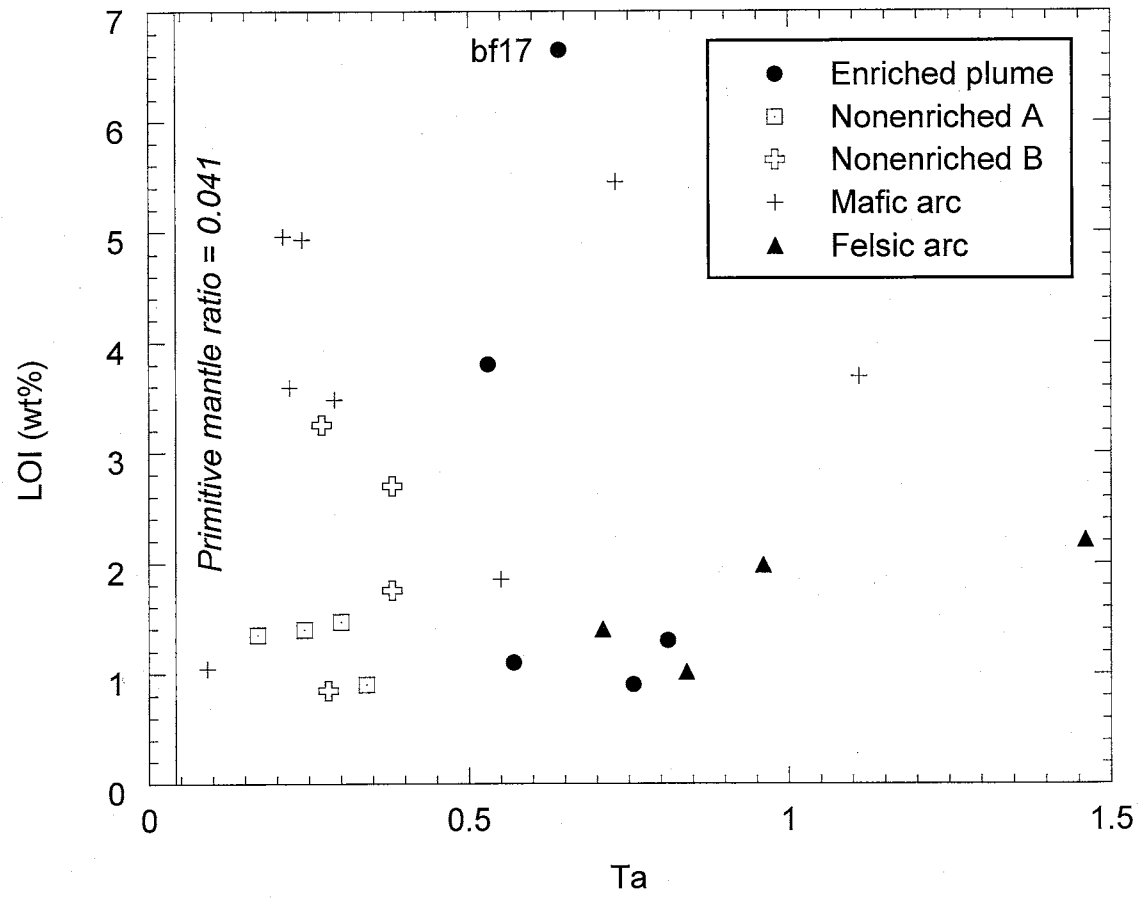


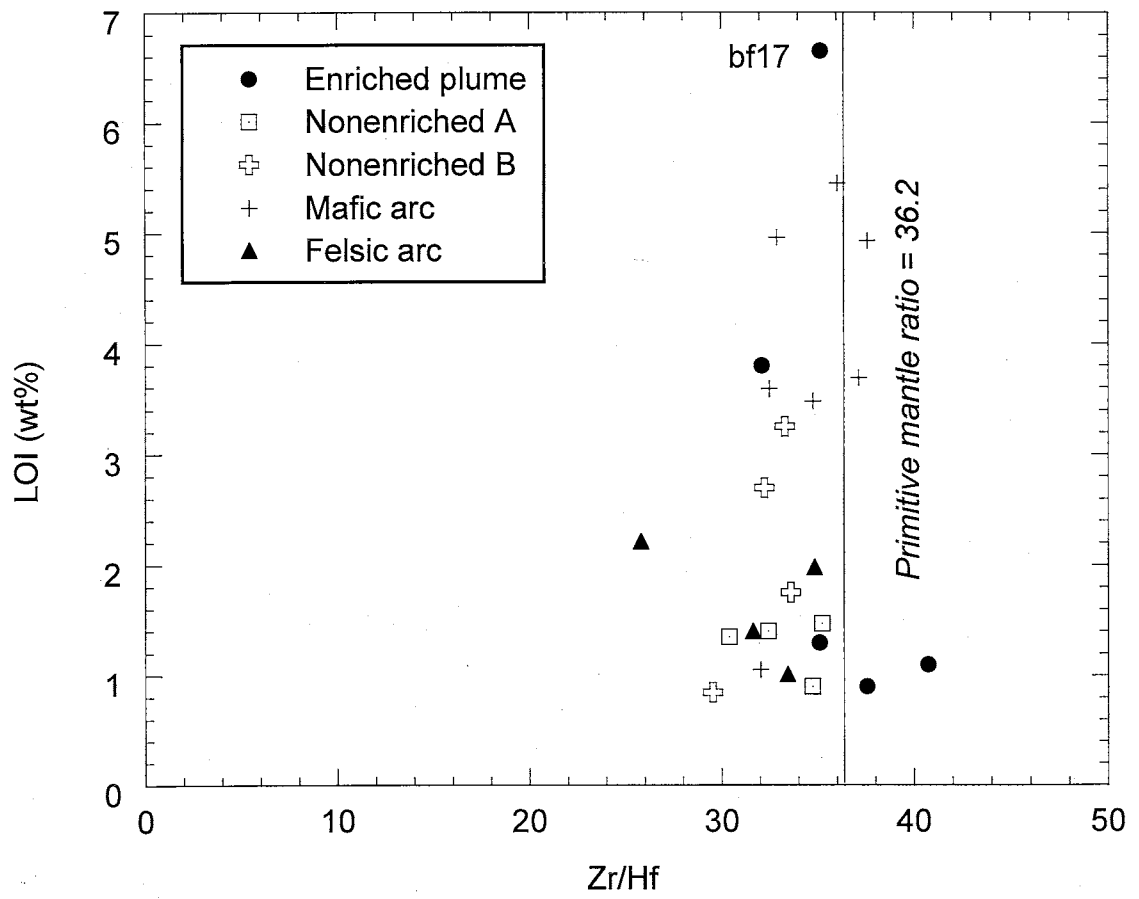


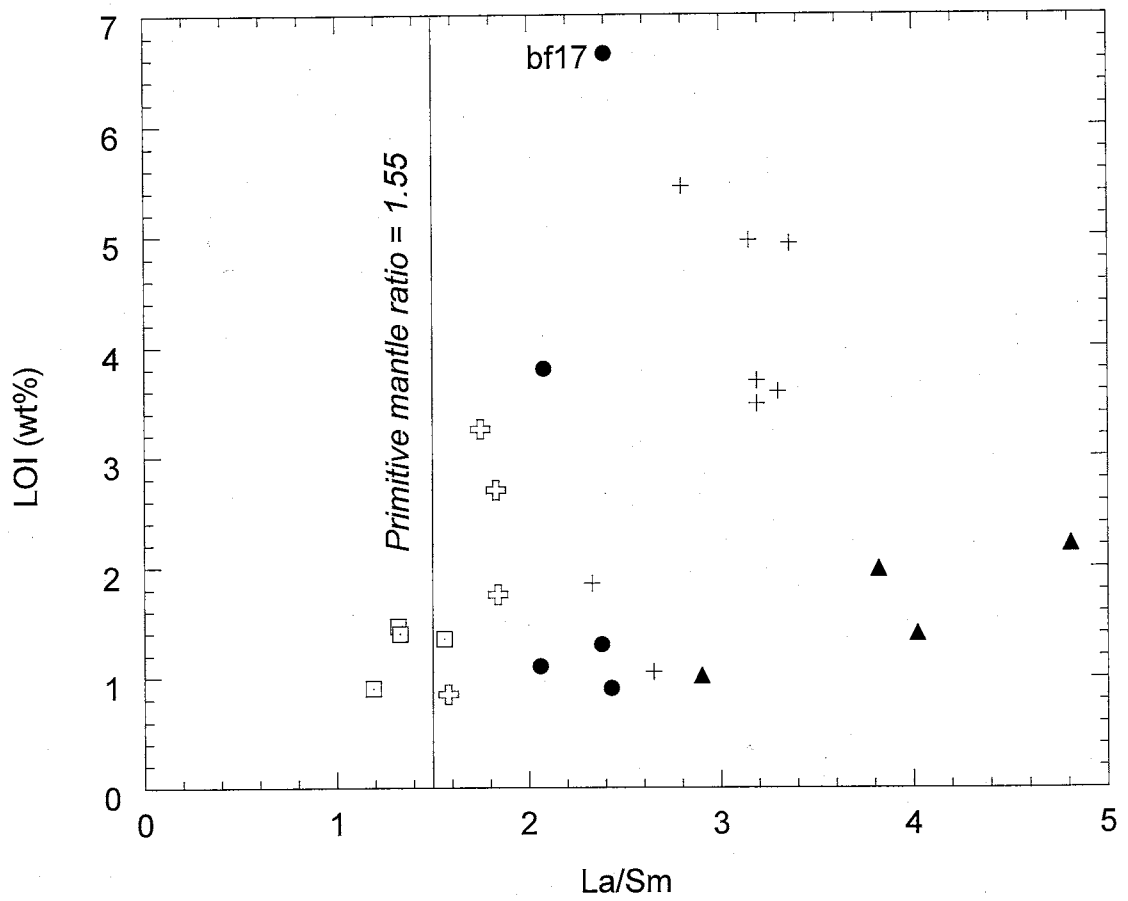
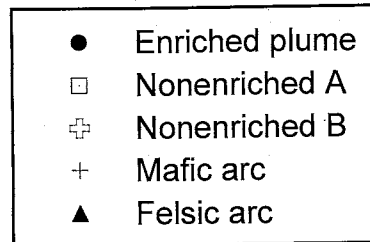












REFERENCES

- Abbott, D., and Mooney, W., 1995, The structural and geochemical evolution of the continental crust: Support for the oceanic plateau model of continental growth, Reviews of geophysics supplement to volume 33, 1995: U.S. National Report to International Union of Geodesy and Geophysics, 1991-1994: Washington, D.C., American Geophysical Union, p. 231-242.
- Anderson, C.A., and Creasey, S.C., 1958, Geology and ore deposits of the Jerome area, Yavapai County, Arizona, p. 185.
- Anderson, C.A., Blacet, P.M., Silver, L.T., and Stern, T.W., 1971, Revision of Precambrian stratigraphy in the Prescott-Jerome area, Yavapai County, Arizona, p. 16.
- Anderson, C.A., 1972, Precambrian rocks in the Cordes area, Yavapai County, Arizona: Washington, U.S. Government Printing Office, p. 36.
- Anderson, C.A., and Blacet, P.M., 1972a, Precambrian geology of the Northern Bradshaw Mountains, Yavapai County, Arizona: Washington, U.S. Government Printing Office, p. 82.
- , 1972b, Geologic map of the Mayer Quadrangle, Yavapai County, Arizona, U.S. Geological Survey.
- , 1972c, Geologic map of the Mount Union Quadrangle, Yavapai County, Arizona, U.S. Geological Survey.
- Anderson, C.A., and Silver, L.T., 1976, Yavapai Series – A greenstone belt, *in* Wilt, J. C., Jenney, J. P., editor, Tectonic Digest: Arizona Geological Society Digest 10, p. 13-26.
- Barker, F., 1994, Some accreted volcanic rocks of Alaska and their elemental abundances, *in* Plafker, G., and Berg, H.C., editor, The Geology of Alaska: The Geology of North America, v. G-1: Boulder, Colorado, Geological Society of America.
- Batiza, R., and White, J.D., 2000, Submarine lavas and hyaloclastite, *in* Sigurdsson, H., editor, Encyclopedia of Volcanoes: San Diego, Academic Press, p. 361-381.

Bowring, S.A., Chamberlain, K.R., Dann, J.C., and Karlstrom, K.E., 1991, U-Pb geochronologic constraints on the early Proterozoic evolution of Arizona: Geological Society of America Abstracts with Programs, v. 23, p. 7.

Campbell, I.H., 2001, The identification of ancient mantle plumes, *in* Ernst, R. E., and Buchan, K.L., editor, Mantle Plumes: Their Identification Through Time: Geological Society of America Special Paper 352, p. 5-21.

Cas, R.A.F., and Wright, J.V., 1987, Volcanic Successions: Modern and Ancient: London, Allen & Unwin, 528 p.

Chaffey, D.J., Cliff, R.A., and Wilson, B.M., 1989, Characterization of the St. Helena magma source, *in* Saunders, A. D., and Norry, M.J., editor, Magmatism in the Ocean Basins: Geological Society Special Publication No. 42, p. 257-276.

Clague, D.A., and Frey, F.A., 1982, Petrology and trace element geochemistry of the Honolulu Volcanics, Oahu: Implication for the oceanic mantle below Hawaii: Journal of Petrology, v. 23, p. 447-504.

Cloos, M., 1993, Lithospheric buoyancy and collisional orogenesis: Subduction of oceanic plateaus, continental margins, island arcs, spreading ridges, and seamounts: Geological Society of America Bulletin, v. 105, p. 715-737.

Condie, K.C., 1981, Precambrian rocks of southwestern United States and adjacent areas of Mexico, New Mexico Bureau of Mines.

-, 1984, Early Proterozoic supracrustal associations in the Southwest; an update: Geological Society of America Abstracts with Programs, Rocky Mountain Section, 37th annual meeting, v. 16, p. 218.

-, 1986, Geochemistry and tectonic setting of early Proterozoic supracrustal rocks in the southwestern United States: Journal of Geology, v. 94, p. 845-864.

-, 1993, Chemical composition and evolution of the upper continental crust: Contrasting results from surface samples and shales: Chemical Geology, v. 104, p. 1-37.

Condie, K.C., 1994, Greenstones through time, *in* Condie, K. C., editor, Archean Crustal Evolution: Amsterdam, Elsevier, p. 528.

-, 1997a, Contrasting sources for upper and lower continental crust: The greenstone connection: The Journal of Geology, v. 105, p. 729-736.

-, 1997b, Plate Tectonics and Crustal Evolution: Oxford, Butterworth-Heinemann, 282 p.

-, 2001, Mantle plumes and their record in earth history, Cambridge University Press.

Conway, C.M., and Silver, L.T., 1989, Early Proterozoic rocks (1710-1615 Ma) in central to southeastern Arizona, *in* Jenney, J. P., and Reynolds, S.J., editor, Geologic evolution of Arizona: Arizona Geological Society Digest 17: Tucson, Arizona Geological Society, p. 165-186.

Corcoran, P.L., 2000, Recognizing distinct portions of seamounts using volcanic facies analysis: examples from the Archean Slave Province, NWT, Canada: *Precambrian Research*, v. 101, p. 237-261.

Cox, K.G., Bell, J.D., and Pankhurst, R.J., 1979, The interpretation of igneous rocks: London, Allen and Unwin.

Darrach, M.E., Karlstrom, K.E., Argenbright, D.N., and Williams, M.L., 1991, Progressive deformation in the early Proterozoic Shylock shear zone, central Arizona, *in* Karlstrom, K. E., editor, Proterozoic Geology and Ore Deposits of Arizona, Arizona Geological Society Digest 19, p. 97-116.

David, K., Schiano, P., and Allegre, C.J., 2000, Assessment of the Zr/Hf fractionation in oceanic basalts and continental materials during petrogenetic processes: *Earth and Planetary Science Letters*, v. 178, p. 285-301.

Davies, G. F., 1999, *Dynamic Earth: Plates, Plumes and Mantle Convection*: Cambridge, Cambridge University Press, 458 p.

Devey, C.W., Hemond, C., and Stoffers, P., 2000, Metasomatic reactions between carbonated plume melts and mantle harzburgite: The evidence from Friday and Domingo Seamounts (Juan Fernandez chain, SE Pacific): *Contributions to Mineralogy and Petrology*, v. 139, p. 68-84.

DeWitt, E., 1995, Base- and precious-metal concentrations of early Proterozoic massive sulfide deposits in Arizona – Crustal and thermochemical controls of ore deposition: *U.S. Geological Survey Bulletin 2138*: Washington, 36 p.

Dostal, J., and Church, B.N., 1994, Geology and geochemistry of the volcanic rocks of the Pioneer Formation, Bridge River area, southwestern British Columbia (Canada): *Geological Magazine*, v. 131, p. 243-253.

Dupuy, C., Barseczus, H.G., Dostal, J., Vidal, P., and Liotard, J.-M., 1989, Subducted and recycled lithosphere in the mantle source of ocean island basalts from southern Polynesia, central Pacific: *Chemical Geology*, v. 77, p. 1-18.

Ewart, A., Collerson, K.D., Regelous, M., Wendt, J.I., and Niu, Y., 1998, Geochemical evolution within the Tonga-Kermadec-Lau Arc-Back-arc systems: The role of varying mantle wedge composition in space and time: *Journal of Petrology*, v. 39, p. 331-368.

Fan, J., and Kerrich, R., 1997, Geochemical characteristics of aluminum depleted and undepleted komatiites and HREE-enriched low-Ti tholeiites, western Abitibi greenstone belt: a heterogeneous mantle plume-convergent margin environment: *Geochimica et Cosmochimica Acta*, v. 61, p. 4723-4744.

Fink, J.H., and Griffiths, R.W., 1992, A laboratory analog study of the surface morphology of lava flows extruded from point and line sources: *Journal of Volcanology and Geothermal Research*, v. 54, p. 19-32.

Fisher, R.V., 1984, Submarine volcanoclastic rocks, *in* Kokelaar, B. P., Howells, M.F., editor, *Marginal basin geology: Volcanic and associated sedimentary and tectonic processes in modern and ancient marginal basins*: Oxford, Blackwell Scientific Publications for the Geological Society, p. 5-27.

Fisher, R.V., and Schmincke, H.-U., 1984, *Pyroclastic Rocks*: Berlin, Springer-Verlag, p. 472.

Fitton, J.G., Saunders, A.D., Norry, M.J., Hardarson, B.S., and Taylor, R.N., 1997, Thermal and chemical structure of the Iceland plume: *Earth and Planetary Science Letters*, v. 153, p. 197-208.

Frey, F.A., Jones, W.B., Davies, H., and Weis, D., 1991, Geochemical and petrologic data for basalts from sites 756, 757, and 758: Implications for the origin and evolution of Ninetyeast Ridge, *in* Weissel, J., Peirce, J., Taylor, E., Alt, J., et al., editor, *Proceedings of the ocean drilling program, scientific results*.

Govindaraju, K., 1994, 1994 compilation of working values and sample description for 383 geostandards: *Geostandards Newsletter*, v. 18.

Green, J.C., 1992, Proterozoic rifts, *in* Condie, K. C., editor, *Proterozoic Crustal Evolution: Developments in Precambrian Geology 10*: Amsterdam, Elsevier, p. 97-149.

Gross, G.A., 1996a, Stratiform iron, *in* Eckstrand, O. R., Sinclair, W.D., and Thorpe, R.I., editor, *Geology of Canadian Mineral Deposit Types: Geology of Canada*, No. 8, Geological Survey of Canada, p. 41-54.

-, 1996b, Algoma-type iron-formation, *in* Eckstrand, O. R., Sinclair, W.D., and Thorpe, R.I., editor, *Geology of Canadian Mineral Deposit Types: Geology of Canada*, no. 8, Geological Survey of Canada, p. 66-73.

Haskin, L.A., Haskin, M.A., Frey, F.A., and Wildeman, T.R., 1968, Relative and absolute terrestrial abundances of the rare earths, *in* Ahrens, L. H., editor, *Origin and distribution of the elements*: New York, Pergamon, p. 889-912.

Henderson, J.B., Caldwell, W.G.E., Harrison, J.E., 1980, North American Commission on Stratigraphic Nomenclature; Report 8, Amendment of Code concerning terminology for igneous and high-grade metamorphic rocks: *Geological Society of America Bulletin* 91, v. 6, 374-376 p.

Herzberg, C., 1995, Generation of plume magmas through time: An experimental perspective: *Chemical Geology*, v. 126, p. 1-16.

Hoffman, P.F., 1988, United plates of America, the birth of a craton: Early Proterozoic assembly and growth of Laurentia, *in* Wetherill, G. W., editor, *Annual Review of Earth and Planetary Sciences*: Palo Alto, California, Annual Reviews Inc., p. 676.

-, 1989, Speculations on Laurentia's first gigayear (2.0 to 1.0 Ga): *Geology*, v. 17, p. 135-138.

Hofmann, A.W., 1988, Chemical differentiation of the Earth: the relationship between mantle, continental crust, and oceanic crust: *Earth and Planetary Science Letters*, v. 90, p. 297-314.

Jenner, G.A., Longerich, H.P., Jackson, S.E., and Fryer, B.J., 1990, ICP-MS -- A powerful tool for high-precision trace-element analysis in Earth sciences: Evidence from analysis of selected U.S.G.S. reference samples: *Chemical Geology*, v. 83, p. 133-148.

Karlstrom, K.E., Bowring, S.A., and Conway, C.M., 1987, Tectonic significance of an Early Proterozoic two-province boundary in central Arizona: *Geological Society of America Bulletin*, v. 99, p. 529-538.

Karlstrom, K.E., and Bowring, S.A., 1988, Early Proterozoic assembly of tectonostratigraphic terranes in southwestern North America: *Journal of Geology*, v. 96, p. 561-576.

Karlstrom, K.E., 1991, Styles and timing of early Proterozoic deformation in Arizona; Constraints on tectonic models, in Karlstrom, K. E., editor, *Proterozoic geology and ore deposits of Arizona: Arizona Geological Society Digest 19*, p. 1-10.

Karlstrom, K.E., and Bowring, S.A., 1993, Proterozoic orogenic history of Arizona, *in* Reed Jr., J. C., et al., editor, *Precambrian: Conterminous U.S.: The Geology of North America: Boulder, Colo., Geological Society of America*, p. 657.

Kepezhinskas, P., McDermott, F., Defant, M.J., Hochstaedter, A., Drummond, M.S., Hawkesworth, C., Koloskov, A., Maury, R.C., and Bellon, H., 1997, Trace element and Sr-Nd-Pb isotopic constraints on a three-component model of Kamchatka Arc petrogenesis: *Geochimica et Cosmochimica Acta*, v. 61, p. 577-600.

Kerr, A.C., Marriner, G.F., Tarney, J., Nivia, A., Saunders, A.D., Thirlwall, M.F., Sinton, C.W., 1997, Cretaceous basaltic terranes in western Columbia: Elemental, chronological and Sr-Nd isotopic constraints on petrogenesis: *Journal of Petrology*, v. 38, p. 677-702.

Kerr, A.C., Tarney, J., Nivia, A., Marriner, G.F., Saunders, A.D., 1998, The internal structure of oceanic plateaus: inferences from obducted Cretaceous terranes in western Columbia and the Caribbean: *Tectonophysics*, v. 292, p. 173-188.

Kerr, A.C., White, R.V., and Saunders, A.D., 2000, LIP reading: Recognizing oceanic plateaux in the geological record: *Journal of Petrology*, v. 41, p. 1041-1056.

Knoper, M.W., Condie, K.C., 1988, Geochemistry and petrogenesis of early Proterozoic amphibolites, west-central Colorado, U.S.A.: *Chemical Geology*, v. 67, p. 209-225.

Lassiter, J.C., and DePaolo, D.J., 1997, Plume/lithosphere interaction in the generation of continental and oceanic flood basalts: Chemical and isotopic constraints, *in* Mahoney, J. J., Coffin, M.F., editor, *Large Igneous Provinces: Continental, Oceanic, and*

Planetary Flood Volcanism: Washington, D.C., American Geophysical Union, p. 335-355.

Lindberg, P.A., 1989, Precambrian ore deposits of Arizona, *in* Jenney, J. P., and Reynolds, S.J., editor, Geologic evolution of Arizona: Arizona Geological Society Digest 17, p. 187-210.

Lindgren, W., 1926, Ore deposits of the Jerome and Bradshaw Mountains Quadrangles, Arizona: U.S. Geological Survey Bulletin 782: Washington, 192 p.

MacLean, W.H., and Barrett, T.J., 1993, Lithogeochemical techniques using immobile elements: *Journal of Geochemical Exploration*, v. 48, p. 109-133.

Mahoney, J.J., Storey, M., Duncan, R.A., Spencer, K.J., and Pringle, M., 1993, Geochemistry and age of the Ontong Java Plateau, *in* Pringle, M. S., editor, *The Mesozoic Pacific: Geology, Tectonics, and Volcanism*: Washington, D.C., American Geophysical Union, p. 233-261.

Mahoney, J.J., Jones, W.B., Frey, F.A., Salters, V.J.M., Pyle, D.G., and Davies, H.L., 1995, Geochemical characteristics of lavas from Broken Ridge, the Naturaliste Plateau and southernmost Kerguelen Plateau: Cretaceous plateau volcanism in the southeast Indian Ocean: *Chemical Geology*, v. 120, p. 315-345.

McCulloch, M.T., and Gamble, J.A., 1991, Geochemical and geodynamical constraints on subduction zone magmatism: *Earth and Planetary Science Letters*, v. 102, p. 358-374.

Middlemost, E.A.K., 1975, The Basalt Clan: *Earth-Science Reviews*, v. 11, p. 337-364.

Mortimer, N., and Parkinson, D., 1996, Hikurangi Plateau: A Cretaceous large igneous province in the southwest Pacific Ocean: *Journal of Geophysical Research*, v. 101, p. 687-696.

Neal, C.R., Mahoney, J.J., Kroenke, L.W., Duncan, R.A., and Petterson, M.G., 1997, The Ontong Java Plateau, *in* Mahoney, J. J., Coffin, M.F., editor, *Large Igneous Provinces: Continental, Oceanic, and Planetary Flood Volcanism*: Washington, D.C., American Geophysical Union, p. 438.

Pavel, K., McDermott, F., Defant, M.J., Hochstaedter, A., Drummond, M.S., Hawkesworth, C., Koloskov, A., Maury, R.C., and Bellon, H., 1997, Trace element and

Sr-Nd-Pb isotopic constraints on a three-component model of Kamchatka Arc petrogenesis: *Geochimica et Cosmochimica Acta*, v. 61, p. 577-600.

Pearce, J.A., 1983, Role of the sub-continental lithosphere in magma genesis at active continental margins, *in* Hawkesworth, C. J., and Norry, M.J., editor, *Continental basalts and mantle xenoliths: Cheshire, England*, Shiva Publishing Ltd., p. 272.

Pearce, J.A., Baker, P.E., Harvey, P.K., and Luff, I.W., 1995, Geochemical evidence for subduction fluxes, mantle melting and fractional crystallization beneath the South Sandwich Island Arc: *Journal of Petrology*, v. 36, p. 1073-1109.

Petterson, M.G., Babbs, T., Neal, C.R., Mahoney, J.J., Saunders, A.D., Duncan, R.A., Tolia, D., Magu, R., Qopoto, C., Mahoa, H., and Natogga, D., 1999, Geological-tectonic framework of Solomon Islands, SW Pacific: crustal accretion and growth within an intra-oceanic setting: *Tectonophysics*, v. 301, p. 35-60.

Polat, A., Kerrich, R., and Wyman, D.A., 1998, The late Archean Schreiber-Hemlo and White River-Dayohessarah greenstone belts, Superior Province: Collages of oceanic plateaus, oceanic arcs, and subduction-accretion complexes: *Tectonophysics*, v. 289, p. 295-326.

-, 1999, Geochemical diversity in oceanic komatiites and basalts from the late Archean Wawa greenstone belts, Superior Province, Canada: Trace element and Nd isotope evidence for a heterogeneous mantle: *Precambrian Research*, v. 94, p. 139-173.

Robinson, P.T., and Malpas, J., 1999, *Oceanic Lithosphere 3. The Origin and Evolution of Oceanic Lithosphere: The Geochemistry and Origin of Oceanic Lavas*: *Geoscience Canada*, v. 26, p. 71-80.

Roden, M.F., Frey, F.A., and Clague, D.A., 1984, Geochemistry of tholeiitic and alkalic lavas from the Koolau Range, Oahu, Hawaii: Implications for Hawaiian volcanism: *Earth and Planetary Science Letters*, v. 69, p. 141-158.

Rollinson, H., 1993, *Using geochemical data: evaluation, presentation, interpretation*: Harlow, Prentice Hall, 352 p.

Saunders, A.D., and Tarney, J., 1984, Geochemical characteristics of basaltic volcanism within back-arc basins, *in* Kokelaar, B.P., Howells, M.F., editor, *Marginal basin geology: Volcanic and associated sedimentary and tectonic processes in modern*

and ancient marginal basins: Oxford, Blackwell Scientific Publications for the Geological Society, p. 59-76.

Schubert, G., and Sandwell, D., 1989, Crustal volumes of the continents and of oceanic and continental submarine plateaus: *Earth and Planetary Science Letters*, v. 92, p. 234-246.

Sharma, M., 1997, Siberian traps, *in* Mahoney, J.J., Coffin, M.F., editor, *Large Igneous Provinces: Continental, Oceanic, and Planetary Flood Volcanism*: Washington, D.C., American Geophysical Union, p. 273-295.

Shinjo, R., Woodhead, J.D., Hergt, J.M., 2000, Geochemical variation within the northern Ryukyu Arc: Magma source compositions and geodynamic implications: *Contributions to Mineralogy and Petrology*, v. 140, p. 263-282.

Sinton, C.W., Duncan, R.A., and Denyer, P., 1997, Nicoya Peninsula, Costa Rica: A single suite of Caribbean oceanic plateau magmas: *Journal of Geophysical Research*, v. 102, p. 15,507-15,520.

Smith, T.E., 1992, Volcanic rocks of early Proterozoic greenstone belts, *in* Condie, K.C., editor, *Proterozoic Crustal Evolution: Developments in Precambrian Geology 10*: Amsterdam, Elsevier, p. 7-54.

Staudigel, H., and Schmincke, H-U., 1984, The Pliocene Seamount Series of La Palma/Canary Islands: *Journal of Geophysical Research*, v. 89, p. 11,195-11,215.

Steiger, R.H., and Jaeger, E., 1977, Subcommission on geochronology; convention on the use of decay constants in geo- and cosmochronology: *Earth and Planetary Science Letters*, v. 36, p. 359-362.

Sun, S.-s., Nesbitt, R.W., and Sharaskin, A., 1979, Geochemical characteristics of mid-ocean ridge basalts: *Earth and Planetary Science Letters*, v. 44, p. 119-138.

Sun, S.-s., and McDonough, W.F., 1989, Chemical and isotopic systematics of oceanic basalts; implications for mantle composition and processes, *in* Saunders, A.D., Norry, M.J., editor, *Magmatism in the ocean basins: Geological Society Special Publications*: Oxford, for The Geological Society by Blackwell Scientific Publications, p. 313-345.

Tarney, J., Wood, D.A., Varet, J., Saunders, A.D., and Cann, J.R., 1979, Nature of mantle heterogeneity in the North Atlantic: Evidence from Leg 49 basalts, *Deep drilling*

results in the Atlantic Ocean; ocean crust: Maurice Ewing Series 2, American Geophysical Union, p. 285-301.

Thurston, P.C., 1994, Archean volcanic patterns, *in* Condie, K.C., editor, *Archean Crustal Evolution*: Amsterdam, Elsevier, p. 528.

Togashi, S., Imai, N., Okuyama-Kusunose, Y., Tanaka, T., Okai, T., Koma, T., and Murata, Y., 2000, Young upper crustal chemical composition of the orogenic Japan Arc: *Geochemistry Geophysics Geosystems*, v. 1.

Tomlinson, K., and Condie, K., 2001, Archean mantle plumes: Evidence from greenstone belt geochemistry, *in* Ernst, R.E., and Buchan, K.L., editor, *Mantle Plumes: Their Identification Through Time*, Geological Society of America Special Paper 352, p. 341-358.

Van Schmus, W.R., and Bickford, M.E., 1993, Transcontinental Proterozoic provinces, *in* Reed Jr., J.C., et al., editor, *Precambrian: Conterminous U.S.: The Geology of North America*: Boulder, Colo., Geological Society of America, p. 657.

Vance, R.K., 1989, Geochemistry and tectonic setting of the early Proterozoic Yavapai Supergroup, Central Arizona, Geoscience Department: Socorro, New Mexico, New Mexico Institute of Mining and Technology, p. 461.

White, W.M., and Duncan, R.A., 1996, Geochemistry and geochronology of the Society Islands: New evidence for deep mantle recycling, *Earth Processes – Reading the Isotopic Code: Geophysical Monograph 95*, American Geophysical Union.

Williams, M.L., 1991, Overview of Proterozoic metamorphism in Arizona, *in* Karlstrom, K. E., editor, *Proterozoic and geology and ore deposits of Arizona*: Arizona Geological Society Digest 19, p. 11-26.

Wilson, M., 1989, *Igneous Petrogenesis: A Global Tectonic Approach*: London, Chapman & Hall, 466 p.

Winchester, J.A., and Floyd, P.A., 1977, Geochemical discrimination of different magma series and their differentiation products using immobile elements: *Chemical Geology*, v. 20, p. 325-343.

Winter, J.D., 2001, *An Introduction to Igneous and Metamorphic Petrology*: Upper Saddle River, New Jersey, Prentice Hall, 697 p.

Woodhead, J.D., Eggins, S.M., and Johnson, R.W., 1998, Magma genesis in the New Britain Island Arc: Further insights into melting and mass transfer processes: *Journal of Petrology*, v. 39, p. 1641-1668.

Xie, Q., and Kerrich, R., 1995, Application of isotope dilution for precise measurement of Zr and Hf in low-abundance samples and international reference materials by inductively coupled plasma mass spectrometry: implications for Zr (Hf)/REE fractionations in komatiites: *Chemical Geology*, v. 123, p. 17-27.

This thesis is accepted on behalf of the
Faculty of the Institute by the following committee:

Kenn D. Lordin

Advisor

Neha W. Gupta

[Signature]

January 15, 2002

Date

I release this document to the New Mexico Institute of Mining and Technology.

Bonnie [Signature]

Student's Signature

Jan. 25, 2002

Date